Resonant excitation of a nanowire quantum dot and optical frequency shifting via electro-optic modulation

by

Turner Garrow

A thesis
presented to the University of Waterloo
in fulfillment of the
thesis requirement for the degree of
Master of Applied Science
in
Electrical and Computer Engineering (Quantum Information)

Waterloo, Ontario, Canada, 2021

Author's Declaration

This thesis consists of material all of which I authored or co-authored: see Statement of Contributions included in the thesis. This is a true copy of the thesis, including any required final revisions, as accepted by my examiners.

I understand that my thesis may be made electronically available to the public.

Statement of Contributions

The results presented in the thesis were only possible through collaboration with several people. The tomography apparatus in Chapter 3 was designed by Arash Ahmadi and built by him and I. The pulse shaper discussed in 3.2.1 was initially built by Jeff Salvail, and was redesigned based on advice from Arash Ahmadi. The tomography measurements were taken with help from Mohd Zeeshan. The frequency shifting results in Chapter 5 follow directly from work by Simon Daley and Michael Kobierski. Matteo Pennacchietti assisted with data acquisition for the results in Chapter 5.

Abstract

The ability to create pairs of entangled photons is a requirement for many near-future quantum technologies. Despite this, the current state-of-the-art entangled photon sources are fundamentally limited in their performance by their probabilistic nature. Recently, semiconductor quantum dots have gained a great deal of interest as candidates for next-generation entangled photon sources. Quantum dots can produce photon pairs deterministically, and therefore do not suffer from the same limitation. In addition, certain emission properties such as the emission direction, lifetime and spectral linewidth can be greatly improved by embedding the quantum dot within a nanostructure.

The results in this thesis are from two separate, but related, techniques relating to the performance of an InAsP quantum dot embedded in an InP photonic nanowire. The first technique is resonant two-photon excitation of the quantum dot, a scheme of optically exciting the quantum dot which is expected to outperform all other optical excitation methods. Quantum dots use the biexciton-exciton cascade to generate entanglement, and the performance of the source depends on how the biexciton is generated within the dot. By directly populating the biexciton state of the quantum dot through two-photon excitation, the charge noise is decreased, which reduces both re-excitation of the dot and dephasing over the lifetime of the excited state. Using this method of excitation, we measure single photon purities of 0.9979(3) and 0.9985(2) for the emitted biexciton and exciton photons, respectively. Furthermore, quantum state tomography of the emitted pairs reveals a peak concurrence of 0.87(4), with a count-averaged concurrence of 0.52(3). This represents the first ever quantum state tomography measurement of a nanowire quantum dot excited with this excitation scheme.

One downside of quantum dot-based photon sources is there tends to be some asymmetry introduced unintentionally in the fabrication process. This leads to an energy difference between the intermediate states of the biexciton-exciton cascade, called the fine structure splitting. The fine structure splitting causes the state to precess, so that the state emitted depends on the time between the first and second exciton recombinations. The second technique investigated in this thesis is an all-optical method of eliminating the fine structure splitting. This proposed method uses a pair of electro-optic modulators to shift the

energy of the emitted photons and recover the state emitted by a quantum dot without any fine structure splitting. In this thesis, we demonstrate a lithium niobate electro-optic modulator capable of both increasing and decreasing the energy of photons, depending on their polarization. We show up-conversion of right circularly polarized light with 83.7% efficiency and down-conversion of left circularly polarized light with 80.7% efficiency. This demonstration shows that an all-optical fine structure eraser is feasible, and leaves us well-positioned for an experimental demonstration in the near future.

Acknowledgements

I would like to acknowledge everyone who made this thesis possible. First, I would like to thank Dr. Michael Reimer for his excellent supervision and guidance, as well as for the freedom to change my research as I saw fit. I'd also like to thank members of the Quantum Photonics Devices group for their help and valuable discussions. Michael Kobierski for teaching me the foundations of optics experiments and the background covered in Chapter 4. Arash Ahmadi for designing the experiment in Chapter 3 and Mohd Zeeshan for helping with running the experiment. Matteo Pennacchietti for his assistance in the experiment featured in Chapter 5. Nachiket Sherlekar, Burak Tekcan, Divya Bharadwaj, Lin Tian, Brad Van Kasteren and Sasan Vosoogh-Grayli for valuable discussions and feedback.

I'd also like to thank my family and friends. In particular, my parents, Bobbi and John, for their support throughout this degree. And finally my friends, too numerous to list here, for greatly improving my time in Waterloo.

Table of Contents

List of Tables x

List of Figures xi

1 Introduction 1

1.1 Quantum Information . . . 3

1.2 Photons as Information Carriers . . . 6

1.2.1 Polarization . . . 7

1.2.2 Measurement . . . 10

1.3 Bipartite States and Entanglement . . . 12

1.3.1 The Density Matrix . . . 14

1.3.2 Quantifying Entanglement . . . 16

2 Entangled Photon Sources 20

2.1 Photon Source Properties . . . 20

2.1.1 On-Demand . . . 21

2.1.2 Bright . . . 22

2.1.3 Photon Pair Purity . . . 23

2.1.4 Entangled . . . 25
2.1.5 Indistinguishable . . . 26
2.2 Atomic Cascades . . . 26
2.3 Spontaneous Parametric Down Conversion . . . 28
2.4 Quantum Dots . . . 30
2.4.1 Confinement . . . 33
2.4.2 Photon Generation . . . 36
2.4.3 Fine Structure Splitting . . . 38

3 Two Photon Resonant Excitation **41**
3.1 Excitation Schemes . . . 41
3.1.1 Above-Bandgap Excitation . . . 43
3.1.2 Quasi-Resonant Excitation . . . 44
3.1.3 Two-Photon Resonant Excitation . . . 46
3.2 Experimental Setup . . . 49
3.2.1 Pulse Shaping . . . 49
3.2.2 Tomography . . . 52
3.3 Results . . . 54
3.3.1 Rabi Oscillations . . . 54
3.3.2 Single Photon Purity . . . 55
3.3.3 Quantum State Tomography . . . 58

4 Electro-Optic Modulation **62**
4.1 Birefringence . . . 63
4.1.1 The Pockels Effect . . . 65

4.2 Rotating Half-Waveplate . . . 67
4.3 Frequency Shifting . . . 69
4.4 FSS Eraser . . . 71

5 Frequency Shifting **75**
5.1 Electro-Optic Modulator . . . 76
5.1.1 Electronics . . . 78
5.1.2 Standing Wave . . . 80
5.1.3 Travelling Wave . . . 83
5.2 DC Results . . . 84
5.3 AC Results . . . 87
5.3.1 Stability . . . 91

6 Conclusion and Outlook **94**
6.1 Conclusion . . . 94
6.2 Outlook . . . 95

References **97**

APPENDICES **111**

A Tomography Results **112**

List of Tables

4.1 Conversion between i, j indices and l index. 66

4.2 A summary of the outputs of a rotating half-waveplate. 71

List of Figures

1.1 Polarization ellipse of the state $\frac{|H\rangle+e^{i\frac{\pi}{4}}|V\rangle}{\sqrt{2}}$. 8

1.2 Ellipticity angle χ and orientation angle ψ of a polarization ellipse. 9

2.1 Fidelity vs. pair production probability for a probabilistic source. 30

2.2 SEM image of a typical InP nanowire waveguide. 33

2.3 Emission wavelength of a single exciton in the quantum dot. 36

2.4 The biexciton-exciton cascade. 38

2.5 The biexciton-exciton cascade with non-zero fine structure splitting. 40

3.1 Broadband emission spectrum of the quantum dot and nanowire. 42

3.2 Spectra of the quantum dot s-shell under the three excitation schemes. . . 45

3.3 Resonant two photon excitation of the quantum dot biexciton state. 47

3.4 The pulse shaper used to decrease the linewidth of the excitation laser. . . 50

3.5 Laser linewidth before and after the pulse shaper. 51

3.6 Setup for the tomography experiment. 53

3.7 Population of the biexciton state as measured by photon flux. 55

3.8 Measured exciton and biexciton autocorrelation as a function of time delay. 56

3.9 Circular basis correlation counts of the exciton and biexciton photons. . . . 58

3.10 Concurrence of the two-photon state during the lifetime of the quantum dot. 60

4.1 Polarization ellipsoid and ellipses of $LiNbO_3$. 65

4.2 Diagram of the fine structure eraser using two EOM devices. 74

5.1 Cross-section of the $LiNbO_3$ EOM device. 76

5.2 Simulated electrostatic potential in the EOM. 77

5.3 Electrical components involved in driving the EOM. 79

5.4 The three electrical configurations for the EOM device. 80

5.5 Measured reflected and transmitted signals for the EOM operating in standing wave mode. 82

5.6 EOM setup for DC testing. 84

5.7 False colour image of the waveguide and $LiNbO_3$ chip. 85

5.8 Ellipticity angle χ and orientation angle ψ of light output from the EOM. . 86

5.9 EOM setup for AC experiment. 88

5.10 Frequency shifting of light from a narrowband diode laser. 89

5.11 Conversion efficiency of the EOM device over time. 92

Chapter 1

Introduction

Quantum information processing is a rapidly developing field that promises to revolutionize computing in the coming years. Already, there exist quantum algorithms that can efficiently solve problems that are intractable for classical computers. However, these algorithms currently only exist in theory and cannot be implemented until a large-scale quantum computer is built. Building a quantum computer capable of performing meaningful calculations is extremely difficult, since even tiny amounts of noise can introduce errors to the system and error correction is much more difficult compared to the classical case.

Currently, there exist many candidates for implementing quantum computing, including superconducting qubits [1], trapped ions [2], nitrogen-vacancy centres in diamond [3] and NMR-based quantum computing [4]. Different implementations have benefits and drawbacks, and it is currently unclear which implementation will become the industry standard in the future. One commonality between these implementations is that they have a larger spatial footprint than classical information processing devices. Classical computers operate at room temperature, and nanofabrication has improved to the point where tens of billions of transistors can be fabricated per square centimetre. In contrast, quantum information processing devices tend to require bulky supporting infrastructure such as cryostats, large magnets and driving electronics. For this reason, it is not currently feasible to build arbitrarily large quantum computers, and instead it is more practical to build quantum

networks where large problems can be split between smaller quantum computers.

Quantum computing networks work by breaking a large computation problem into smaller pieces and distributing these pieces to smaller, remote quantum computers called nodes that each perform a part of the total calculation [5]. The outputs of the nodes can then be sent elsewhere for further processing or measured to give an output. The nodes of a distributed quantum computing network need to be able to communicate with each other in order to share results from their calculations. This necessitates a way of communicating quantum information quickly and with low loss. Photons have many properties that make them ideal for quantum communication, including their high velocity and low interaction with the environment. While the debate over which implementation is the best for quantum computation is still ongoing, it is clear that photons are the implementation of choice for quantum communication.

In order to produce photons for quantum information processing applications, we need a source capable of generating entanglement, a quantum mechanical property we will discuss later. Entangled photon sources are fundamentally different from light sources most people are familiar with, such as light bulbs. We want our quantum light source to produce exactly two strongly correlated photons in the time it would take a regular light bulb to emit trillions of photons. It is not enough to simply turn the power down to reduce the number of photons; these light source must make use of some quantum mechanical process to produce photon pairs in order for them to be entangled.

This thesis presents results from two techniques that can be used to improve the performance of a quantum light source. The first is a method of triggering our source to emit photons called resonant two-photon excitation (TPE). This method of exciting the source is expected to yield improved performance when compared to other optical excitation schemes. While the method has been implemented on other, similar photon sources [6, 7, 8, 9], this thesis represents the first quantification of entanglement for an InP nanowire/InAsP quantum dot entangled photon source being excited with resonant TPE. The second technique is an electro-optic modulator (EOM) capable of shifting the frequency of photons either up or down, depending on their polarization. The need for this EOM is motivated by a proposal to improve the performance of our photon source even further by tuning the energies of the emitted photons.

This thesis will be organized as follows. In Chapter 1, we will start by discussing the theory of quantum information and how it differs from classical information. We will also discuss how photons are an excellent candidate to implement qubits for quantum communication applications, and define some figures of merit we will use later. In Chapter 2, we will discuss the ideal properties of an entangled photon source, as well as some specific implementations of entangled photon sources. We will introduce the specific device used in this thesis and explain the process by which it generates entanglement. In Chapter 3, we will compare different methods of exciting the photon source and argue why resonant TPE is the superior method. To support this argument, we will then present experimental results showing that resonant TPE improves the performance of the entangled photon source. In Chapter 4, we will shift our focus to discuss the theory of electro-optic frequency shifting, as well as the motivation for doing so. Finally, in Chapter 5, we will present experimental results of an electro-optic frequency shifter, and show that it is suitable to improve the performance of our photon source.

1.1 Quantum Information

Quantum information processing refers to making use of quantum mechanical properties in order to process data and perform computations. In order to understand quantum information and how it is encoded, we will first discuss how information is represented and processed classically. In classical computation theory, the basic unit of information is the binary digit, or bit, which can take on one of two values: either 0 or 1. In classical computation, bits are often encoded using voltages: a low voltage (e.g. 0 V) is considered a 0 and a high voltage (e.g. 5 V) is considered a 1. Classical information is processed by comparing the values of input bits using logic gates, which produce an output bit based on the values of the input bits. At the end of the calculation, the output of the calculation is measured to determine the output state. A measurement of a 0 bit will always give the value 0, and the measurement of a 1 bit will always give the value 1. The output can consist of many bits, which, when all considered together, represent the result of the computation.

In quantum information theory, the basic unit of information is the quantum bit, or 'qubit'. Like a classical bit, a qubit can be in two different states which we call $|0\rangle$ and $|1\rangle$, analogous to the 0 and 1 values of a classical bit. The notation $|x\rangle$ is called a 'ket', and represents a vector with the label x. The two kets $|0\rangle$ and $|1\rangle$ represent a pair of orthogonal eigenvectors, called state vectors:

$$|0\rangle = \begin{bmatrix} 1 \\ 0 \end{bmatrix} \qquad\qquad |1\rangle = \begin{bmatrix} 0 \\ 1 \end{bmatrix}. \tag{1.1}$$

.

The corresponding eigenvalues of the eigenvectors are the possible outcomes when the state is measured. Like a classical bit, a measurement of a qubit in the $|0\rangle$ ($|1\rangle$) state will always yield an output value of 0 (1). In this way, qubits can be used to encode and read out classical data.

In contrast with a classical bit, a qubit can also exist in a linear combination or superposition of the two basis vectors. Such a state $|\psi\rangle$ is written as $|\psi\rangle = \alpha\,|0\rangle + \beta\,|1\rangle$ for some values α and β, which are called the probability amplitudes. The ability to be in a superposition of states is a quantum mechanical property, and is part of what differentiates quantum information processing from classical. Like classical computation, we get the result of a calculation by measuring the value of qubits at the output. However, unlike classical computation, the qubit does not have to be in one of the two basis states; it can be in a superposition of them. The probability amplitudes tell us the probability of measuring the corresponding output when the state is measured. α and β, when squared, give the probability of measuring that the state is in state $|0\rangle$ and $|1\rangle$, respectively. Furthermore, since the probability that the qubit is in *some* state must be unity, we require that the state is normalized such that $|\alpha|^2 + |\beta|^2 = 1$. For example,

$$|\psi\rangle = 0.6\,|0\rangle + 0.8\,|1\rangle = \begin{bmatrix} 0.6 \\ 0.8 \end{bmatrix} \tag{1.2}$$

is a valid qubit, but not a valid classical bit.

A measurement of a qubit does not give full information about the original state of the qubit, it only gives a single bit of information about the probability amplitudes of the state. In addition, after the measurement of a quantum system yields an eigenvalue of the measured property, the system collapses into the corresponding eigenvector. This is what is known as wave function collapse, and makes it impossible to extract any further information about the original state the qubit was in. If we were to measure the qubit in Eq. 1.2, we would measure

$$\begin{cases} 0 & \text{with probability } 0.36, \text{state collapses to } |0\rangle \\ 1 & \text{with probability } 0.64, \text{state collapses to } |1\rangle . \end{cases} \tag{1.3}$$

After the measurement, the state is longer in a superposition of $|0\rangle$ and $|1\rangle$, so we cannot gather any further information about the original state. However, if given many identical copies of the state, we can measure each of them and make an estimate about the original probability amplitudes. For example, if we measure a single qubit in state $|\psi\rangle$ and get an output of 1, our best guess would have to be that the original state was $|\psi\rangle = |1\rangle$. However, if we measure 10 qubits in state $|\psi\rangle$, on average we will measure 0 four times and 1 six times, so our guess for the original state is $|\psi\rangle = \sqrt{0.4}\,|0\rangle + \sqrt{0.6}\,|1\rangle$, which is closer to the actual state. With more identical copies of $|\psi\rangle$, our estimate will narrow in on the original state even further.

In general, probability amplitudes can be complex numbers, so there can exist a phase difference between the $|0\rangle$ and $|1\rangle$ components of a qubit. For example

$$|\chi\rangle = 0.6\,|0\rangle + i0.8\,|1\rangle = \begin{bmatrix} 0.6 \\ i0.8 \end{bmatrix} \tag{1.4}$$

is also a valid qubit and its output when measured would be the same as Eq. 1.3. Quantum states are only defined up to a global phase, so that $|\psi\rangle = e^{i\phi}\,|\psi\rangle$ for any ϕ. The global phase cannot be measured in any way, nor does it have any effect on calculations involving the qubit. Because of this, the global phase is non-physical, and it can be discarded without changing anything about the state. The ability for qubits to encode a phase difference

between the two basis vectors is part of what confers an advantage to quantum computers. It allows algorithm designers to organize input states and quantum logic gates such that the phases of the correct output constructively interfere, while the other outputs destructively interfere. This means that the correct output has a higher probability amplitude and is therefore more likely to be measured.

Single qubits differ from classical bits since they can exist in a superposition of states, and there can exist a phase between the states of the superposition. These differences between quantum and classical information processing seem simple, but have far-reaching consequences. In order to perform quantum information processing, we need something physical that displays both of these phenomena. As mentioned before, photons are an ideal candidate for communicating quantum information. We will now discuss how photons can be used as qubits to store and send quantum information.

1.2 Photons as Information Carriers

Light is already widely used to encode classical bits and send information through fibre-optic cables. Classically, light can be used to communicate information by modulating the phase or amplitude of a stream of photons in order to transfer information. This is the concept behind fibre-optic internet, a technology that has already had a huge impact on classical information transfer speeds. Light is an excellent information carrier for classical communication, since, compared to electrons in copper wire, photons travel very quickly and have much lower signal loss. For the same reasons, single photons are excellent candidates for carriers of quantum information over long distances, such as between nodes in a distributed quantum computing network.

While classical communication uses modulated pulses of light to encode information, quantum communication makes use of single photons to encode quantum information. Information can be encoded in a number of degrees of freedom, including the spatial mode [10], frequency [11], polarization [12] and time of arrival [13]. In this thesis, we will focus on using the polarization degree of freedom of photons for encoding information.

1.2.1 Polarization

Polarization is a quantum mechanical property that describes the orientation of the electric field of a single photon. A single photon is the smallest possible excitation of the electromagnetic field, and consists of oscillating electric and magnetic fields. If the electric field is oscillating in a plane parallel to the floor in the lab frame (which we will define as the x direction), we say it is horizontally polarized, which we label as the $|H\rangle$ state. Conversely, if the electric field is oscillating in a plane perpendicular to the floor (defined as the y direction), we say it is vertically polarized and in the $|V\rangle$ state. As these two polarization states are orthogonal, we can define them as the $|0\rangle$ and $|1\rangle$ states of our qubit:

$$|H\rangle = |0\rangle = \begin{bmatrix} 1 \\ 0 \end{bmatrix} \qquad\qquad |V\rangle = |1\rangle = \begin{bmatrix} 0 \\ 1 \end{bmatrix}. \tag{1.5}$$

.

Since the electric field is oscillating in one plane, if we were able to look at the electric field vector as the photon is travelling directly towards us, we would see it oscillating along a line. For this reason, the $|H\rangle$ and $|V\rangle$ states are said to be linearly polarized.

It is also possible for a photon to have components of its electric field split between the $|H\rangle$ and $|V\rangle$ states. If a photon has equal parts of its electric field in these two states and they are in phase, the polarization is linear and points in a direction 45° relative to the x and y directions. There are two orthogonal states that satisfy this and we call them diagonal and anti-diagonal polarized photons, defined by:

$$|D\rangle = \frac{|H\rangle + |V\rangle}{\sqrt{2}} = \frac{1}{\sqrt{2}} \begin{bmatrix} 1 \\ 1 \end{bmatrix} \qquad\qquad |A\rangle = \frac{|H\rangle - |V\rangle}{\sqrt{2}} = \frac{1}{\sqrt{2}} \begin{bmatrix} 1 \\ -1 \end{bmatrix}. \tag{1.6}$$

$|D\rangle$ and $|A\rangle$ are also linearly polarized states. Looking at a $|D\rangle$ or $|A\rangle$ photon travelling towards us, we would see the electric field vector oscillating in a line, 45° offset from the $|H\rangle$ and $|V\rangle$ states.

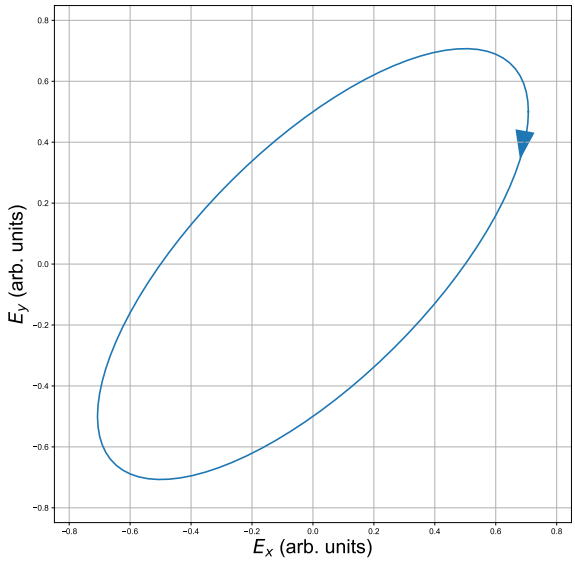

Figure 1.1: Polarization ellipse of the state $\frac{|H\rangle+e^{i\frac{\pi}{4}}|V\rangle}{\sqrt{2}}$.

There is another type of polarization, in which a photon has equal components of its polarization in the x and y directions, but not in phase with each other. This phase difference means that we will no longer see the electric field vector trace out a line as we watch the photon travelling towards us. If the $|H\rangle$ and $|V\rangle$ components are 90° out of phase, we will see the electric field vector rotate in the plane perpendicular to the photon's direction of travel with a constant magnitude. For this reason, we call these states circularly polarized light. By convention, we define right circularly polarized (RCP) and left circularly polarized (LCP) light from the point of view of the receiver. If the photon is travelling directly towards us and the electric field is rotating counterclockwise, it is RCP, and if it is rotating clockwise it is LCP. Mathematically, these are defined as:

$$|R\rangle = \frac{1}{\sqrt{2}}(|H\rangle - i\,|V\rangle) = \frac{1}{\sqrt{2}}\begin{bmatrix}1\\-i\end{bmatrix} \qquad |L\rangle = \frac{1}{\sqrt{2}}(|H\rangle + i\,|V\rangle) = \frac{1}{\sqrt{2}}\begin{bmatrix}1\\i\end{bmatrix}. \tag{1.7}$$

The three pairs of orthogonal vectors we have discussed can each be used to completely describe the polarization state of a photon, since they each span the polarization space.

Any polarization that is not linear or circular is called elliptically polarized, as the electric field traces out an ellipse rather than a line or circle. For example, the state $\frac{|H\rangle+e^{i\pi/4}|V\rangle}{\sqrt{2}}$ will trace out the polarization ellipse shown in Fig. 1.1.

The polarization ellipse can be described by a pair of parameters called the ellipticity angle χ and orientation angle ψ, shown in Fig. 1.2. These are related to the probability amplitudes of a state $\alpha|H\rangle + \beta|V\rangle$ by:

$$\tan(2\psi) = \frac{2|\alpha||\beta|}{|\alpha|^2 - |\beta|^2}\cos(\delta) \qquad \tan(2\psi) = \frac{2|\alpha||\beta|}{|\alpha|^2 + |\beta|^2}\sin(\delta) \tag{1.8}$$

where δ is the phase between α and β (i.e. $\delta = \phi_b - \phi_b$ for $\alpha = |\alpha|e^{i\phi_a}$ and $\beta = |\beta|e^{i\phi_b}$).

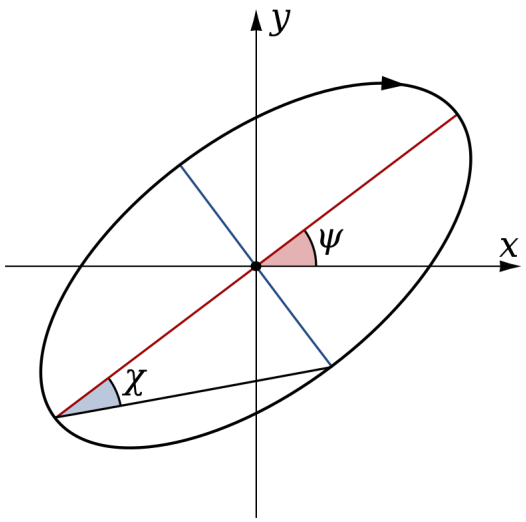

Figure 1.2: Ellipticity angle χ and orientation angle ψ of a polarization ellipse.

The polarization ellipse is a useful tool for visualizing the polarization when it is not in a state easily described in the vector notation. We will use it later when describing how the polarization of a beam of light changes through a device with a continually changing birefringence. However, for most of the discussion in this thesis, it is more natural to use the vector notation.

1.2.2 Measurement

Thus far, we have only discussed the measurement of a quantum state very vaguely. We know that the probability amplitudes give the probability of measuring a certain value, and that the state collapses into the corresponding eigenvector. Chapter 3 uses repeated measurement of a two-photon state to determine the probability amplitudes of the state as a function of time. We will now discuss the measurement process mathematically, in order to understand how this process works.

In quantum mechanics, we extract information about a quantum state through measurement. Any quantity we can measure from a state is called an 'observable', including those used to encode quantum information, such as spatial mode, frequency and polarization. As stated before, it is impossible to extract all the information encoded in a qubit through a single measurement. Instead, we measure a state and get a single bit of information according to its probability amplitudes. After the measurement, the wavefunction collapses into the eigenvector corresponding to the measured eigenvalue. Since the state changes, no more information about the original state can be extracted. This makes quantum measurement fundamentally different from classical measurement, where we can repeatedly measure a state without having any effect on it.

In quantum mechanics, every observable is an operator with a set of eigenvectors and corresponding eigenvalues. The eigenvalues correspond to the possible outcome measurements and therefore must be real numbers. Any arbitrary pure state in the space can be written as a linear superposition of the eigenvectors of the operator. The possible measurement outcomes correspond to eigenvalues of the observable, and the wavefunction will collapse into the corresponding eigenvector upon measurement. This type of measurement is called a projective measurement, since it projects the original qubit onto the state that is measured.

In this thesis, we will measure the projection of a photon in a certain basis vector, ignoring it if we measure the orthogonal vector instead. Most single photon detectors can only measure the presence of a single photon, and not its polarization. Therefore, in order to measure the polarization of a photon, we use a combination of a polarizing filter and a detector. The polarizing filter allows photons in one polarization state (say $|H\rangle$) to pass

through, and absorbs the orthogonal polarization. By placing a single photon detector after the polarizer, we know that the presence of a photon indicates a projective measurement in $|H\rangle$, but the lack of a photon does not indicate a photon in $|V\rangle$.

For example, if we wish to measure the projection in the $|H\rangle$ basis, we use the projection operator defined as $P_H = |H\rangle\langle H|$, where $\langle\psi|$ is called a "bra" and represents the transpose of the state vector $|\psi\rangle$. This bra-ket notation makes it easy to write the inner product between two states $|x\rangle$ and $|y\rangle$ as simply $\langle x|y\rangle$. If we measure the projection of the state defined in Eq. 1.2 in $|H\rangle$, we find:

$$P(H) = \langle\psi| P_H |\psi\rangle = (0.6\langle H| + 0.8\langle V|)(|H\rangle\langle H|)(0.6|H\rangle + 0.8|V\rangle) = 0.6^2 \tag{1.9}$$

$$= 0.36. \tag{1.10}$$

This result agrees with our definition of the probability amplitudes: we have a 36% chance of measuring the qubit in the $|H\rangle$ state. The other 64% of the photons are discarded, since they will be measured to be in the $|V\rangle$ state and absorbed by the polarizing filter.

Importantly, we are not restricted to only measuring a state in the $|H\rangle / |V\rangle$ basis. It is equally valid to measure the projection of the state in any other basis vector, or any other state in the space. For example, the projection of $|\psi\rangle$ along the $|D\rangle$ basis vector is $\langle\psi| P_D |\psi\rangle = 0.98$, and the projection along the $|R\rangle$ vector is $\langle\psi| P_R |\psi\rangle = 0.5$. Measuring in different bases allows us to gain more information about the state than repeatedly measuring in the same basis. As mentioned earlier, the states $|\psi\rangle = 0.6|H\rangle + 0.8|V\rangle$ and $|\chi\rangle = 0.6|H\rangle + i0.8|V\rangle$ will both yield a zero 36% of the time and a one 64% of the time. If measuring just in the $|H\rangle / |V\rangle$ basis, we could measure as many copies of these two states as we want and never be able to differentiate between them. The ability to differentiate between these states comes from also measuring in a different basis, for example $|R\rangle / |L\rangle$. $\langle\psi| P_R |\psi\rangle = 0.5$ and $\langle\chi| P_R |\chi\rangle = 0.98$, so if we find 98% of our measurements in $|R\rangle$ result in the photon passing through the polarizer, we know the state is $|\chi\rangle$ and not $|\psi\rangle$. This process of measuring in a number of bases to re-create the original state is called quantum state tomography, and plays a major role in the results of Chapter 3.

1.3 Bipartite States and Entanglement

Thus far, we have limited our discussion of quantum states to single qubits. We have discussed a few interesting properties of qubits, including superposition, phase and state collapse. However, the true power of quantum mechanics reveals itself when looking at states consisting of two or more qubits. Similar to single qubit states, two-qubit states can exist in a linear superposition of their basis states. Interestingly, it is also possible for two qubits to exist in a superposition of basis states such that it is impossible to write the state of one qubit without also considering the other qubit. The property of two or more qubits having non-separable states is called entanglement, and is a quantum phenomenon with many interesting implications.

First, we will consider two-qubit states with no entanglement present, called separable states. Single qubits occupy a two-dimensional, complex Hilbert space that is spanned by their basis vectors. For photons, this is the space of all possible polarizations. If we have two unentangled qubits that exist in separate Hilbert spaces, we can write their joint state as

$$|\psi_0\rangle \otimes |\psi_1\rangle = |\psi_0\psi_1\rangle \tag{1.11}$$

where $\otimes$ indicates the tensor product. For a set of two classical bits, there are four possible states the bits can be in: 00, 01, 10 and 11. Similarly, the space of a pair of qubits can is spanned by four states: $|00\rangle, |01\rangle, |10\rangle$ and $|11\rangle$. These four basis vectors span the space of all two-qubit states, which is a four-dimensional complex Hilbert space, and qubits can also exist in a linear superposition of these basis vectors. The combined state $|\psi_0\psi_1\rangle$ is a four-dimensional vector describing the combined state of the two qubits. For example:

$$|0\rangle \otimes \frac{|0\rangle + |1\rangle}{\sqrt{2}} = \frac{|00\rangle + |01\rangle}{\sqrt{2}} = \frac{1}{\sqrt{2}} \begin{bmatrix} 1 \\ 1 \\ 0 \\ 0 \end{bmatrix} \tag{1.12}$$

is one possible state vector in the new four-dimensional Hilbert space. Since the vector above can be split into a tensor product of two, two-dimensional Hilbert spaces, it is called a separable state. Separable states are multi-qubit states without any degree of entanglement present, and can always be written as a tensor product of qubits. Additionally, since $|\psi_0\rangle$ and $|\psi_1\rangle$ are both normalized, the product state $|\psi_0\psi_1\rangle$ is as well.

However, there also exist states in the four-dimensional Hilbert space that satisfy the normalization condition but cannot be written as a product of two qubits. For example

$$|\psi^+\rangle = \frac{|01\rangle + |10\rangle}{\sqrt{2}} = \frac{1}{\sqrt{2}} \begin{bmatrix} 0 \\ 1 \\ 1 \\ 0 \end{bmatrix} \tag{1.13}$$

is also a valid state vector in our four-dimensional Hilbert space. However, if one tries to find a pair of qubits whose tensor product is $|\psi^+\rangle$, they will find that no such states exist. This state is therefore said to be entangled, since the state of each constituent qubit cannot be written independently of the other. In fact, $|\psi^+\rangle$ is one of the four maximally-entangled basis vectors that span the two-qubit Hilbert space. This set of four basis vectors is called the Bell states and are:

$$|\phi^+\rangle = \frac{|00\rangle + |11\rangle}{\sqrt{2}} \tag{1.14}$$

$$|\phi^-\rangle = \frac{|00\rangle - |11\rangle}{\sqrt{2}} \tag{1.15}$$

$$|\psi^+\rangle = \frac{|01\rangle + |10\rangle}{\sqrt{2}} \tag{1.16}$$

$$|\psi^-\rangle = \frac{|01\rangle - |10\rangle}{\sqrt{2}} \tag{1.17}$$

.

The Bell states are important states in quantum information processing. For a pair of qubits, the Bell states possess the maximum amount of entanglement. We will cover how

we quantify entanglement in 1.3.2, but for now it can be thought of as how dissimilar a state is from any separable state in the Hilbert space. Two-photon entanglement is an important resource in quantum communication applications, such as superdense coding and quantum teleportation [14, 15]. These schemes both use Bell states to send information in a way that would be impossible with two separable qubits. Therefore, in order to implement either of these schemes experimentally, we want some source that can produce photons in one of the four Bell states.

An interesting implication of entanglement is that a projective measurement of one qubit affects the state of the other qubit, even if they are separated by a great distance. For example, if two people (Alice and Bob) separated by some distance each have one qubit of the $|\phi^+\rangle$ state and Alice measures a 0, the wavefunction will immediately collapse to $|00\rangle$, so Bob will now measure a zero 100% of the time. The value of the measurement will always be perfectly correlated, despite being separated by a large distance. However, since the result of Alice's measurement will always be random, the result of Bob's measurement will also be random, although correlated with Alice's. Although the wavefunction collapse is instantaneous, no information is transferred and so the theory of relativity is not violated.

In contrast to a pair of entangled qubits, consider the same situation with the separable state $\frac{|00\rangle+|01\rangle}{\sqrt{2}}$. Alice is given the first qubit, and when she measures a 0, Bob still has a 50/50 chance of measuring 0 or 1. Alice's measurement had no effect on what Bob measured, since the qubits are separable and a measurement of one qubit does not collapse the wavefunction of the other. In this case, the two measurements will only display classical correlations due to the lack of entanglement.

1.3.1 The Density Matrix

Thus far, we have only discussed quantum states that exist in a single, well-defined state. These are called pure states, since the there is only one possible state and no probability is involved in the initial state. However, it is sometimes the case that the initial state we get is selected from a statistical distribution of possibilities. It is still possible to describe a state like this mathematically, but we need a more general data structure than state vectors: the density matrix.

The density matrix of an n-dimensional pure state $|\psi\rangle$ is an $n \times n$ matrix which we usually represent as ρ, defined as:

$$\rho = |\psi\rangle \langle\psi| . \tag{1.18}$$

For example, for a qubit with state vector $|0\rangle$, the density matrix is

$$\rho = \begin{bmatrix} 1 & 0 \end{bmatrix} \begin{bmatrix} 1 \\ 0 \end{bmatrix} = \begin{bmatrix} 1 & 0 \\ 0 & 0 \end{bmatrix} . \tag{1.19}$$

A mixed state is a probabilistic mixture of pure states. This often arises when a qubit preparation scheme does not always produce the exact same state, but produces states following some probability distribution. For a mixed state consisting of m possible states, where state $|\psi_i\rangle$ has probability of P_i, the density matrix is

$$\rho = \sum_{i=1}^{m} P_i |\psi_i\rangle \langle\psi_i| . \tag{1.20}$$

This is just the sum of the possible density matrices, weighted by their probability. The density matrix is important, as it contains all possible information about a quantum state. To see why the density matrix is important, we will compare two states, one mixed and one pure:

$$|\psi_0\rangle = \begin{cases} |00\rangle & P = 0.5 \\ |11\rangle & P = 0.5 \end{cases} \tag{1.21}$$

$$|\psi_1\rangle = \frac{|00\rangle + |11\rangle}{\sqrt{2}} \tag{1.22}$$

.

The state $|\psi_0\rangle$ is a mixed state consisting of two completely separable states and therefore has no entanglement present. On the other hand, $|\psi_1\rangle$ is one of the Bell states and has the maximum amount of entanglement present. Simply measuring both these states

in the $|0\rangle / |1\rangle$ basis would yield 00 half the time and 11 the other half; the results would be identical. However, looking at their density matrices, we find:

$$\rho_0 = \frac{1}{2}\begin{bmatrix} 1 & 0 & 0 & 0 \\ 0 & 0 & 0 & 0 \\ 0 & 0 & 0 & 0 \\ 0 & 0 & 0 & 1 \end{bmatrix} \tag{1.23}$$

$$\rho_1 = \frac{1}{2}\begin{bmatrix} 1 & 0 & 0 & 1 \\ 0 & 0 & 0 & 0 \\ 0 & 0 & 0 & 0 \\ 1 & 0 & 0 & 1 \end{bmatrix}. \tag{1.24}$$

These two density matrices differ in their anti-diagonal elements. Just measuring in the $|0\rangle / |1\rangle$ basis would not provide enough information to determine what state is present. By reconstructing the density matrix, we are able to differentiate between states that give the same outcomes in a certain measurement basis. As discussed before, this is done through quantum state tomography, which involves repeated measurement in different bases [16]. This is an important process, as the density matrix contains full information about a state, including whether the state is pure or mixed, and the degree of entanglement present.

1.3.2 Quantifying Entanglement

So far, we have only mentioned two specific cases of entanglement between photons: unentangled, separable states and maximally entangled Bell states. These two special cases represent the two extremes of entanglement in a system. It is also possible to lie somewhere between these two extremes, with some amount of entanglement present, but not maximally entangled. We therefore want some way to quantify the 'amount' of entanglement present. For a two-qubit system, we can quantify the entanglement using a value called the entanglement of formation (EF) [17]. This is calculated by finding the Von Neumann entropy of the reduced density matrix of one of the qubits. Essentially, this is telling us how far the reduced density matrix is from being a pure state. By definition, a separable

pure state is a tensor product of two pure states, so the reduced density matrix of either qubit in the separable state will be pure. In contrast, the qubits in an entangled pair cannot be written as a product of pure states and their reduced density matrices will be mixed states. This gives us a way to numerically express how separable or entangled a quantum state is.

Without loss of generality, we will consider the reduced density matrix of qubit A, ρ_A. For a pure state, the entanglement of formation is defined as:

$$EF = -Tr[\rho_A \log(\rho_A)]. \tag{1.25}$$

The EF takes a value in the range [0, 1], with 0 corresponding to a completely separable state and 1 corresponding to a maximally entangled state. For a pure state, the EF can be rewritten as a binary entropy function [18]:

$$EF = -x \log(x) - (1-x) \log(1-x) \tag{1.26}$$

$$x = \frac{1 + \sqrt{1 - C(\rho)^2}}{2} \tag{1.27}$$

where $C(\rho)$ is a value called the concurrence of the bipartite state [19]. Concurrence is a function of the density matrix of a state and is an example of an entanglement monotone. An entanglement monotone is any function that quantifies the entanglement present between a pair of qubits and is a monotonically increasing function of entanglement. Since concurrence is a monotonically increasing function of entanglement and is often easier to calculate than the entanglement of formation, we can use concurrence to quantify the degree of entanglement present in a system instead.

As discussed before, the Bell states form a basis spanning the space of two-qubit pure states, so any bipartite pure state can be written as a linear combination of the Bell states. We can write a bipartite state as $|\psi\rangle = \sum_{i=0}^{3} \alpha_i |v_i\rangle$ where the $|v_i\rangle$ are the Bell states and α_i are the probability amplitudes. For a pure state, the concurrence is defined as

$$C(\rho) = |\sum_{i=0}^{3} \alpha_i^2|. \tag{1.28}$$

For mixed states, the entanglement of formation is more complex. However, there exists a method for calculating the concurrence directly from the density matrix of a bipartite system. For a two-qubit state, that can in general be mixed, the concurrence is calculated as

$$C(\rho) = max(\lambda_3 - \lambda_2 - \lambda_1 - \lambda_0, 0) \tag{1.29}$$

where λ_0-λ_3 are the sorted eigenvalues of the matrix $\sqrt{\sqrt{\rho}\tilde{\rho}\sqrt{\rho}}$ where $\tilde{\rho} = (\sigma_y \otimes \sigma_y)\rho^*(\sigma_y \otimes \sigma_y)$ and ρ^* is the complex conjugate of ρ [17].

For a mixed state, this method of calculating the concurrence is simpler than calculating the entanglement of formation, hence why we will use concurrence as our entanglement monotone instead of the EF. Experimentally, our goal is then to find the density matrix of our state through quantum state tomography of the two-photon states emitted by our source. This allows us to calculate the concurrence of the state and quantify the entanglement present in our system. This gives us a way to compare the performance of different entangled photon sources in terms of the entanglement of the photons emitted.

Another common measure of the entanglement between two photons is the fidelity to a maximally entangled state, often just called the fidelity. In general, the fidelity is a measure of how similar a state is to a known reference state. We choose the reference state to be the nearest maximally entangled state. The fidelity of a state is defined as:

$$F(\rho) = Tr[\rho\rho_0] \tag{1.30}$$

where ρ_0 is the density matrix of the maximally entangled reference state. Both concurrence and fidelity are commonly used as entanglement monotones, and we will use both when quantifying entanglement throughout this thesis. Given a state ρ with concurrence $C(\rho)$, the fidelity to a maximally entangled state is bounded by [20]

$$max\left(\frac{1+C}{4}, C\right) \leq F \leq \frac{1+C}{2}. \tag{1.31}$$

Therefore, the fidelity of a two-qubit state will lie in the range [0.25, 1], and will always be greater than or equal to the concurrence.

Chapter 2

Entangled Photon Sources

2.1 Photon Source Properties

Thus far, we have discussed using individual photons as qubits by encoding information in their polarization degree of freedom. We have also discussed qubit entanglement theoretically without mentioning how it arises physically. In this section, we will discuss devices that can generate pairs of entangled photons and the physical processes behind them.

Entangled photon generation can occur in a number of different ways, such as optical processes in a non-linear crystal or radiative recombination of excited charges. Specific examples of these sources are covered later in the chapter. Every device has advantages and drawbacks, and in order to compare their overall performance, we will first discuss the properties we want in an ideal photon source. An ideal entangled photon source has the following five properties:

1. **On-demand:** photons are produced if and only if the source is triggered by some triggering system.
2. **Bright:** the source produces photon pairs at a high rate.
3. **Photon pair purity:** each time the source is triggered, one and only one pair of photons is emitted by the source.

4. **Entangled:** the emitted pair of photons possess the maximum amount of entanglement.

5. **Indistinguishable:** photons emitted in subsequent excitations have identical properties, such as frequency and spatial mode.

A photon source that satisfies all five of these properties is what we will call an ideal photon pair source. Depending on the application, only some of these properties may be important and others not mentioned here may be relevant as well, but we will focus only on these five. In reality, no photon source meets all the requirements, but this gives us something to strive for. We will now discuss these requirements in more detail and why they are important.

2.1.1 On-Demand

For an entangled photon source to be considered on-demand, it must produce a pair of entangled photons whenever it is triggered. A 'triggering event' is any physical process that can cause the photon source to emit a pair of photons. For example, the trigger can be electrical like a single electron transistor that injects charges into the device or optical like a pulse from a laser. After the photon source is triggered, it must then emit a pair of entangled photons within a short time frame in order to be considered on-demand.

A photon source that operates completely on demand is required for a number of applications, mainly when interference between photons is required. For example, entanglement swapping is a process that exchanges entanglement between two pairs of photons so that two photons that have never interacted with each other are entangled [21]. Entanglement swapping is a requirement for building large-scale quantum networks, and requires photons interfering with each other on a beam splitter. An on-demand source is necessary for deterministic entanglement swapping, since the photons must arrive at the beam splitter at the same time for the entanglement swapping protocol to succeed [22].

There are a few considerations that go into determining if a source is considered on-demand. The first is the source pair efficiency, which is the likelihood that a source will

produce a pair of photons for a single triggering event. Ideally, this value is unity so that we receive a pair of photons every time we trigger the device. However, this is not always the case, since the photon source might be probabilistic or have some mechanism of losing energy without emitting photons. Another important measure is the pair extraction efficiency, which is the percentage of photon pairs produced that are collected by the first lens. This is an important property experimentally, as only photons that are collected can be used in an experiment. If photons are produced but cannot be collected by the optics, the photons are lost and the device cannot be considered truly on-demand. If we multiply the source pair efficiency and the pair extraction efficiency, we get the first lens pair efficiency, which is the fraction of triggering events that lead to a pair of photons being collected by the first lens. For an ideal, on-demand source, the first lens pair efficiency will be unity so that every triggering event leads to a pair of photons being collected by the optics.

2.1.2 Bright

The brightness of a photon source refers to how many pairs of photons the device is capable of producing per second. Since only a single qubit can be encoded in each photon, the rate of communication directly scales with the rate at which we can produce photons. Therefore, we want our entangled photon source to be as bright as possible. The brightness of a source has no upper limit, so there is no ideal brightness for a source, however, we will consider a source operating in the $10^7 - 10^9$ Hz range to be 'bright'.

Classically, light is used to communicate data through fibre optic cables. Although the wavelength and fibre materials are selected to minimize absorption, attenuation still becomes a problem over long distances. Classically, loss is compensated for with repeaters, which amplify the input signal and eliminate the effects of fibre absorption. In quantum communication, if a single photon is absorbed in the fibre, that information is lost entirely and cannot be amplified. Furthermore, the no-cloning theorem states that quantum states cannot be copied [23], which means that a quantum signal cannot be amplified the same way that classical information is. Therefore, attenuation is a major problem for long-distance quantum communication, and classical repeaters cannot solve this problem.

For photons in a fibre, attenuation causes the number of photons to decay exponentially with the length of the fibre, meaning that the distance over which quantum communication is possible is currently limited by the brightness of the source. Entanglement distribution has been demonstrated experimentally through 300 km of optical fibre using time-bin encoded qubits [24], and 144 km in free space using polarization-entangled qubits [25], placing an upper limit on the distance over which quantum information can be sent. These demonstrations had very low photon counts due to attenuation and loss in their respective systems. To overcome this, a technology known as quantum repeaters promises to solve the exponential loss in the communication channels by using entanglement swapping between many nodes [26]. While there exist demonstrations of functioning quantum repeaters, currently no quantum repeater has outperformed direct transmission of photons [27]. Therefore, both the rate of communication and distance to the receiver are currently limited by the brightness of the photon pair source.

For a photon pair source, the important measure of brightness is the photon pair flux, which is the total rate that photon pairs are produced and collected by the optics. This is different from the first lens pair efficiency, as a source may have high efficiency but only support a low repetition rate, leading to a low overall photon flux. While high efficiency (on-demand operation) is desirable, if the overall photon flux is low, the source will be limited in its applications. Therefore, a combination of on-demand operation and high overall brightness is required in an ideal entangled photon source.

2.1.3 Photon Pair Purity

High photon pair purity refers to the fact that the source emits only one pair of entangled photons. An ideal source has zero probability of emitting any photons other than the entangled pair. In practice, however, this is not typically the case. Sources based on electron recombination may get re-excited, leading to multiple pairs of photons being emitted. Sources based on probabilistic, non-linear optical interactions emit a number of photon pairs that follow a Poissonian distribution and therefore have non-zero multi-pair emission.

Photon purity is important for a few reasons. If two pairs of entangled photons are

emitted, the two receivers may receive photons from different pairs. Since photons from different pairs are not entangled, this reduces the overall entanglement of the mixed state. Additionally, an important application of entangled photons sources is quantum key distribution (QKD), which relies on single photon purity to guarantee their security [28]. If an entangled photon source produces two identical copies of a state, an eavesdropper can steal information without being detected, compromising the security of the communication channel.

The single photon purity of a source can be evaluated using the degree of second order coherence $g^{(2)}(\tau)$ [29]. For single photons, $g^{(2)}(\tau)$ is a measure of the probability of detecting a second photon at a time τ, given that the first photon was detected at time 0. $g^{(2)}(\tau)$ is defined as

$$g^{(2)}(\tau) = \frac{\langle n(t)n(t+\tau)\rangle}{\langle n(t)\rangle^2}, \tag{2.1}$$

where $n(t)$ is the number of photons detected at a time t, and angled brackets denote the expectation value. An important case is that of $\tau = 0$, for which $g^{(2)}$ is the probability that more than one photon is detected at the same time. A source of classical light cannot produce pure single photon states, leading to $1 \leq g^{(2)}(\tau) < \infty$, but for a non-classical state $0 \leq g^{(2)}(\tau) < \infty$, so $0 \leq g^{(2)}(\tau) < 1$ is an entirely non-classical zone [29].

For number states, it is convenient to re-write $g^{(2)}(0)$ as

$$g^{(2)}(0) = \frac{\langle n^2\rangle - \langle n\rangle}{\langle n\rangle^2}. \tag{2.2}$$

Therefore, if we treat each photon from the entangled pair separately, $g^{(2)}(0) = 0$ corresponds to perfect single photon purity, since it indicates zero probability of detecting two photons at the same time. The $g^{(2)}(\tau)$ function can be measured experimentally using the Hanbury-Brown-Twiss setup [30]. This gives us a way to test the single photon purity of both photons emitted from a photon pair source. An ideal source has $g^{(2)}(0) = 0$ for both of the photons it emits, indicating a lack of multi-photon emission in a given triggering event.

2.1.4 Entangled

Obviously, a source of entangled photons should emit photon pairs with the highest possible degree of entanglement. The states that satisfy this property are the Bell states, which are the two-qubit states with maximal entanglement and have a concurrence of $C = 1$. In order for our photon pair source to be considered ideal in terms of entanglement, the measured concurrence of the emitted photon pairs should be unity.

There are a number of factors that affect the entanglement of photons emitted by an entangled photon source, some of which are related to other photon source properties. The first lens pair efficiency and photon pair flux are related to the on-demand and brightness properties of the dot, but also influence the measured entanglement of a source. We need to collect both emitted photons in order to measure entanglement between them. If only a single photon is collected, at best no coincidence count will be measured. In reality, photon detectors have dark counts and can detect background light, so single photons from a source can be correlated with background photons with which they share no entanglement. This reduces the overall measured concurrence as the entanglement is drowned out by background. It is therefore important to have a bright source with a high collection efficiency and two-photon flux to overcome any background and measure a high degree of entanglement.

Additionally, the single photon purity affects the measured entanglement of photons from a pair source. If two pairs of entangled photons are generated by the source, it is possible to detect one photon from each pair, which will not be entangled and therefore have no quantum correlations. Again, measuring non-entangled photons reduces the overall measured entanglement and will lead to a reduced concurrence.

One class of entangled photon sources depend on radiative recombination of charges to produce photons. However, photon sources based on radiative decay in a semiconductor environment can have their entanglement reduced through dephasing [31]. These sources are triggered by exciting charge carriers to an higher energy state, which then decay and emit polarization-entangled photons based on conservation of the angular momentum of the charge carriers. However, this decay process is not instantaneous, and the carriers may sit at an intermediate state for some time. During this time, any process that causes the

charges to lose their angular momentum information will lead to dephasing and loss of coherence between the photons [32]. Spin information can be destroyed by the presence of a magnetic field, such as that produced by the movement of nearby free charges [33]. Therefore, to maximize the entanglement present in photons emitted from a semiconductor source, we want to minimize the dephasing over the lifetime of the excited state.

2.1.5 Indistinguishable

Indistinguishability refers to the properties of the photons emitted from subsequent triggering events. As we have discussed before, photons have many degrees of freedom, including polarization, frequency and spatial mode, which can all be used to encode information. In this thesis, we are interested in using the polarization degree of freedom to encode qubits. However, important effects such as quantum interference require photons that are identical in all aspects, not just polarization. Indistinguishability means that all degrees of freedom of emitted photons are the same in subsequent excitations.

Indistinguishability is important for observing quantum interference effects. For example, the Hong-Ou-Mandel (HOM) effect is a non-classical interference effect that occurs when two identical photons enter the two input ports of a 50/50 beam splitter. The two identical photons will always exit the beam splitter together through one of the exit ports, and will never leave different ports. However, if the photons are not identical in all aspects, this effect will not be observed. This is important, as the HOM effect is the physical phenomenon behind many proposals for quantum repeaters [34]. We want our ideal photon pair source to be capable of being part of a quantum repeater, so we want the emitted photons to be identical in all degrees of freedom in subsequent excitations.

2.2 Atomic Cascades

The first sources of entangled photon pairs were based on electrons decaying from excited states in single atoms. The first entangled photon pair source involved heating a sample of calcium to produce a low density gas, then illuminating it with a lamp to excite electrons

in single atoms [35]. The subsequent decay from the excited state emits a photon of energy equal to the difference in the two levels: $\Delta E = \hbar\omega$. If the electron decays from the excited state to the ground state by first decaying to an intermediate state, a pair of photons are emitted.

In 1967, Kocher and Commins demonstrated a photon pair source using the $6^1S_0 \rightarrow 4^1P_1 \rightarrow 4^1S_0$ cascade in calcium, emitting photons of wavelength 551.3 nm in the first step and 422.7 nm in the second [35]. Both the initial and final states have total angular momentum $j = 0$, but the intermediate state has $j = 1$. Therefore, the first decay will emit either a $|R\rangle$ or $|L\rangle$ photon, which have an angular momentum projection in the z-direction of $j_z = \pm 1$. However, in order to satisfy $j = 0$ at the final state, the second decay must produce a photon of the opposite handed polarization. Furthermore, since the j_z value of the electron in the intermediate state is unknown, the recombination occurs in a superposition of the two possible pathways, emitting a photon pair in the state:

$$|\Psi\rangle = \frac{|RL\rangle + |LR\rangle}{\sqrt{2}} = \frac{|HH\rangle + |VV\rangle}{\sqrt{2}}. \tag{2.3}$$

In the $|H\rangle\,/\,|V\rangle$ basis, this state is the Bell state $|\phi^+\rangle$, and therefore has the maximum amount of entanglement possible. The two photons emitted were predicted to be polarization-entangled, but due to their low count rate, Kocher and Commins could not test this experimentally. However, they were able to measure correlations between the photon polarizations and found the emitted photons were linearly polarized in the same direction. While this does provide evidence that the photon source was working as intended, the correlations observed were not strong enough to rule out classical correlations without entanglement.

Later, in 1972, Freedman and Clauser performed a measurement of photon entanglement using a similar source based on the same cascade in calcium [36]. The innovation of Freedman and Clauser was to measure the polarization correlations in a number of bases, not just parallel and perpendicular. From this, they were able to show the state emitted displayed correlations that could not be explained classically and must be attributed to entanglement.

Unfortunately, sources based on atomic cascades in rarefied gases have many problems. The low density required to isolate single atoms reduces the probability of exciting an atom, limiting the brightness of the source. Additionally, since atoms emit photons isotropically, only a small fraction of emitted photons can be collected by the optics and the probability of detecting both of the emitted photons from the cascade is even smaller. These compounding factors lead to very low brightnesses of atomic cascade photon sources. Kocher and Commins required 21 hours of data collection just to show some degree of polarization correlation, and Freedman and Clauser's experiment required an integration time of 200 hours to show a violation of the classical limit. Clearly, atomic cascades in rarefied gases are not bright enough to use in quantum information processing applications, excluding them from the discussion of an ideal photon source.

2.3 Spontaneous Parametric Down Conversion

Around the same time that atomic cascade sources were being used in quantum optics experiments, another class of entangled photon sources was being developed. These sources are based on spontaneous parametric down conversion (SPDC), a non-linear optical process observed in certain crystals. First predicted in 1961 [37], SPDC uses a pump laser and a non-linear crystal to produce a pair of photons, called the signal and the idler photons. While the full theory of SPDC is outside the scope of this thesis, we will briefly discuss how these sources are used to generate entanglement.

In a linear crystal, the only possible output frequency is that of the input beam, corresponding to regular transmission of light through a medium. However, some crystals exhibit non-linearity in their electric susceptibility χ, which allows solutions to the wave equation with different frequencies than the input. This means that an incident photon at one frequency may be converted into a pair of photons with lower frequencies. However, SPDC cannot create photons of arbitrary frequencies and the photons must satisfy two conditions:

$$\hbar\omega_{pump} = \hbar\omega_{signal} + \hbar\omega_{idler} \tag{2.4}$$
$$\vec{k}_{pump} = \vec{k}_{signal} + \vec{k}_{idler}. \tag{2.5}$$

These two equations are called the phase matching conditions and arise from conservation of energy and momentum [38]. To conserve momentum, the output photons will emerge at an angle, such that the vector sum of their momenta is equal to that of the input photon. This leads to the two photons emerging from the crystal along the surfaces of a pair of cones called emission cones. For a certain class of non-linear crystals, called type-II, the cones consist of photons of opposite polarization [39]. Interestingly, at the intersection of these cones, the individual photon polarizations are in a superposition of the two possibilities. This corresponds to the Bell state $|\psi^+\rangle$, which is a maximally entangled state.

Unfortunately, SPDC is a probabilistic process, and down-conversion of a single photon into an entangled pair occurs with a low probability. Strong laser pulses are required in order to observe the non-linearity required for SPDC and unfortunately, there is a trade-off. Too strong a pulse and there is a non-negligible chance of down-converting more than one photon, leading to multi-pair emission. Too weak a pulse and the probability of SPDC occurring is low, leading to low brightness. This trade-off is characteristic of probabilistic sources; the number of photon pairs produced follows a Poissonian distribution, and we can never simultaneously maximize the brightness and photon pair purity. Fig. 2.1 shows the maximum measured fidelity of a photon pair as a function of the pair production efficiency [40]. The upper right corner represents an ideal photon source with unity pair production efficiency and fidelity, but is mathematically forbidden for probabilistic sources.

SPDC-based entangled photon sources are currently the state of the art, and satisfy some of our requirements for an ideal single photon source. SPDC sources are capable of producing photons pairs with high concurrence [41] and high indistinguishability [42]. Unfortunately, SPDC source are not on-demand and suffer from a trade-off between their pair production efficiency and photon pair purity. While both of these properties can be optimized individually, an ideal source is capable of optimizing them simultaneously.

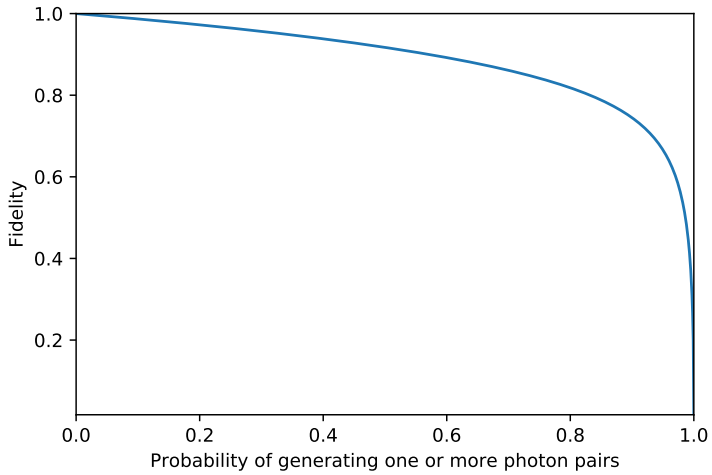

Figure 2.1: Fidelity vs. pair production probability for a probabilistic source.

2.4 Quantum Dots

Clearly, in order to make an ideal source of entangled photons, we need to use a deterministic process, rather than a probabilistic one. Inspired by early sources based on atomic cascades, quantum dots use a radiative cascade to produce entanglement between photons. However, in contrast to single atoms, quantum dots can be grown deterministically and integrated into photonic nanostructures to improve the low excitation probability and out-coupling issues faced by atomic gasses.

Quantum dots are small clusters of a semiconductor with a lower bandgap than the surrounding material. The bandgap difference forms a confining potential for both electrons and holes, creating a spectrum of bound states for both charge carriers. Radiative recombination of charges in these bound states produces single photons, with a polarization depending on the angular momentum difference between the initial and final energy state. Like in an atomic cascade, if the decay occurs through an intermediate state, a pair of photons are emitted. We select the initial, intermediate and final states such that the photons emitted are in one of the four Bell states and are therefore fully entangled.

Early quantum dot sources were based on self-assembled quantum dots, which form

due to a lattice mismatch during molecular beam epitaxy [43]. The lattice mismatch leads to strain, which builds as more epitaxial layers are deposited. Eventually, the strain causes the material to stop being deposited epitaxially, and instead bunch up, forming quantum dots. Quantum dots formed this way are called self-assembled quantum dots, and their distribution is random on the surface of the material. They are then covered by a semiconductor with a larger bandgap to protect the dot and form the potential well. Unfortunately, embedding the QDs in a material with a higher refractive index than air leads to total internal reflection of emitted photons, reducing the pair extraction efficiency. This, coupled with the isotropic emission from bare self-assembled QDs, means that only a small fraction of emitted photons can be collected by the first lens, leading to very low overall brightness [44]. Despite this, polarization correlations were still observed in the photons emitted from these types of sources [45, 46]. The main challenge then became improving the brightness of QD-based sources by improving the directionality of photon emission and reducing internal reflections. It was soon realized that this could be achieved by integrating quantum dots into nanostructures.

There exist a wide variety of nanostructures that improve the brightness and collection efficiency of quantum dots. These structures include photonic structures such as microlenses [8] and nanowires [47], which improve the directionality of the emission, as well as many types of cavities [48, 49, 50] which can both enhance the rate of emission and improve the directionality of emission. These nanostructures have been extremely successful at improving the brightness of quantum dot photons. The use of a photonic structure to enhance the brightness of a quantum dot source was first demonstrated by Dousse et al. in 2010 [50]. They used a pair of photonic microcavities, called a 'photonic molecule' to achieve a first lens pair efficiency of 0.12. Within a few years, Müller et al. demonstrated a quantum dot embedded in a planar cavity with a photon pair generation rate of 0.86(8) [48]. In 2018, Wang et al. demonstrated a bullseye cavity with a pair generation rate of 0.59(1), along with a pair extraction efficiency of 0.62(6) for a first lens efficiency of 0.36 [51]. This is orders of magnitude larger than the efficiencies achieved with bare, self-assembled quantum dots. Additionally, Wang et al. measured $g^2(0)$ values of 0.014(1) and 0.013(1) for the two emitted photons. This combination of pair extraction efficiency and single photon purity can only be achieved by a deterministic photon source.

The improvement in photon pair extraction efficiency and therefore brightness has enabled the measurement of other important photon source performance metrics. Photon indistinguishabilities greater than 95% are routinely measured from quantum dots in a variety of different nanostructures [8, 49, 52, 53], with the connected pillar QD source of Somaschi et al. achieving an indistinguishability of 0.9956(45) [54]. This device acted only as a single photon source and not as a source of entangled photons, but quantum dot sources have also been shown to be excellent sources of entangled photons, as demonstrated by their high entanglement fidelities. A fidelity of 0.9369(4) has been achieved with an optical antenna [55] and a value of 0.95(1) was reached using a microlens structure [8]. In 2021, Schimpf et al. demonstrated a quantum dot embedded in a planar cavity with a fidelity as high as 0.987(8), and a concurrence of 0.95(2) [56]. Additionally, quantum dot-based sources have been shown to have excellent single photon purity, with $g^2(0)$ values less than 1% being reported for a wide variety of nanostructures [9, 49, 54, 52, 57]. In 2018, a raw $g^2(0)$ value of 7.5×10^{-5} was reported by Schweickert et al. using a quantum dot embedded in a planar cavity [58]. In an ideal setup without dark counts or background, a probabilistic source would have to operate at a pair production efficiency of on the order of 10^{-4} to achieve the same value of $g^2(0)$.

While there exist many nanostructures that improve the brightness and collection efficiency of quantum dots, in this thesis we will focus on quantum dots embedded in nanowires. A photonic nanowire is a thin protrusion of a semiconductor with an index of refraction greater than that of the surrounding material. Nanowires are grown using the vapour-liquid-solid (VLS) method, in which the semiconductor constituents dissolve from the gaseous form into a catalyst and subsequently crystallize to form a one dimensional nanowire [59]. By briefly varying the vapours present in the chamber during growth, a different material can be integrated part way along the nanowire. If this semiconductor has a lower bandgap than the bulk nanowire material, it will act as a three-dimensional confining potential: a quantum dot. For example, by adding arsenic vapour briefly during the growth of an InP nanowire, an InAsP quantum dot will be embedded into the nanowire. This is the structure we will consider in this thesis.

The nanowire acts as a waveguide, so photons emitted from the quantum dot are coupled into a narrow spatial mode, improving collection efficiency and therefore brightness. Furthermore, by modifying the growth conditions for the last portion of nanowire growth, a taper can be introduced to the end of the nanowire [61]. The gradual tapering of the nanowire allows the waveguide mode to expand adiabatically into free space. This minimizes reflections at the end of the nanowire, improving the outcoupling efficiency of the nanowire [47, 62].

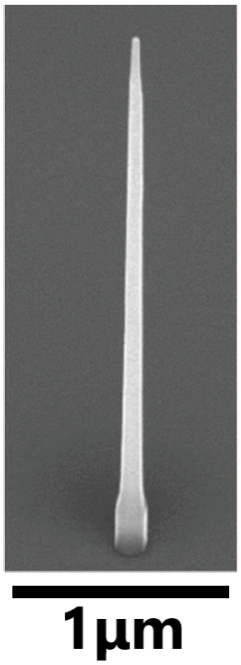

Figure 2.2: SEM image of a tapered InP nanowire waveguide. The quantum dot is embedded 200 nm from the base. Image from [60] licensed under CC BY 4.0.

2.4.1 Confinement

The discrete bound states of the quantum dot enable single photon production. Quantum dots provide a confining potential for both electrons in the conduction band and holes in the valence band, leading to discrete allowed states for both these charge carriers. Radiative decay from bound excited states to the ground state is the process behind photon production in a quantum dot based source. Both electrons and holes are confined to a small region of space since they are of opposite charge, they form a bound state called an exciton, consisting of a single electron and a single hole. Upon recombination of an exciton, a single photon is emitted. Therefore, in order to emit a pair of photons, we will populate a state of the dot with two excitons: a biexciton.

In an atom, the nucleus produces a potential well, which allows discrete energy solutions for electrons. Quantum dots are sometimes referred to as artificial atoms, since the confining potential from the bandgap difference also allows a spectrum of bound states. For photon generation using a quantum dot, we are interested in the lowest energy bound state for both electrons and holes, which is analogous to the s-shell of an atom. Like an atomic s-shell, this state is non-degenerate except for spin degeneracy and can therefore

fit only two electrons and two holes. Additionally, since it is the lowest energy state in the quantum dot, carriers cannot decay to lower energy states except through radiative recombination.

Since our quantum dot is formed as a section of a nanowire, it can be modelled as a short cylinder, or 'hockey puck'. In the direction of growth of the nanowire, the potential has the form of a 1D finite square well of width L and well depth $\Delta E = E_{g,InP} - E_{g,InAsP}$, where E_g is the bandgap of the material. In the radial direction, the confining potential is of the form of a circular finite square well of radius R. The ground state energies of these potentials can be solved by finding the wavefunction and applying boundary conditions.

In the axial direction, the ground state wavefuction is

$$\begin{aligned} \psi(z) &= \begin{cases} A\cos(k_0 z/2) & |z| \leq L/2 \\ Be^{-\alpha_0(|z|-L/2)} & |z| > L/2 \end{cases} \\ k_0 &= \frac{\sqrt{2m_{qd}E_0}}{\hbar} \\ \alpha_0 &= \frac{\sqrt{2m_{nw}(\Delta E - E_0)}}{\hbar}, \end{aligned} \tag{2.6}$$

where m_{qd} is the effective mass of the carrier in the dot, m_{nw} is the effective mass of the charge carrier in the nanowire, E_0 is the ground state energy in the axial direction and A and B are normalization constants. Applying boundary conditions gives rise to eigenenergies that are solutions to

$$\alpha_0 = \frac{m_{nw}}{m_{qd}} k_0 \tan\left(\frac{k_0 L}{2}\right). \tag{2.7}$$

Similarly, in the radial direction, our wavefunction solutions for the ground state are of the form

$$\psi(r,\phi) = \begin{cases} CJ_0(k_0 r) & r \leq R \\ DK_0(\alpha_0 r) & r > R \end{cases} \tag{2.8}$$

where J_0 is a Bessel function of the first kind and K_0 is a modified Bessel function of the second kind, and 0 is the order of the Bessel function, since we are interested in the ground state, and C and D are normalization constants. Continuity of the wavefunction and its first derivative gives us a transcendental equation which can be solved for the eigenenergy of the ground state:

$$k_0 \frac{J_0'(k_0 r)}{J_0(k_0 r)} = \alpha \frac{K_0'(\alpha_0 r)}{K_0(\alpha_0 r)}. \tag{2.9}$$

The energy of the photon emitted upon recombination from the ground states then has energy

$$\Delta E = E_{g,InAsP} + E_{0,e,axial} + \Delta E_{0,h,axial} + E_{0,e,radial} + \Delta E_{0,h,radial}, \tag{2.10}$$

where the e and h subscripts refer to electrons and holes, respectively. Using bandgap and effective mass values from Faria et al. [63], we can numerically find the ground state energy of a single exciton in the quantum dot. This gives us an idea of what wavelength we expect our quantum dots to emit at: the ground state energy of a single exciton is 1.30 eV, which corresponds to a wavelength of 950 nm. This broadly agrees with the nanowire/quantum dot system studied in this thesis, which emits around 893 nm. The discrepancy can be explained by differences in material properties and quantum dot dimensions. The emission wavelength as a function of dot dimensions is shown in Fig. 2.3.

This analysis holds for a single exciton in a quantum dot. However, when a second exciton is formed in the quantum dot, the potential it sees is modified by the presence of the first exciton. This leads to a slight shift in the energy of the biexciton, by a value called the biexciton binding energy ΔE_b. The biexciton binding energy can be positive or negative, and is usually on the order of a few meV [64]. The total energy of the biexciton state can therefore be written as $E_{XX} = 2E_X + \Delta E_b$. The biexciton binding energy is extremely useful, as it allows us to separate exciton photons (with energy E_X) from biexciton photons (with energy $E_{XX} = E_X + \Delta E_b$) spectrally.

2.4.2 Photon Generation

Quantum dots produce photons through radiative recombination of electrons and holes from excited states to the ground state. Photons carry spin angular momentum and have two possible values: $+1$ and -1, working in units of $\hbar$. The angular momenta of $+1$ and -1 correspond to left circularly polarized (LCP) photons and right circularly polarized (RCP) photons, respectively. Angular momentum must be conserved during radiative recombination, so we will now look at the angular momentum of electrons and holes in the lowest energy excited state in an InAsP/InP quantum well.

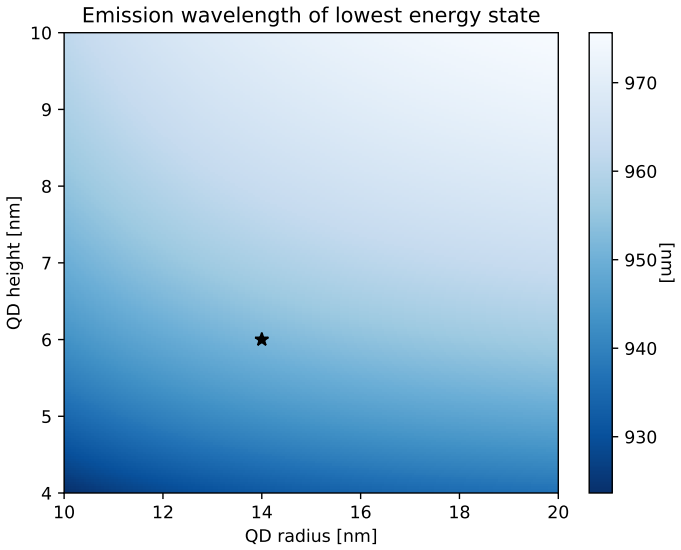

Figure 2.3: Emission wavelength of a single exciton populating the lowest energy excited state of the quantum dot. The black star represents the approximate height and radius of the quantum dot discussed throughout this thesis.

The total angular momentum operator of a charge carrier (either electron or hole) in a semiconductor is:

$$\boldsymbol{J} = \boldsymbol{L_s} + \boldsymbol{L_b} + \boldsymbol{S} \tag{2.11}$$

where $\boldsymbol{S}$ is the spin angular momentum operator, $\boldsymbol{L_s}$ is the operator for the orbital angular momentum of the shell, and $\boldsymbol{L_b}$ is the operator for the intrinsic angular momentum of the band. We are interested in the allowed values of j_z for electrons and holes in the lowest energy excited states of the quantum dot. Electrons and holes are both spin-$\frac{1}{2}$ particles, and since we are interested in the lowest energy excited state, $l_s = 0$. Furthermore, the states at the bottom of the conduction band form s-like states and the states at the top of the valence band are p-like [65], so $l_{b,e} = 0$ and $l_{b,h} = 1$. Therefore, for electrons, the total angular momentum quantum number is $j_e = \{\frac{1}{2}\}$ and for holes the angular momentum quantum number is $j_h = \{\frac{1}{2}, \frac{3}{2}\}$. So, we find that the projection of the total angular momentum in the z-direction is $j_{z,e} = \{-\frac{1}{2}, \frac{1}{2}\}$ for electrons and $j_{z,h} = \{-\frac{3}{2}, -\frac{1}{2}, \frac{1}{2}, \frac{3}{2}\}$ for holes.

The $j = \frac{1}{2}$ holes correspond to the spin-orbit split-off band, the $j = \frac{3}{2}$, $j_z = \pm\frac{1}{2}$ holes correspond to the light hole band and the $j = \frac{3}{2}$, $j_z = \pm\frac{3}{2}$ correspond to the heavy hole band [65]. The heavy hole subband has the lowest ground state energy in the valence band. Therefore, for the quantum dot's lowest energy excited state, we are interested in electrons with $j = \frac{1}{2}, j_z = \pm\frac{1}{2}$ and holes with $j = \frac{3}{2}, j_z = \pm\frac{3}{2}$.

Electrons and holes confined in the quantum dot form bound excitons. Due to the Pauli exclusion principle, two electrons and two holes can populate the lowest energy states in the conduction band and valence band, respectively. An exciton can recombine and emit a photon, so long as the optical selection rule:

$$\Delta j_z = \pm 1 \tag{2.12}$$

is satisfied. $\Delta j_z = +1$ corresponds to emitting a LCP photon and $\Delta j_z = -1$ corresponds to emitting a RCP photon. There are two combinations of electrons and holes that satisfy Eq. 2.12: $j_{z,e} = \frac{1}{2}, j_{z,hh} = -\frac{3}{2}$ and $j_{z,e} = -\frac{1}{2}, j_{z,hh} = \frac{3}{2}$. Therefore, a fully populated lowest energy state of the quantum dot consists of two bright excitons. Additionally, for a fully populated lowest energy state, $j_z = 0$. Note that this decay process is similar to the atomic cascade discussed in Section 2.2: the initial state has $j_z = 0$, the intermediate state has $j_z = \pm 1$ and the final state has $j_z = 0$.

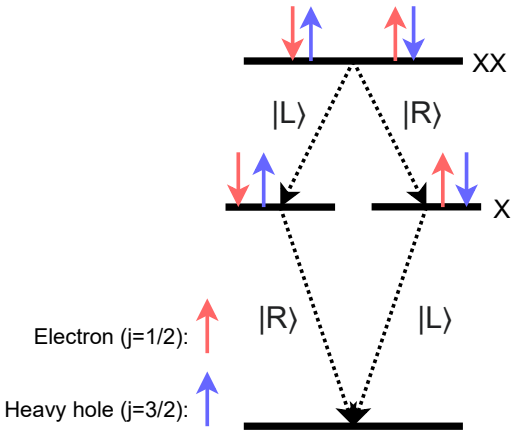

Figure 2.4: The biexciton-exciton cascade. Electron-hole pairs recombine to emit left and right circularly polarized photons. After two subsequent recombinations, an entangled two-photon state is created.

Quantum dots produce entangled photon pairs through what is known as the biexciton-exciton cascade, shown in Fig. 2.4. The biexciton-exciton cascade consists of two consecutive exciton recombinations within the quantum dot. There are two possible pathways that the electrons and holes can recombine: $\Delta j_z = +1$ first (emitting a LPC photon), followed by $\Delta j_z = -1$ (emitting a RPC photon), or $\Delta j_z = -1$ first, followed by $\Delta j_z = +1$. In the absence of which-path information, the intermediate state of the exciton is unknown, and recombination occurs in a superposition of these two pathways [45]. This leads to the same polarization-entangled state as that emitted from an atomic cascade: in the $|H\rangle$ / $|V\rangle$ basis, the quantum dot emits the Bell state $|\phi^+\rangle$ which has the maximum degree of entanglement for a two photon state.

2.4.3 Fine Structure Splitting

Thus far, the discussion has assumed an ideal, perfectly circular quantum dot confining potential. In reality, the potential of the quantum dot will not be perfectly circular. Asymmetries such as an elliptical nanowire cross-section, strain in the dot, and a non-uniform arsenic distribution all lead to an asymmetric confining potential for both electrons and

holes [66, 67, 68]. In this case, the circular symmetry of the system is broken and the eigenstates of the quantum dot system are no longer $|R\rangle$ and $|L\rangle$, but $|H\rangle$ and $|V\rangle$. Additionally, because the confining potential is asymmetric, we no longer expect the energies of these states to be the same. The two intermediate exciton states are split in energy by an amount δ, called the fine structure splitting. This energy difference results in a phase accumulation between the two pathways, depending on the time τ between the biexciton and exciton recombinations. The two-photon state emitted by a quantum dot with non-zero fine structure splitting becomes:

$$|\Psi\rangle = \frac{|HH\rangle + e^{i\frac{\delta\tau}{\hbar}}|VV\rangle}{\sqrt{2}}. \tag{2.13}$$

Expanding this in the $|R\rangle / |L\rangle$ basis, the state becomes:

$$|\Psi\rangle = \frac{|RL\rangle + |LR\rangle}{\sqrt{2}} \cos\left(\frac{\delta\tau}{2\hbar}\right) - \frac{|RR\rangle + |LL\rangle}{\sqrt{2}} i \sin\left(\frac{\delta\tau}{2\hbar}\right). \tag{2.14}$$

Therefore, in the presence of fine structure splitting, the emitted state oscillates between two Bell states: $|\psi^+\rangle$ and $|\phi^+\rangle$ [69]. Fig. 2.5 shows the fine structure splitting in the H/V basis and how it leads to precession between two Bell states in the R/L basis.

The fine structure splitting is an unwanted property of semiconductor quantum dots associated with the fabrication process. Often, we want to send a known state with an entangled photon source. The precession caused by the FSS means the state emitted by the source depends on the time between recombinations. In order to send a known state, we would have to time-gate the emitted photons, leading to a reduction in counts, and removing the on-demand property of quantum dots.

To get information from a photon and make use of its entanglement, it must be detected by a photodetector. Photodetectors have some time resolution, and thus the state detected in each time bin are actually from a range of times depending on the response function of the detector. Slower detectors have a large time uncertainty and can therefore have a small energy uncertainty by the energy-time uncertainty principle. With a high energy precision, the detectors can resolve the energy difference between the two paths, meaning

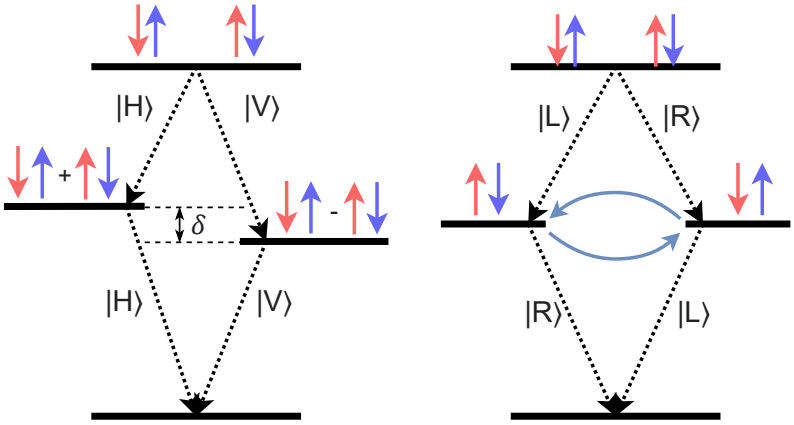

Figure 2.5: The biexciton-exciton cascade in the presence of non-zero fine structure splitting. The system is no longer circularly symmetric and the eigenstates become $|H\rangle$ and $|V\rangle$, with an energy difference between them. When expressed in the $|R\rangle$ / $|L\rangle$ basis, the state precesses as a function of time between the biexciton and exciton recombinations.

the measured entanglement of the source is reduced [33]. Detectors with low timing jitter have high energy uncertainty, and therefore the degeneracy of the exciton state is recovered. Therefore, either reducing the FSS or using detectors with low timing jitter is expected to fix the issue of reduced entanglement in the presence of non-zero FSS.

It is of great interest to minimize or eliminate the fine structure splitting to solve the problems of time-dependent states and reduced entanglement. We will come back to this in Chapter 4, where we will discuss an all-optical method of reducing or eliminating the fine structure splitting. We will now move on to experimental results of the nanowire/quantum dot-based source, discussed theoretically in this section.

Chapter 3

Two Photon Resonant Excitation

In order for a quantum dot to act as a source of entangled photon pairs, we need to populate the lowest energy state with a pair of excitons. There are two general ways this can be done: optically or electrically. Optical excitation uses the electro-optic properties of the dot and surrounding environment to excite electrons to the conduction band and holes to the valence band in order to populate the quantum dot. Optical excitation is relatively easy to implement, as it only requires an external light source; no additional fabrication is required near the source. However, this increases the overall footprint of the source, as tunable excitation lasers tend to be bulky. In contrast, electrical excitation involves using some sort of electrical gate, such single electron transistors or diodes, to inject charge carriers into the dot [70]. This reduces the overall footprint, since no excitation laser is needed, but requires additional fabrication near the dot. The source we are discussing in this thesis has no such electrical gates, and therefore must be excited optically.

3.1 Excitation Schemes

Even within the broad category of optical excitation, there are a variety of excitation schemes with different benefits and drawbacks. The performance of our quantum dot source depends not only on its design and fabrication, but also on how it is excited.

The biexciton state of the quantum dot can be populated optically with a few different schemes. Each excitation scheme uses a different optical transition within the quantum dot or nanowire to excite charge carriers. Fig. 3.1 shows the emission of the quantum dot and nanowire when illuminated by a Coherent Mira 900 Ti:Sapphire laser operating with an energy greater than the bandgap of the nanowire. The emission shows a number of peaks, corresponding to radiative recombination of charges at different energy levels within the nanowire or quantum dot. Each excitation scheme will use one of the spectral features in Fig. 3.1 to generate charge carriers in or near the quantum dot. We will briefly discuss three excitation schemes and compare emission properties of the dot when they are used.

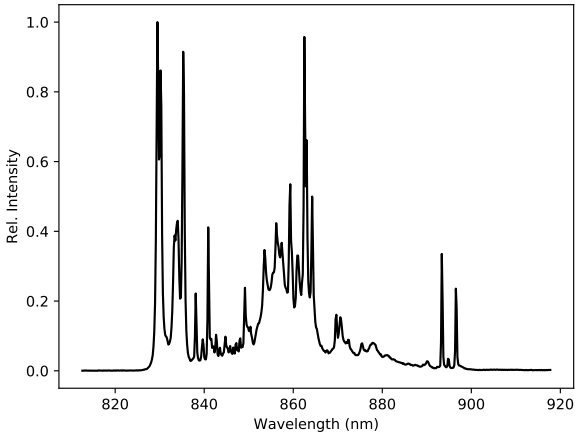

Figure 3.1: Broadband emission spectrum of the quantum dot and nanowire when excited above bandgap with a laser at 780 nm. The quantum dot s-shell is visible as the three rightmost peaks. The relatively small double-peaked feature at 870 nm is associated with acceptor/donor states and is used to populate the quantum dot in quasi-resonant excitation. The peak around 830 nm corresponds to recombinations in the bulk nanowire and tells us the bandgap of the InP.

3.1.1 Above-Bandgap Excitation

The first biexciton excitation scheme is above-bandgap excitation (ABE). In this scheme, the nanowire is illuminated by photons with an energy higher than the bandgap of the InP nanowire. Absorption of a photon excites an electron (hole) from the valence (conduction) band to the conduction (valence) band. Through interactions with lattice phonons, these charge carriers lose energy and decay into the lower energy s-shell of the quantum dot. By exciting an abundance of electrons and holes, we ensure that the biexciton state is populated with near certainty.

Experimentally, this scheme is the simplest to implement, since the only constraint on the excitation laser wavelength is that the photon energies must be larger than the bandgap of InP. Relaxation from the conduction to valence band of InP is the highest energy transition within our nanowire/quantum dot system. From Fig. 3.1, we see that this transition is around 830 nm, indicating that the InP has a bandgap of 1.49 eV. Therefore, when the nanowire is illuminated with a wavelength less than 830 nm, an abundance of charge carriers are produced in the bulk nanowire and may become trapped in the quantum dot potential well through phonon interactions. Due to the abundance of carriers produced, even a relatively low excitation laser power will populate the biexciton state with near certainty.

Although much simpler than other schemes, above-bandgap excitation has a few major drawbacks. The excess free charges produced in the nanowire lead to a fluctuating electric field in the vicinity of the quantum dot. This changing electric field is a source of dephasing, which reduces the degree of entanglement between the two emitted photons [31]. The fluctuating electric field also leads to broadening of the emission lines of the exciton, decreasing the indistinguishability of the emitted photons [71]. Furthermore, the excess of charge carriers means that additional carriers can relax into the dot after the biexciton has recombined but before the exciton has recombined. This can lead to the formation of charged exciton complexes (called trions, either X^- or X^+) or the formation of a second biexciton. The excess of free charges is undesirable in an entangled photon source as it decreases the single photon purity, entanglement fidelity and indistinguishability of the photons emitted. Additionally, the biexciton state is not populated directly and relies on

phonon interactions for charges to decay into the potential well. Since it takes time for the carriers to become trapped in the quantum dot, this increases the total lifetime between laser excitation and emission of both photons. A long lifetime is undesirable, as we must wait for the dot to emit both photons before we can excite it again. This means that a longer lifetime limits the repetition rate of the excitation laser, decreasing the maximum overall brightness of the source.

Fig. 3.2 a) shows the emission of the quantum dot when excited above bandgap. The brightest, rightmost line has previously been identified as emission from the charged exciton X^-. Since an abundance of electrons and holes are created near the quantum dot, there is a high probability of capturing free electrons before the exciton has a chance to decay, leading to trion emission. Additionally, the small, leftmost line is attributed to recombination of the other trion X^+, formed similarly. The peak at 894.108 nm is emission from the biexciton and the peak at 892.667 nm is emission from the exciton. Note that the height of the exciton and biexciton lines are not the same, indicating that each exciton photon emitted does not necessarily have a corresponding biexciton photon.

Above-bandgap excitation does not satisfy all the properties of an ideal quantum dot source. QDs excited above bandgap tend to have high brightness but low single photon purity, entanglement fidelity and indistinguishability. Therefore, this excitation scheme is suitable for identifying bright dots on a sample and aligning optics, but not for applications requiring highly entangled or indistinguishable photons.

3.1.2 Quasi-Resonant Excitation

The second excitation scheme is the quasi-resonant excitation (QRE) of the quantum dot. This scheme uses donor/acceptor states in the nanowire to populate the biexciton state. As shown in Fig. 3.1, the quantum dot has an optical transition around 870 nm that is attributed to the recombination of donor or acceptor-bound excitons within the nanowire [33]. Therefore, by tuning the excitation laser to this energy, these bound exciton states can be directly populated. The bound charges can then decay into the quantum dot and populate the biexciton state without producing an excess of free charges near the quantum dot.

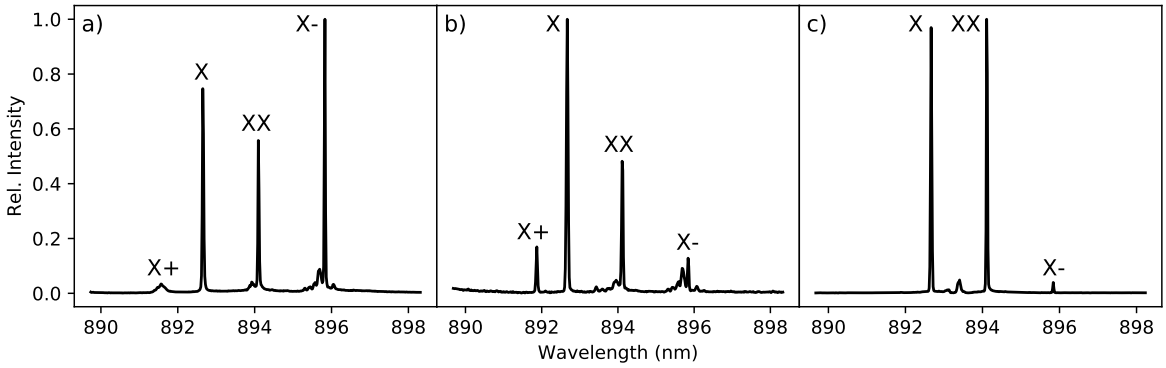

Figure 3.2: Spectra of the quantum dot s-shell under the three excitation schemes. From left to right, the four peaks correspond to X^+ trion, exciton, biexciton and X^- trion emission. a) Above-bandgap excitation. There is significant emission from the X^- trion, due to the abundance of free electrons produced by this scheme. The free electrons can decay into the dot, forming an X^- trion. b) Quasi-resonant excitation. This excitation scheme shows a reduction in X^- emission, due to the reduced number of free charges produced with quasi-resonant excitation. c) Resonant two-photon excitation. This excitation scheme shows minimal trion emission, compared to the other two schemes. The peak at 893.4 nm is residual from the laser that was not fully eliminated by the notch filters. Note that the height of the exciton and biexciton lines are nearly the same, since each biexciton photon has a corresponding exciton photon.

Like above-bandgap excitation, quasi-resonant excitation is not a coherent process and also depends on charge carriers decaying into the ground state of the quantum dot. The benefit of quasi-resonant excitation is the number of free charges is greatly reduced compared to above-bandgap excitation. Since the energy of the excitation laser is less than the bandgap of the nanowire, no free electrons or holes will be excited above the bandgap of the InP. The absence of free charges means there will not be a fluctuating electric field in the local environment of the quantum dot, and therefore less dephasing and spectral broadening. Additionally, the re-excitation probability is lower for quasi-resonant excitation, meaning multi-photon emission is suppressed.

Fig. 3.2 b) shows the quantum dot emission spectrum when excited quasi-resonantly. Again, the four emission lines are observed, attributed to recombination of the biexciton, exciton and both trions. However, in this case, the X^- trion emission is greatly suppressed compared to ABE, and the emission is dominated by the exciton and biexciton recombination. In addition, more emission from the X^+ trion is observed compared to above-bandgap excitation.

Despite the improvement conferred by quasi-resonant excitation of the biexciton state, it is still a suboptimal excitation scheme. Multi-photon emission of the exciton and biexciton transitions are still non-zero, leading to a decreased concurrence of the measured photon pairs. Additionally, the timing jitter of photon emission is still large, since populating the biexciton state still depends on higher-energy states decaying into the QD. Quasi-resonant excitation reduces the dephasing and multi-photon emission issues introduced by ABE [33]. However, there is still room for improvement, especially in regard to the lifetime of the excited state.

3.1.3 Two-Photon Resonant Excitation

The final excitation scheme we will discuss is resonant two photon excitation (TPE) of the biexciton state. In this excitation scheme, the biexciton state of the quantum dot is populated directly through the absorption of a pair of photons, without the need for charge carriers to decay into the dot [72]. Conservation of angular momentum dictates that no single photon process can directly populate the biexciton state, since the biexciton

state has $j_z = 0$ and photons have $j_z = \pm 1$. Therefore, we need a two-photon process to directly populate the QD biexciton state. As discussed previously, the total energy of the biexciton state is $E_{XX} = 2E_X + \Delta E_b$. Because of the biexciton binding energy ΔE_b, the excitation laser energy can be tuned to $E_x + \frac{\Delta E_b}{2}$, and not be resonant with either the $g \rightarrow X$ ($E = E_x$) or $X \rightarrow XX$ ($E = E_x + \Delta E_b$) single photon transitions. This means that $g \rightarrow X$ or $X \rightarrow XX$ re-excitation is unlikely, resulting in very low multi-photon emission for both exciton and biexciton transitions. Instead, this excitation scheme uses a virtual state at $E = E_x + \frac{\Delta E_b}{2}$ to mediate the transition from the ground state to the biexciton state [73].

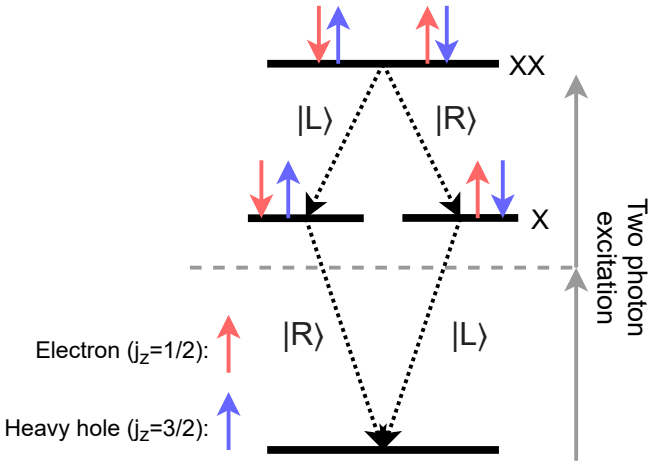

Figure 3.3: Resonant two photon excitation of the quantum dot biexciton state. Simultaneous absorption of a pair of photons directly populates the biexciton state without creating any additional charge carriers.

Additionally, since we are using the lowest energy state in both the quantum dot and nanowire, the excitation laser has too little energy to excite any charges other than those forming the biexciton. Therefore, no photons are absorbed in the nanowire and no free or bound charge carriers are produced in the bulk material. Like the quasi-resonant scheme, this means that charge noise and therefore dephasing in the quantum dot is greatly reduced. Furthermore, since the biexciton is directly excited and does not depend on phonon interactions, the total lifetime of the excited state is reduced compared to the two other

excitation schemes mentioned.

In addition to resonant TPE, there exists a non-resonant variation of two photon excitation. If the laser is slightly blue-detuned from resonance, the dot can be still be populated through phonon-assisted TPE, in which a phonon absorbs the excess energy when the biexciton state is populated [74, 75, 76, 77]. This variation of TPE occurs over a broader range of energies compared to resonant TPE. Additionally, it is less sensitive to power fluctuations, since the population of the biexciton state is a monotonically increasing function of power [76] under phonon-assisted TPE. However, since our dot has a negative exciton binding energy, blue-detuning the laser from resonance brings the excitation pulse closer in energy to the exciton photon. This is undesirable, as it makes off-resonant excitation of a single exciton more likely, reducing the single-photon purity of the emitted exciton photons.

Fig. 3.2 c) shows the dot emission when excited with resonant two-photon excitation. The line around 893.4 nm is residual light from the excitation laser that was not fully suppressed by our experimental setup. Here, the X^- trion emission is suppressed even further, since there is no longer an abundance of free electrons nearby to form an X^- trion. Additionally, the height of the exciton and biexciton lines are nearly identical, since resonant TPE directly populates the biexciton state of the quantum dot, so the dot will emit an exciton photon if and only if it also emits a biexciton photon.

Resonant TPE directly excites the biexciton state of the quantum dot without the need to create additional charge carriers in the QD or nanowire. It is therefore expected to have superior single photon purity and minimal dephasing due to free charges compared to either of the other excitation schemes we have discussed. Furthermore, since it does not depend on charges decaying into the dot, TPE has the smallest lifetime between laser excitation and the second exciton recombining. This shortened lifetime means the dot can be excited more frequently, and therefore has a higher maximum brightness compared to ABE and QRE. We therefore expect resonant TPE to be the optimal scheme for exciting semiconductor quantum dots. Resonant TPE is expected to outperform the other two excitation schemes in terms of single photon purity and entanglement fidelity. To test this, we will compare two figures of merit: $g^2(0)$ and concurrence.

3.2 Experimental Setup

We now move on to the experimental setup used to compare the performance of the quantum dot under different excitation schemes. Specifically, we will focus on the setup for implementing TPE, as it is the most difficult to implement experimentally. The wavelength of the excitation laser must be tuned very precisely to the average energy of the exciton and biexciton. For our experiment, we used a Coherent Mira 900 Ti:Sapphire laser, which is tunable over a wide frequency range and can be operated in both continuous wave and pulsed modes.

3.2.1 Pulse Shaping

To implement TPE, the linewidth of the laser must be much less than the biexciton binding energy ΔE_b to avoid direct excitation of a single exciton in the QD. When the laser was tuned to the average wavelength of the exciton and biexciton photons, the linewidth was found to have a full width at half max (FWHM) of 0.41 nm. This is too broad to use for TPE, as the spectral distribution overlaps significantly with both the exciton and biexciton lines.

To decrease the linewidth of the laser and fine-tune its central wavelength, we designed and built a $4f$ pulse shaper, shown in Fig. 3.4. The pulse shaper was originally designed and built by Jeff Salvail, and used a pair of reflection gratings, one to split the frequencies of the pulse and the other to recombine them after shaping. However, based on advice from Arash Ahmadi, the design was modified to use a single grating to both spatially split and recombine the frequency components of the pulse. The reasoning is that the single grating setup is expected to minimize the amount of chirp present in the pulse. This is desirable, as the presence of chirp in the excitation pulse is expected to prevent optimal excitation of the biexciton state at finite temperatures [78].

In the new design, the pulse shaper first uses a Newport 10HG1200-800-1 reflection grating to split the incident light based on its wavelength. A Thorlabs LA1417-B lens is placed one focal length of 15 cm from the reflection grating, as is standard for $4f$ pulse shapers. The lens focuses the split light on Newport SV-0.5 adjustable width slit

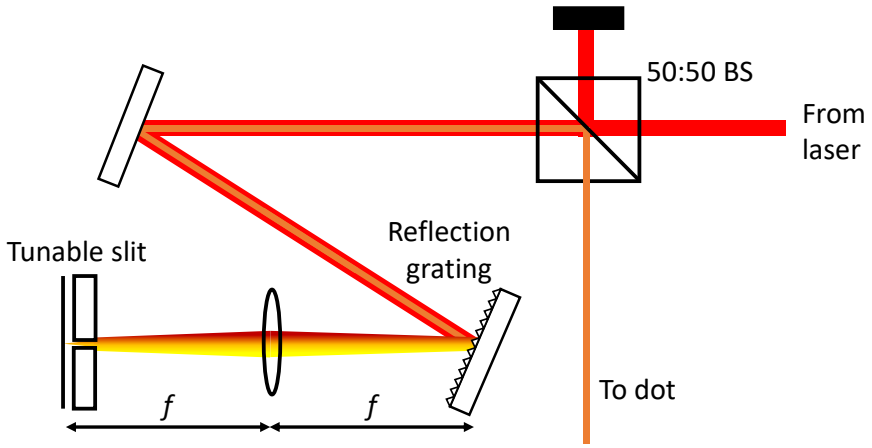

Figure 3.4: The pulse shaper used to decrease the linewidth of the excitation laser. The incoming pulse is split spectrally by a reflection grating and filtered spatially, before being recombined on the same grating.

placed near the focal point. Light of different wavelengths will focus in slightly different positions, so the narrow slit cuts off the edges of the original spectral line. Both the width and horizontal position of the slit can be controlled in order to adjust the width and centre location of the laser spectral distribution. Light that passes through the slit is reflected by a mirror placed just behind the slit and recombined on the same reflection grating, before going to excite the quantum dot. Using the same diffraction grating to both split and recombine the beam is expected to minimize the frequency dispersion of the pulse. Dispersion leads to chirp in the pulse, which reduces the population efficiency of the biexciton state [78].

Using this pulse shaper, we can make the laser linewidth narrow enough that it fits between the exciton and biexciton spectral lines, minimizing off-resonant excitation of either transition. Fig. 3.5 shows the effect of our pulse shaper on the laser spectral distribution. Our pulse shaper setup decreased the spectral FWHM from 0.41 nm to 0.18 nm. Even at low power, the original spectral distribution can be seen overlapping with the exciton line, and would also overlap with the biexciton line at the higher powers required for excitation. This would lead to single-photon excitation of both exciton and biexciton

states, as well as detection of reflected laser light at the same wavelength as the dot is emitting at. Since the laser is much brighter than the dot, this would completely drown out the signal from the dot. However, after pulse shaping, the spectral line is narrow enough that it has negligible overlap with either the exciton or biexciton lines, shown for reference in Fig. 3.5.

Furthermore, our pulse shaper also allows us to fine-tune the centre of the spectral distribution, so it lies exactly on the two-photon resonance of the quantum dot. The pulse shaper moved the centre of our excitation pulse from 893.393 nm to 893.379 nm, closer to the exact resonant wavelength of 893.371 nm. This shift corresponds to a difference of only 0.02 meV, but even this small a change is expected to affect the population efficiency of the biexciton state [76], so the ability to fine-tune the centre wavelength is useful.

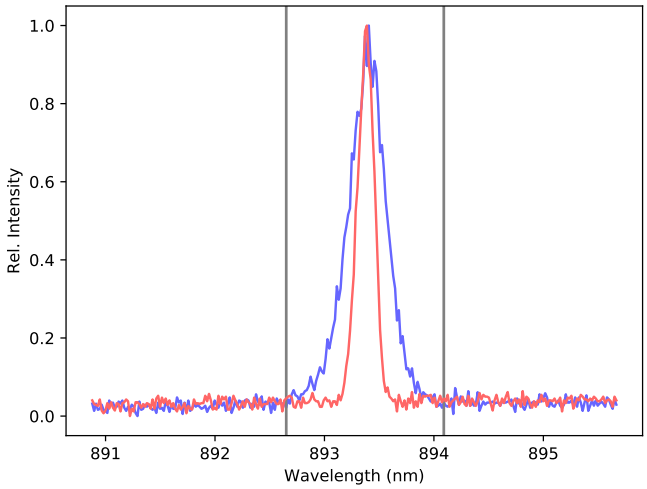

Figure 3.5: Laser linewidth before and after the pulse shaper. The spectral FWHM is decreased from 0.41 nm to 0.18 nm, and the pulse will now fit between the exciton and biexciton lines. The location of the exciton and biexciton lines are shown for reference.

3.2.2 Tomography

After the excitation pulse has passed through the pulse shaper, it is sent through a beam splitter to the quantum dot. The quantum dot is located within an Attocube attoDRY 800 cryostat, and is cooled to approximately 4 K. After excitation, the emitted photons and reflected laser pulse are collected and pass back through the beam splitter and through a series of three OptiGrate BNF-894-OD4 notch filters. These notch filters have a narrow rejection band with a FWHM of 0.4 nm, which can be tuned by adjusting the angle of incidence by rotating the filters. The rejection band is aligned with the excitation laser so that only the photons emitted by the quantum dot continue on to the rest of the tomography setup, shown in Fig. 3.6.

The purpose of the tomography setup is twofold: determine the time between exciton recombination and find the two-photon state of the photons emitted at that time delay. First, both exciton and biexciton photons pass through a Casix WPA1215-$\lambda/4$ quarter-waveplate (QWP) followed by a Casix WPA1215-$\lambda/2$ half-waveplate (HWP) and are then split on a 50/50 beam splitter. One output from the beam splitter goes directly through a Thorlabs LPNIRE100-B polarizer set to allow H polarized light through, which is then coupled into a single-mode optical fibre with a Thorlabs CFC-8X-B lens. Once in the fibre, the photons pass through a WL Photonics WLTF-NM-P tunable optical bandpass filter, which has a transmission FWHM of 0.07 nm. The transmission band of the filter is set to allow transmission of either exciton or biexciton photons. At the output of the bandpass filter, the photons are detected by an Excilitas SPCM-AQRH-16-FC avalanche photodiode. The second output from the beam splitter is sent through a second pair of identical quarter and half-waveplates before encountering an identical polarizer, bandpass filter and detector. Both detectors send their output signals to a PicoHarp 300 time tagger, which builds a histogram of counts as a function of time delay between photon detections.

The two quarter-waveplate/half-waveplate pairs, along with the polarizers and detectors, perform a projective measurement of the polarizations of the two photon state. The first two waveplates take the polarization we want to measure for the exciton photon and transform it into $|H\rangle$. When a $|H\rangle$ photon passes through the polarizer, it will be transmitted 100% of the time, and enter the detector where it will register as a count. As an

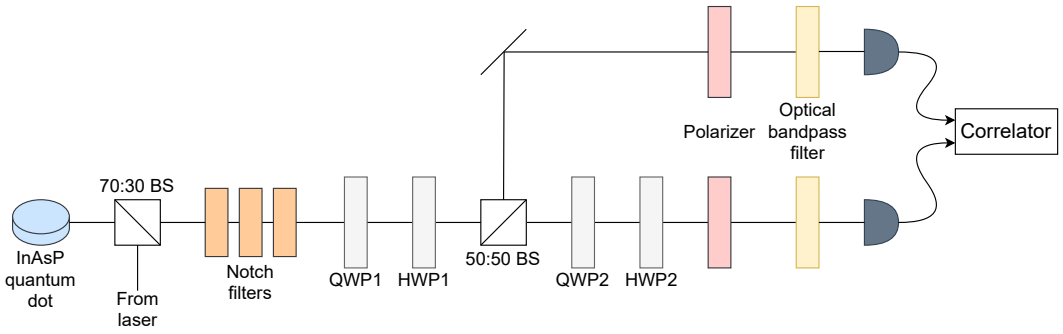

Figure 3.6: Setup for the tomography experiment. The notch filters eliminate light from the excitation laser, so only the exciton and biexciton photons reach the rest of the setup. The two pairs of QWPs and HWPs, along with the polarizers, can perform a projective measurement in any polarization basis, depending on the orientation of the waveplates. The bandpass filters ensure we only collect exciton photons on one path and biexciton photons on the other. From these measurements, the density matrix of the two-photon state can be reconstructed.

example, imagine we are interested in a photon in state $0.6\,|R\rangle + 0.8\,|L\rangle$, and want to measure its projection in $|R\rangle$. To do so, we set QWP1 to $-45°$ and HWP1 to $0°$, to transform the R polarized light into H. After the waveplates, the photon state is $0.6\,|H\rangle + 0.8\,|V\rangle$, and will pass through the polarizer with probability $0.6^2 = 36\%$. This process of setting the waveplates to measure in a certain polarization basis is then repeated along the second path to perform a measurement of the correlation counts between two polarization states. The tunable bandpass filters are set such that only biexciton photons are detected on one path from the beam splitter and exciton photons are detected on the other.

A two-photon density matrix can be fully specified by 15 values. Therefore, a measurement of 15 two-photon polarization states, plus one for normalization, is sufficient to reconstruct the density matrix. However, we will measure correlations in all 36 possible two-photon combinations of $\{H, V, D, A, R, L\}$ and reconstruct our density matrix from that, as it has been shown to yield better results [79]. Since our state is time-dependant, we group our measurements into time bins based on the time between photon detections. From the correlation counts, the density matrix of the two photon state can be recon-

structed at each time step during the lifetime of the excited state. This is achieved with a maximum likelihood algorithm that finds the physical state most likely to have given rise to the measured data [80]. The development and implementation of this algorithm is out of the scope of this thesis, but the interested reader can find more information in Ref. [16]. With the time-dependent density matrix reconstructed, we can calculate the concurrence of the emitted photons over the lifetime of the excited state.

In order to perform a projective measurement of the two-photon state, we need only set the waveplates to transform the polarization we want to measure into $|HH\rangle$, so that it is transmitted by the polarizing filters. The waveplate angles corresponding to the 36 measurements can be found in the Supporting Information of Ref. [33]. In order to automate the process of setting the angles, the four waveplates were each mounted on a Zaber X-RSW60A rotary stage. The angles of the waveplates could then be set programmatically, allowing the entire data collection process of the tomography experiment to be automated.

3.3 Results

3.3.1 Rabi Oscillations

With the laser tuned to the two photon resonance of the dot, the first step is to confirm that the dot is being excited resonantly, without phonon interactions. This is done by looking at the biexciton population as a function of the pump laser energy. In a coherent process, we expect to see Rabi oscillations as the excitation pulse area (proportional to the square root of the excitation laser power) is increased [81, 82, 83]. The Rabi oscillations are fit following the discussion in Ref. [81], modulated by an exponential term as discussed in Ref. [84]. Rabi oscillations are only present when the QD is populated coherently [76, 85], so observation of Rabi oscillations confirms resonant two photon excitation of the biexciton state.

Fig. 3.7 shows the measured biexciton and exciton photon fluxes as a function of pump laser power. Rabi oscillations are clearly visible, indicating that we are resonantly pop-

ulating the biexciton state of the quantum dot, and not relying on phonon interactions (i.e. phonon-assisted TPE). Additionally, Fig. 3.7 reveals the optimal power for achieving population inversion in the quantum dot; the power corresponding to a π-pulse is approximately 1 μW. To maximize counts, we will set the excitation power to this value for all subsequent experiments.

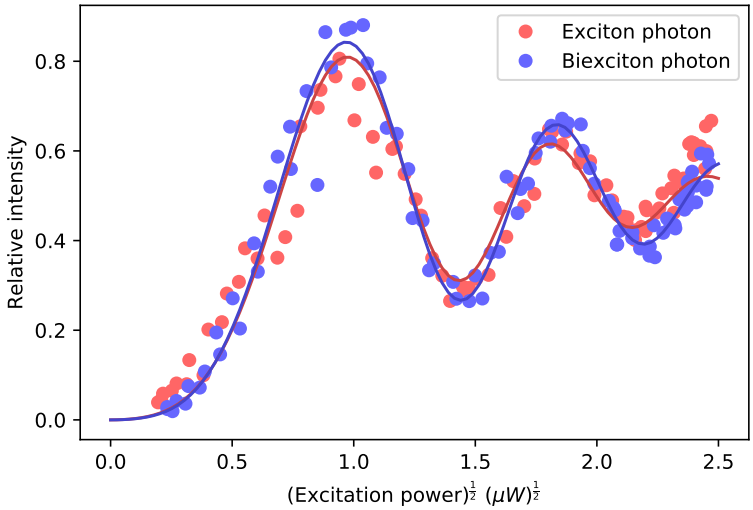

Figure 3.7: Population of the biexciton state as measured by biexciton and exciton photon flux. Rabi oscillations as a function of pulse area indicate coherent two photon excitation of the quantum dot.

3.3.2 Single Photon Purity

One of the major advantages of resonant TPE is the low multi-photon emission probability. This is critical in applications such as quantum key distribution, where multi-photon emission can lead to an eavesdropper stealing information without being detected. In TPE, no extraneous charge carriers are created in the nanowire or higher energy quantum dot states, so the biexciton or exciton states will not be re-populated after recombination. In order to quantify this, the degree of second order coherence ($g^{(2)}(\tau)$) of the exciton and biexciton photons was found experimentally.

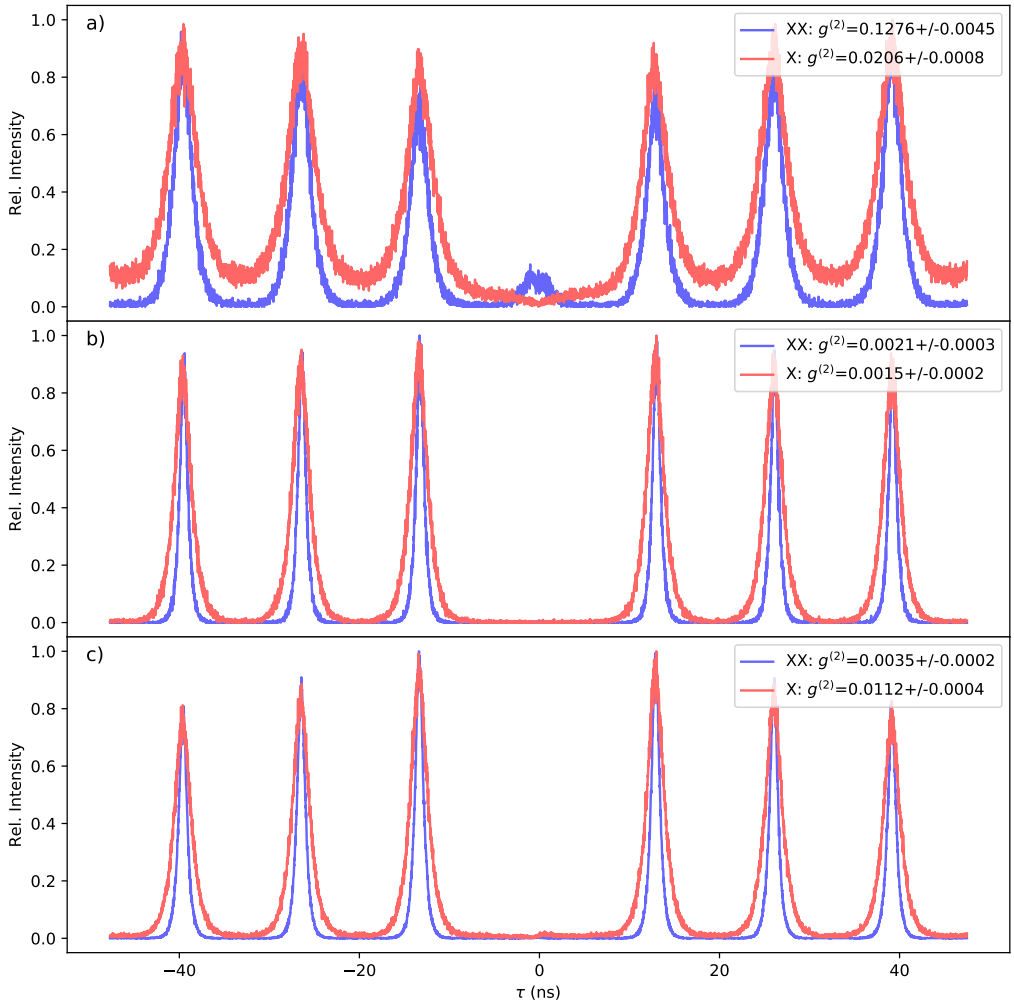

Figure 3.8: Measured exciton and biexciton autocorrelation as a function of time delay. Peaks at 13 ns intervals are from correlating a single photon with one from a subsequent excitation. The features at zero time delay correspond to photons produced from the same pulse. a) Quasi-resonant excitation. The peak at $\tau = 0$ indicates re-excitation of the quantum dot. b) Resonant two-photon excitation. The lack of a peak at $\tau = 0$ indicates a low re-excitation probability and excellent single photon purity. c) Phonon-assisted two-photon excitation. The small peak at $\tau = 0$ is likely reflected laser light at the same frequency the exciton emits at.

The degree of second order coherence is found by correlating the counts of either the exciton or biexciton photons with themselves under pulsed excitation. Each excitation pulse should result in the emission of a single pair of biexciton and exciton photons. Experimentally, this uses the tomography setup discussed before, but modified to operate as a Hanbury-Brown-Twiss setup [30] by removing the polarizers and setting both bandpass filters to pass the same wavelength. This measures the correlations between emitted exciton photons or biexciton photons, regardless of polarization. For optimal single photon purity, the autocorrelation function at zero time delay ($g^{(2)}(0)$) should be zero.

The autocorrelation functions of both photons are shown in Fig. 3.8, for QRE and both resonant and phonon-assisted TPE. ABE was not included in this study, as it has previously been shown to be inferior to QRE, both in terms of single photon purity and measured concurrence of the emitted state [33]. For QRE, the measured $g^{(2)}(0)$ values were 0.1276(45) and 0.0206(8) for the biexciton and exciton photons, respectively. For resonant TPE, the $g^{(2)}(0)$ values were 0.0021(3) and 0.0015(2) for the biexciton and exciton photons, respectively. The value of $g^{(2)}(0)$ under resonant TPE is two orders of magnitude lower for the biexciton photon and one order lower for the exciton photon compared to ABE. This shows a huge improvement in the single photon purity of the source under resonant TPE. For phonon-assisted TPE, the calculated $g^{(2)}(0)$ values are 0.0035(2) and 0.0112(4) for the biexciton and exciton photons, respectively. The exciton $g^{(2)}(0)$ is an order of magnitude larger for phonon-assisted TPE compared to resonant TPE. This is due to the laser being closer in frequency to the exciton emission line, so a fraction of the laser spectral line overlaps with the exciton emission wavelength. A portion of the reflected laser does not get eliminated by the notch filters and is detected as exciton photons, leading to an increased $g^{(2)}(0)$. For this reason, we chose to use resonant TPE for our tomography experiment.

Also of interest is the narrow temporal linewidths for both photons under both types of TPE compared to QRE. This is because TPE directly populates the biexciton state and does not require charges to decay into the QD, which takes time. While the actual lifetime of the biexciton in the QD is the same under both excitation schemes, QRE necessitates waiting a period of time after the excitation pulse for the biexciton to form, which happens immediately for TPE. This enables TPE to operate at a higher repetition rate, increasing

the maximum potential brightness with this scheme.

3.3.3 Quantum State Tomography

In order to show that TPE confers an advantage in regard to entanglement, we need to quantify the entanglement between the emitted photon pairs. For our entanglement monotone we will use concurrence, which ranges from 0 for a state without entanglement present, to 1 for a perfectly entangled state. In order to calculate the concurrence, we need to know the density matrix of the two photon state. As mentioned previously, we will do so by measuring correlations in a set of 36 polarization bases, corresponding to all possible combinations of $\{H, V, D, A, R, L\}$, and reconstructing the density matrix.

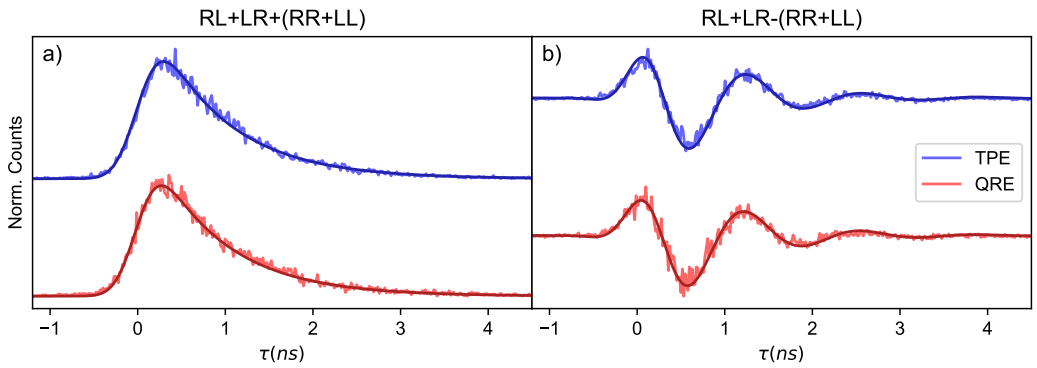

Figure 3.9: Circular basis correlation counts of the exciton and biexciton photons. a) Total two-photon flux of the lifetime of the biexciton. Measured lifetimes are 818(8) ps for TPE and 812(9) ps for QRE. b) Difference between the RL+LR and RR+LL photon fluxes. Oscillations appear due to precession of the state caused by non-zero fine structure splitting. The measured fine structure splitting is 759(4) MHz for TPE and 757(5) MHz for QRE. Neither excitation scheme showed significant dephasing over the lifetime of the biexciton.

Measuring the photon correlations in a number of bases also allows us to measure properties of the quantum dot with high precision. First, if we plot the counts measured in $RL + LR + RR + LL$, we can find the lifetime of the dot. The correlation counts in

this sum represent the total two-photon flux over the lifetime of the dot and by fitting the decaying exponential, we can find the lifetime of the excited state. Fig. 3.9 a) shows the $RL + LR + RR + LL$ correlation counts for both TPE and QRE. From the exponential fits, the lifetime of the biexciton was found to be 818(8) ps for TPE and 812(9) ps for QRE. This agrees with our discussion about the larger linewidths for QRE in Fig. 3.8 being caused by waiting the biexciton to form after the excitation pulse, not from a longer lifetime of the biexciton.

As discussed in Section 2.4.3, the two-photon state emitted precesses between $\frac{|RL\rangle+|LR\rangle}{\sqrt{2}}$ and $\frac{|RR\rangle+|LL\rangle}{\sqrt{2}}$ at a frequency proportional to the FSS, and our correlation counts in the R/L bases will reflect this. Taking the difference between the $RL + LR$ and $RR + LL$ counts, we expect to find an exponentially modified sinusoid at a frequency proportional to the fine structure splitting. Fig. 3.9 b) shows the $RL + LR - (RR + LL)$ correlation counts for both TPE and QRE. From the fits, the fine structure splitting was found to be 759(4) MHz for TPE and 757(5) MHz for QRE. These values are consistent with each other as expected, since the FSS is a property of the quantum dot and not the excitation scheme used.

Of interest when comparing the two excitation schemes is the amplitudes of the R/L oscillations over the lifetime of the dot. The amplitudes should decay exponentially following the lifetime of the dot. If the oscillations damp out faster than this, that is an indicator of dephasing over the lifetime of the biexciton. The counts from the dot under both TPE and QRE show minimal dephasing, as the counts between the $\frac{|RL\rangle+|LR\rangle}{\sqrt{2}}$ and $\frac{|RR\rangle+|LL\rangle}{\sqrt{2}}$ states clearly show oscillations over the entire lifetime of the quantum dot [86]. This is interesting, as it not only shows that TPE leads to minimal dephasing within the dot, but that QRE appears just as good when it comes to minimizing dephasing. This agrees with previous experiments, in which minimal dephasing was observed under QRE over the lifetime of the dot [33].

Since the two-photon state is time-dependent, we reconstruct a time-dependent density matrix by selecting the counts at a number of time steps throughout the lifetime of the biexciton state. At each step, we reconstruct a density matrix by considering all counts within a 50 ps range. From the reconstructed density matrices, we then calculate the

time-dependent concurrence of our state to quantify the entanglement present using Eq. 1.29. The results of this are shown in Fig. 3.10. Resonant two-photon excitation of the quantum dot resulted in a higher peak concurrence of 0.87(4), compared to 0.78(3) for QRE. Additionally, we can calculate a count-averaged concurrence by assigning each time step a weight based on the number of correlation counts detected within the time bin. Doing so, we calculated a count-weighted concurrence of 0.52(3) for TPE and 0.47(3) for QRE. As expected, resonant TPE outperformed QRE in terms of entanglement present in the emitted two-photon state. To our knowledge, this is the first ever measurement of concurrence for a nanowire quantum dot under resonant TPE.

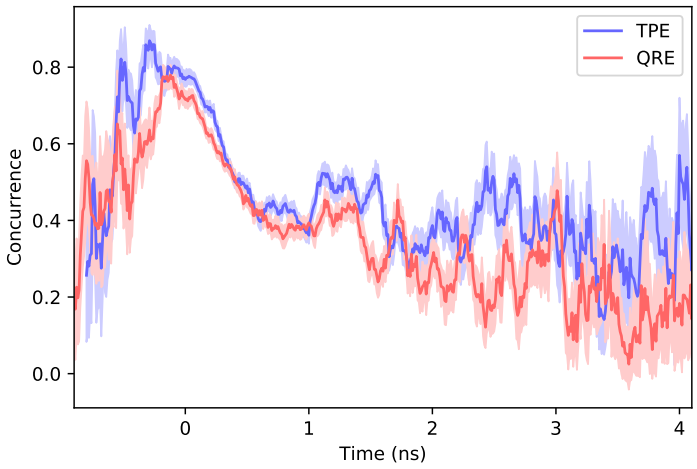

Figure 3.10: Concurrence of the two-photon state during the lifetime of the quantum dot for TPE and QRE. TPE had a higher peak concurrence of 0.87(4), compared to 0.78(3) for QRE. The count-weighted concurrence was 0.52(3) for TPE and 0.47(3) for QR. Errors were assigned based on Poissonian counting statistics and propagated with $n = 30$ Monte Carlo simulations. Error bands represent 1σ confidence.

These results show that TPE yields marginally better results than QRE in terms of entanglement of the emitted photons. As minimal dephasing was observed for both excitation schemes, this difference is likely due to the lower $g^{(2)}(0)$ exhibited by TPE. A low $g^{(2)}(0)$ indicates high single photon purity, so when a biexciton and exciton photon are

detected, we are confident they are from the decay of the same biexciton. The relatively large $g^{(2)}(0)$ of the biexciton under QRE means that a subset of the photon pairs detected are not from the same biexciton, and are not entangled. This leads to a lower overall concurrence for the source under QRE compared to TPE.

As discussed in Chapter 2, the inability to reach unity concurrence has been attributed to the combination of fine structure splitting and detectors with a high timing jitter [33]. In theory, this could be solved by using fast photodetectors, but we would still be left with the issue of precession caused by the FSS. The next two chapters focus on work towards an all-optical method of erasing the FSS of any quantum dot.

Chapter 4

Electro-Optic Modulation

The fine structure splitting of quantum dots arises from asymmetries in the confining potential for electrons and holes. This leads to an energy difference between the two recombination pathways, introducing which-path information when detectors with large timing jitter are used. It is therefore of interest to tune this energy splitting to zero in order to recover a maximally entangled, time-independent state.

Currently, there exist many methods of tuning the fine structure splitting to zero. These methods include applying external electric fields [87, 88, 89, 90], magnetic fields [91], strain fields [92, 93, 94], stress [95, 96], annealing the dot [97] or a combination of these approaches [98, 99]. However, these approaches can typically only compensate for the FSS of a single quantum dot on a sample. For experiments that require more than one source of highly entangled photons, it is desirable to extend FSS erasing capabilities to many quantum dots on a single sample [100]. To do so, we instead consider an all-optical method of removing the fine structure, which acts on the photons after they have been emitted, rather than on the source itself [101]. This means that photons from different sources on the same sample can be sent to different optical FSS erasers and tuned individually.

This all-optical approach of tuning the FSS has a few benefits compared to other methods. This method has the ability to tune the FSS of any dot on a sample, so we can use multiple sources on the same sample. Additionally, it is agnostic to the physical implementation of the source; whether the quantum dot is embedded in a microlens, nanowire,

bullseye grating or any other photonic nanostructure makes no difference, since it acts on the emitted photons and not on the source. This makes it attractive compared to other FSS erasing techniques like strain fields, which experience significant relaxation on scales on the order of 100 nm [92], making them less suitable for tall nanostructures like nanowires.

Our approach to erasing the FSS involves using fast-rotating half-waveplates to shift the energies of the emitted photons in order to correct for the energy difference arising from the fine structure [101]. A waveplate rotating at angular frequency ω will shift the photon energy by $2\hbar\omega$, meaning the waveplate will have to rotate on the order of $10^8 - 10^9$ Hz in order to compensate for a typical FSS. Obviously, it is not realistic to physically rotate an optical component this fast, so a different approach is taken: electro-optic modulation. By modulating the index of refraction of a crystal, we can emulate a fast-rotating half-waveplate without physically rotating an optical component.

In this chapter, we will start by discussing birefringence in a $LiNbO_3$ crystal. We will introduce the linear electro-optic effect, called the Pockels effect, and how it can be used to emulate a rotating half-waveplate in $LiNbO_3$. We will then discuss how a rotating half-waveplate leads to a polarization-dependent frequency shift for photons passing through the crystal. Finally, we will show how this can be used to compensate for the fine structure splitting of a quantum dot.

4.1 Birefringence

In order to understand how we can emulate a half-waveplate using electro-optic modulation, we will first discuss birefringence in general. Birefringence is a property of a material in which the index of refraction depends on the polarization of light passing through it. It is the property used to make quarter and half-waveplates, which are special cases where the difference between the indices of refraction along two perpendicular axes (called the fast and slow axes) leads to a relative delay of exactly $\frac{\pi}{2}$ (for QWPs) and π (for HWPs).

In order for a material to display birefringence, it must display anisotropy in some way. Therefore, the materials we are interested in are typically crystalline in nature, since amorphous materials lack order and tend to be isotropic. In general, any crystal without

a cubic crystal structure can be birefringent, since these materials are anisotropic and light polarized in different directions may experience a different index of refraction. In this thesis, we are specifically interested in lithium niobate ($LiNbO_3$), which is a trigonal crystal.

Since we are discussing anisotropic media, we need a way to describe the optical properties in different directions. We first introduce the permittivity matrix $\boldsymbol{\epsilon}$ and its inverse, the impermeability matrix $\boldsymbol{\eta}$:

$$\boldsymbol{\epsilon} = \begin{bmatrix} \epsilon_{11} & 0 & 0 \\ 0 & \epsilon_{22} & 0 \\ 0 & 0 & \epsilon_{33} \end{bmatrix} = \epsilon_0 \begin{bmatrix} n_{11}^2 & 0 & 0 \\ 0 & n_{22}^2 & 0 \\ 0 & 0 & n_{33}^2 \end{bmatrix} \qquad \boldsymbol{\eta} = \boldsymbol{\epsilon}^{-1} = \frac{1}{\epsilon_0} \begin{bmatrix} \frac{1}{n_{11}^2} & 0 & 0 \\ 0 & \frac{1}{n_{22}^2} & 0 \\ 0 & 0 & \frac{1}{n_{33}^2} \end{bmatrix}. \tag{4.1}$$

The permittivity matrix gives us the electrical permittivity along the x, y and z directions of the crystal. The impermeability matrix allows us to define a geometrical construction called the index ellipsoid

$$\epsilon_0 \sum_{i,j} \eta_{ij} v_i v_j = 1 \tag{4.2}$$

where $\{v_1, v_2, v_3\} = \{x, y, z\}$. The index ellipsoid is used to find the refractive indices seen by the two orthogonal modes of light travelling through the material in an arbitrary direction. If we take the k-vector of a photon travelling through the crystal, then the index of refraction is described by the cross-section of the ellipsoid normal to the k vector. The cross-section is an ellipse and the semi-minor and semi-major axes define the fast and slow axes, as well and the refractive indices in these directions.

We now consider the specific example of $LiNbO_3$, which is a uniaxial crystal with its optical axis in the z direction. With no applied electric field, the equation of the index ellipsoid is:

$$\frac{x^2}{n_o^2} + \frac{y^2}{n_o^2} + \frac{z^2}{n_e^2} = 1 \tag{4.3}$$

where $n_{11} = n_{22} = n_o$ is the ordinary index of refraction and $n_{33} = n_e$ is the extraordinary index of refraction. The index of ellipsoid of $LiNbO_3$ is included for reference in Fig. 4.1.

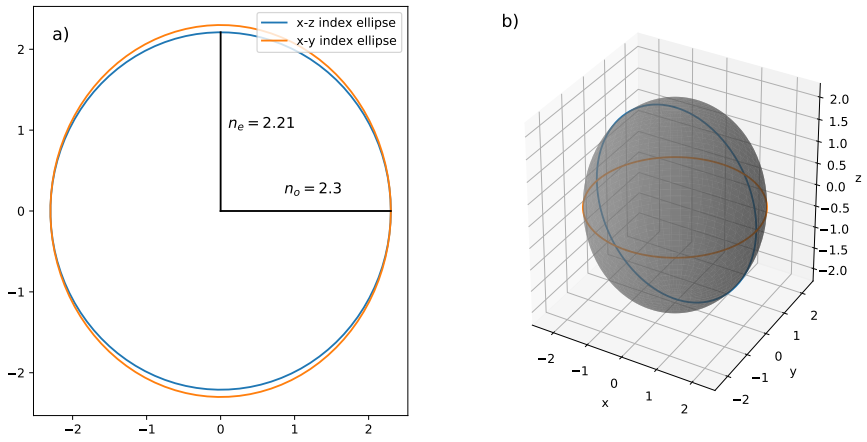

Figure 4.1: Polarization ellipsoid and ellipses of $LiNbO_3$. a) Index ellipses of lithium niobate in the x-y and x-z planes. b) The full index ellipsoid of lithium niobate, with the ellipses from (a) drawn as cross-sections.

4.1.1 The Pockels Effect

We now consider the effect of an applied electric field on the index ellipsoid. The index of refraction depends on the structure of the crystal, which is expected to change in the presence of an external electric field. We therefore expect the index of refraction and the impermeability matrix to be functions of the applied electric field. This implies that the index ellipsoid will change in the presence of an external electric field, which can be used to change the birefringence in the crystal. To emulate a fast-rotating half-waveplate, we need to be able to set the birefringence to act as a half-waveplate at any arbitrary angle. To do so, we will first discuss the effect of a general electric field on lithium niobate.

Certain crystals exhibit a linear change in their refractive index in response to an external electric field. This linear electro-optic effect was first studied by Friedrich Pockels,

and is known as the Pockels effect. By applying an electric field to a material that exhibits the Pockels electro-optic effect, such as $LiNbO_3$, we can induce birefringence in the material. In general, the applied electric field can affect the index of refraction in any direction, not just the direction of the applied field. We can therefore write the impermeability matrix as $\boldsymbol{\eta}(\boldsymbol{E}) = \boldsymbol{\eta} + \boldsymbol{\Delta\eta}(\boldsymbol{E})$, where $\boldsymbol{\eta}$ is defined in Eq. 4.1 and

$$\boldsymbol{\Delta\eta_{ij}}(\boldsymbol{E}) = \sum_{k=1}^{3} r_{ijk} E_k \tag{4.4}$$

is the change in the impermeability introduced by the applied electric field $\boldsymbol{E} = (E_1, E_2, E_3) = (E_x, E_y, E_z)$. The r_{ijk} are called the Pockels coefficients and describe the change in the index of refraction as a function of applied electric field. It appears as though we would need 3 separate 3×3 matrices to fully describe the response of the index of refraction to an applied electric field. However, due to symmetries in $\boldsymbol{\eta}$, $\boldsymbol{r}$ is symmetric under permutations of i and j. Because of this, it is common to replace the two indices i and j with a single index l, as defined in Table 4.1.

j	i = 1	2	3
1	1	6	5
2	6	2	4
3	5	4	3

Table 4.1: Conversion between i, j indices and l index.

Using these new indices, we can write $\boldsymbol{r}$ as a 6×3 matrix. Additionally, we rewrite the impermeability matrix $\boldsymbol{\eta}$ as a 6×1 vector. The change in impermeability due to the applied electric field can now be written as

$$\vec{\Delta\eta} = \boldsymbol{r}\vec{E}. \tag{4.5}$$

Depending on the geometry of the crystal, some Pockels coefficients r_{lk} will be exactly zero, and some will be exactly equal to others. The non-zero elements of $\boldsymbol{r}$ are mea-

sured experimentally. For a trigonal 3m crystal, such as lithium niobate, the change in impermeability is

$$\begin{bmatrix}\Delta\eta_1\\ \Delta\eta_2\\ \Delta\eta_3\\ \Delta\eta_4\\ \Delta\eta_5\\ \Delta\eta_6\end{bmatrix} = \begin{bmatrix} 0 & -r_{22} & r_{13}\\ 0 & r_{22} & r_{13}\\ 0 & 0 & r_{33}\\ 0 & r_{51} & 0\\ r_{51} & 0 & 0\\ -r_{22} & 0 & 0\end{bmatrix} \begin{bmatrix}E_x\\ E_y\\ E_z\end{bmatrix}. \tag{4.6}$$

We can now write the index ellipsoid for a trigonal crystal in the presence of an electric field. In general, the equation of the index ellipsoid is:

$$x^2\left(\frac{1}{n_o^2} - r_{22}E_y + r_{13}E_z\right) + y^2\left(\frac{1}{n_o^2} + r_{22}E_y + r_{13}E_z\right) + z^2\left(\frac{1}{n_e^2} + r_{33}E_z\right) + 2r_{42}E_yyz + 2r_{42}E_xxz - 2r_{22}E_xxy = 1. \tag{4.7}$$

For the present work, we will restrict ourselves to an electric field applied only in the x-y plane and light propagating in the z direction. This means we are interested in the index ellipse in the x-y plane, and how it changes depending on E_x and E_y. We therefore find the index ellipse of z-propagating light to be:

$$x^2\left(\frac{1}{n_o^2} - r_{22}E_y\right) + y^2\left(\frac{1}{n_o^2} + r_{22}E_y\right) - 2r_{22}E_xxy = 1. \tag{4.8}$$

The goal now is to show that we can choose E_x and E_y such that they emulate a rotating half-waveplate.

4.2 Rotating Half-Waveplate

We will now consider the case of sinusoidally varying E_x and E_y, with a 90° phase between the two:

$$\begin{aligned} E_x &= E_0 \sin(\omega t) \\ E_y &= E_0 \cos(\omega t). \end{aligned} \tag{4.9}$$

Because of the xy cross term in Eq. 4.8, we note that the non-zero magnitude of E_x will cause the semi-major and semi-minor axes of the index ellipse to no longer lie along the x and y axes. We define the new principle axes of the ellipse x' and y' as

$$\begin{aligned} x &= x'cos(\theta) - y'sin(\theta) \\ y &= x'sin(\theta) + y'cos(\theta) \end{aligned} \tag{4.10}$$

where θ is the angle between the original axes and the rotated ones. Re-writing the index ellipse in these new coordinates, we find:

$$x'^2 \left[\frac{1}{n_o^2} - r_{22}E_y \cos(2\theta) - r_{22}E_x sin(2\theta)\right] + y'^2 \left[\frac{1}{n_o^2} + r_{22}E_y \cos(2\theta) + r_{22}E_x sin(2\theta)\right] + x'y'[2r_{22}E_y \sin(2\theta) - 2r_{22}E_x \cos(2\theta)] = 1. \tag{4.11}$$

The $x'y'$ cross term is eliminated when $E_y \sin(2\theta) = E_x \cos(2\theta)$, which is true for $\omega t = 2\theta$. Therefore, the angle of the principle axes rotates at a frequency half that of the applied electric field. Setting $\theta = \frac{\omega t}{2}$, we find the equation for the polarization ellipse in the rotating frame:

$$x'^2 \left[\frac{1}{n_o^2} - r_{22}E_0\right] + y'^2 \left[\frac{1}{n_o^2} + r_{22}E_0\right] = 1. \tag{4.12}$$

We can now find the modified indices of refraction along the principle axes of the rotating ellipse:

$$\begin{aligned} \frac{1}{n_{x'}^2} &= \frac{1}{n_o^2} - r_{22}E_0 \\ n_{x'} &= \frac{n_o}{\sqrt{1 - r_{22}E_0 n^2}} \approx n_o + \frac{1}{2}r_{22}E_0 n_o^3 \end{aligned} \tag{4.13}$$

and similarly $n_{y'} \approx n_o - \frac{1}{2} r_{22} E_0 n_o^3$. Therefore, the difference in index of refraction between the fast and slow axes is $\Delta n = r_{22} E_0 n_o^3$. For a waveplate of length l, the retardation of light polarized along the slow axis compared to that polarized along the fast axis is

$$\Gamma = \frac{2\pi l r_{22} E_0 n_o^3}{\lambda}. \tag{4.14}$$

Therefore, we can set the magnitude of the applied electric fields to

$$E_0 = \frac{\lambda}{2 r_{22} n_o^3 l} \tag{4.15}$$

to achieve a $\Gamma = \pi$ delay. The applied voltage which achieves this condition is called the half-wave voltage, and depends on the geometry and optical properties of the device. In conclusion, by applying the sinusoidal drive signals in Eq. 4.9 with the amplitude given by Eq. 4.15, we can create a half-waveplate that rotates at an angular frequency of $\frac{\omega}{2}$.

4.3 Frequency Shifting

So far, we have shown that it is possible to emulate a rotating half-waveplate using a $LiNbO_3$ electro-optic modulator. However, it is not immediately obvious that a rotating half-waveplate will shift the frequency of photons passing through it. Intuitively, it can be thought of as similar to the Doppler shift observed from light reflecting off of a moving mirror. Conservation of momentum dictates that if the momentum vectors of the incident photons and moving mirror point in opposite directions, the frequency of the output light will be increased, and if the angular momentum vectors point the same direction, the frequency of the output light will be decreased. This is called the Doppler effect and is a common example of conservation of momentum.

A rotating waveplate works similarly to a moving mirror to shift light. However, while a moving mirror makes use of conservation of linear momentum, a rotating waveplate makes use of conservation of angular momentum to shift the frequency of the output photons. A rotating waveplate will have an angular momentum vector pointing in either the $+z$

or $-z$ direction, depending on the direction of rotation. For photons, the handedness of circularly polarized light is related to the spin angular momentum (SAM) of the photon [102]. If the SAM vector of the incident photon points in the same direction as that of the rotating waveplate, the frequency of the output photons will be increased, and if the angular momentum vectors point in opposite directions, the frequency of the output photons will be decreased. This is similar to the case of a moving mirror causing a Doppler shift, and therefore is sometimes referred to as the rotational Doppler effect [103]. While this is not a rigorous explanation of the effect, it provides some intuition on how the device works.

We will now look at the electric field vector of an electromagnetic wave travelling through our rotating half-waveplate. If we consider the case of a right circularly polarized wave propagating through a clockwise rotating half-waveplate, the electric field vector of the wave is

$$\begin{bmatrix} E_x \\ E_y \\ E_z \end{bmatrix} = \begin{bmatrix} E\cos(\omega_0 t) \\ E\sin(\omega_0 t) \\ 0 \end{bmatrix} \tag{4.16}$$

where ω_0 is the angular frequency of the wave. Since the field in the z direction is 0, we will ignore it from now on. When the wave is in the rotating waveplate, the principle axes of the polarization ellipse are x' and y'. We can rotate our reference frame by $-\theta$ to describe the electric field vector in this frame:

$$\begin{bmatrix} E_{x'} \\ E_{y'} \end{bmatrix}_{in} = \begin{bmatrix} \cos(\theta) & \sin(\theta) \\ -\sin(\theta) & \cos(\theta) \end{bmatrix} \begin{bmatrix} E\cos(\omega_0 t) \\ E\sin(\omega_0 t) \end{bmatrix} = \begin{bmatrix} E\cos(\omega_0 t - \theta) \\ E\sin(\omega_0 t - \theta) \end{bmatrix}. \tag{4.17}$$

If we choose our applied electric field E_0 such that $\Gamma = \pi$, the x' component is advanced by $\frac{\Gamma}{2}$ and the y' component is delayed by the same amount at the output of the rotating waveplate. In the rotating reference frame, the electric field vector of the photon is:

$$\begin{bmatrix} E_{x'} \\ E_{y'} \end{bmatrix}_{out} = \begin{bmatrix} E\cos(\omega_0 t - \theta + \frac{\Gamma}{2}) \\ E\sin(\omega_0 t - \theta - \frac{\Gamma}{2}) \end{bmatrix}. \tag{4.18}$$

Input Polarization	HWP Rotation	Output Frequency	Output Polarization
$\|L\rangle$	CW	$\omega_0 - \omega$	$\|R\rangle$
$\|L\rangle$	CCW	$\omega_0 + \omega$	$\|R\rangle$
$\|R\rangle$	CW	$\omega_0 + \omega$	$\|L\rangle$
$\|R\rangle$	CCW	$\omega_0 - \omega$	$\|L\rangle$

Table 4.2: A summary of the outputs of a rotating half-waveplate.

Rotating back to the stationary x and y axes, we find:

$$\begin{bmatrix} E_x \\ E_y \end{bmatrix}_{out} = \begin{bmatrix} \cos(\theta) & -\sin(\theta) \\ \sin(\theta) & \cos(\theta) \end{bmatrix} \begin{bmatrix} E\cos(\omega_0 t - \theta + \frac{\Gamma}{2}) \\ E\sin(\omega_0 t - \theta - \frac{\Gamma}{2}) \end{bmatrix} \tag{4.19}$$

$$= \begin{bmatrix} E\cos(\frac{\Gamma}{2})\cos(\omega_0 t) - E\sin(\frac{\Gamma}{2})\sin(\omega_0 t - 2\theta) \\ E\cos(\frac{\Gamma}{2})\sin(\omega_0 t) - E\sin(\frac{\Gamma}{2})\cos(\omega_0 t - 2\theta) \end{bmatrix}. \tag{4.20}$$

We now use the relationships $\theta = \frac{\omega t}{2}$ and $\Gamma = \pi$, which simplifies the electric field vector to:

$$\begin{bmatrix} E_x \\ E_y \end{bmatrix}_{out} = \begin{bmatrix} E\sin((\omega_0 - \omega)t) \\ E\cos((\omega_0 - \omega)t) \end{bmatrix}. \tag{4.21}$$

This is the electric field vector of a left circularly polarized wave of frequency $\omega_0 - \omega$. Thus, the effect of the rotating half-waveplate is shifting the frequency of the light down by ω and switching the handedness of the polarization. This analysis can be repeated for different combinations of polarization and waveplate rotation direction [104], with results being summarized in Table 4.2.

4.4 FSS Eraser

The fine structure splitting of a quantum dot introduces which-path information to the biexciton-exciton cascade. Single photon detectors with high timing jitter have low energy

uncertainty and can resolve the energy difference between the two paths of the cascade. While low timing jitter single photon detectors based on superconducting nanowires do exist, they are expensive and need to be cooled to cryogenic temperatures [105]. Here, we will discuss how our rotating waveplate frequency shifter can reduce or eliminate an arbitrary fine structure splitting from a quantum dot.

As explained in Chapter 2, the state produced by a quantum dot with fine structure splitting δ is:

$$|\Psi\rangle = \frac{|HH\rangle + e^{-i\frac{\delta}{\hbar}\tau}|VV\rangle}{\sqrt{2}}. \tag{4.22}$$

Following Fognini et al. [101], it is convenient to rewrite this state in the operator notation:

$$\Psi = \frac{1}{\sqrt{2}}\left[a^{\dagger}_{z,k_{XX}+\frac{\delta}{2\hbar c},H}a^{\dagger}_{z-\tau c,k_X-\frac{\delta}{2\hbar c},H} + a^{\dagger}_{z,k_{XX}-\frac{\delta}{2\hbar c},V}a^{\dagger}_{z-\tau c,k_X+\frac{\delta}{2\hbar c},V}\right]. \tag{4.23}$$

$a^{\dagger}$ is the creation operator, and corresponds to the creation of a photon with properties described by its subscript. Its adjoint a is the annihilation operator and corresponds to the destruction of a photon. The first subscript describes the spatial position of the photon, the second subscript describes the wavenumber, and the final subscript represents the polarization of the photon.

In order to shift the frequency of the emitted photons with the EOMs, the photons must be circularly polarized. Therefore, we use a pair of quarter-waveplates to transform from the $|H\rangle/|V\rangle$ basis to the $|R\rangle/\ |L\rangle$ basis. The waveplate in the exciton path is set with its fast axis at $\pi/4$ with respect to horizontal in the lab frame, and the waveplate in the biexciton path is set to $-\pi/4$. These waveplates are represented in operator form as

$$\begin{aligned}\Lambda_{1/4,XX} &= a^{\dagger}_{k_{XX},L}a_{k_{XX},V} + a^{\dagger}_{k_{XX},R}a_{k_{XX},H}\\ \Lambda_{1/4,X} &= a^{\dagger}_{k_X,R}a_{k_X,V} + a^{\dagger}_{k_X,L}a_{k_X,H}.\end{aligned} \tag{4.24}$$

After the QWPs, the two-photon state becomes:

$$\Phi = \frac{1}{\sqrt{2}}\left[a^{\dagger}_{z,k_{XX}+\frac{\delta}{2\hbar c},L}a^{\dagger}_{z-\tau c,k_X-\frac{\delta}{2\hbar c},R} + a^{\dagger}_{z,k_{XX}-\frac{\delta}{2\hbar c},R}a^{\dagger}_{z-\tau c,k_X+\frac{\delta}{2\hbar c},L}\right]. \tag{4.25}$$

Following our analysis in 4.3, a half-waveplate rotating counter-clockwise can be expressed in operator form as

$$\Lambda_{1/2}(\omega) = \sum_{k_i} a^{\dagger}_{k_i+2\omega/c,L}a_{k_i,R} + a^{\dagger}_{k_i-2\omega/c,R}a_{k_i,L}. \tag{4.26}$$

Therefore, after the EOMs, the two-photon state is:

$$\begin{aligned}
\chi &= \left[\Lambda_{1/2,XX}(\omega)\otimes\Lambda_{1/2,X}(\omega)\right]\Phi \\
&= \frac{1}{\sqrt{2}}\left[a^{\dagger}_{z,k_{XX}+\frac{\delta}{2\hbar c}-\frac{2\omega}{c},R}a^{\dagger}_{z-\tau c,k_X-\frac{\delta}{2\hbar c}+\frac{2\omega}{c},L} + a^{\dagger}_{z,k_{XX}-\frac{\delta}{2\hbar c}+\frac{2\omega}{c},L}a^{\dagger}_{z-\tau c,k_X+\frac{\delta}{2\hbar c}-\frac{2\omega}{c},R}\right] \\
&= \frac{1}{\sqrt{2}}\left[a^{\dagger}_{z,k_{XX},R}e^{i(z(\frac{\delta}{2\hbar c}-\frac{2\omega}{c}))}a^{\dagger}_{z,k_X,L}e^{i(-z(\frac{\delta}{2\hbar c}-\frac{2\omega}{c})-\tau ck_X+\tau c(\frac{\delta}{2\hbar c}-\frac{2\omega}{c}))}\right. \\
&\quad \left. + a^{\dagger}_{z,k_{XX},L}e^{i(-z(\frac{\delta}{2\hbar c}-\frac{2\omega}{c}))}a^{\dagger}_{z,k_X,R}e^{i(z(\frac{\delta}{2\hbar c}-\frac{2\omega}{c})-\tau ck_X-\tau c(\frac{\delta}{2\hbar c}-\frac{2\omega}{c}))}\right] \\
&= \frac{1}{\sqrt{2}}\left[a^{\dagger}_{z,k_{XX},R}a^{\dagger}_{z,k_X,L}e^{i\tau c(\frac{\delta}{2\hbar c}-\frac{2\omega}{c})} + a^{\dagger}_{z,k_{XX},L}a^{\dagger}_{z,k_X,R}e^{-i\tau c(\frac{\delta}{2\hbar c}-\frac{2\omega}{c})}\right]
\end{aligned} \tag{4.27}$$

Switching back to the ket notation:

$$\begin{aligned}
|\chi\rangle &= \frac{1}{\sqrt{2}}\left[|RL\rangle\, e^{i\tau c(\frac{\delta}{2\hbar c}-\frac{2\omega}{c})} + |LR\rangle\, e^{-i\tau c(\frac{\delta}{2\hbar c}-\frac{2\omega}{c})}\right] \\
&= \frac{|HH\rangle + |VV\rangle}{\sqrt{2}}\frac{e^{i\tau(2\omega-\frac{\delta}{2\hbar})} + e^{-i\tau(2\omega-\frac{\delta}{2\hbar})}}{2} - i\frac{|HV\rangle - |HV\rangle}{\sqrt{2}}\frac{e^{-i\tau(2\omega-\frac{\delta}{2\hbar})} - e^{i\tau(2\omega-\frac{\delta}{2\hbar})}}{2} \\
&= \frac{|HH\rangle + |VV\rangle}{\sqrt{2}}\cos\left(\left(2\omega-\frac{\delta}{2\hbar}\right)\tau\right) + \frac{|HV\rangle - |VH\rangle}{\sqrt{2}}\sin\left(\left(2\omega-\frac{\delta}{2\hbar}\right)\tau\right)
\end{aligned} \tag{4.28}$$

Therefore, if we set the angular frequency of the rotating waveplate to $\omega = \frac{\delta}{4\hbar}$, the output state will be $|\chi\rangle = \frac{|HH\rangle+|VV\rangle}{\sqrt{2}}$. This is exactly the state that would be emitted by a quantum dot with zero fine structure splitting. The net result of this process is recovering a maximally-entangled state that does not depend on the time between biexciton and exciton recombination. The entanglement of the emitted photons will therefore not be degraded, even when using single photon detectors with a large timing jitter.

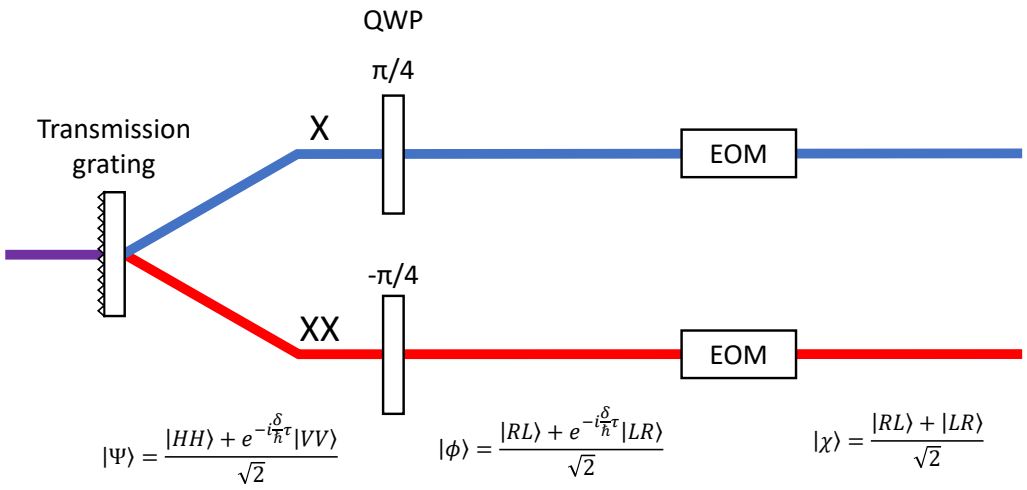

Figure 4.2: Diagram of the fine structure eraser using two EOM devices. The EOMs are set to rotate at a frequency $\omega = \frac{\delta}{2\hbar}$. The output state corresponds to that of a quantum dot without any fine structure splitting.

Additionally, Eq. 4.28 gives us a simple way to measure the FSS after the erasing process. While a full tomography experiment requires measuring the correlations in 36 bases, we can measure the FSS by only measuring in 4: HH, VV, HV and VH. The difference in HH+VV and HV+VH correlation counts will oscillate at a frequency $\frac{\delta}{\hbar} - 2\omega$, giving us a way to experimentally measure the fine structure splitting after the compensation process.

In order to implement the optical FSS eraser scheme, we need to demonstrate electro-optic frequency shifting experimentally. To do so, we require z-propagating lithium niobate and the ability to apply electric fields to it in the x and y directions. The next chapter presents frequency shifting results of a device based on the theory discussed in this chapter.

Chapter 5

Frequency Shifting

We will now move away from the theory of electro-optic modulation and show how it is implemented experimentally. From Chapter 4, we know we require the ability to apply a vertical and horizontal electric field to the region of $LiNbO_3$ that light is propagating in. Early work used a collimated beam propagating through a bulk $LiNbO_3$ crystal, which required applied voltages of up to 8 kV to achieve the half-wave condition [106]. This style of device was able to achieve a frequency shifting efficiency of up to 96% while operating at 110 MHz [107]. However, the large required voltages makes them unsuitable for operation at higher frequencies. These large voltages are required since the bulk optics setup necessitates a large electrode separation. In order to accommodate the incident beam, these bulk devices consisted of a bar of $LiNbO_3$ with widths of a few millimetres. Modern $LiNbO_3$ EOM devices instead use a waveguide to confine the light to a region near the electrodes. This reduces the beam diameter so that the electrodes can be placed close to the centre of the beam, typically only a few micrometers. This means that a significantly lower voltage can be applied to achieve the same electric field in the region the light is propagating. In this chapter, we will discuss how such a device is characterized and present results of frequency shifting light from a diode laser.

The results presented in this chapter follow from the work of Simon Daley [40] and Michael Kobierski [108]. Daley and Kobierski demonstrated a conversion efficiency of 92.6% to a single frequency sideband, using a device similar to the one described in this

section. However, the drive signal they used was found by optimizing for conversion efficiency, and could not be explained by theory. With this approach, it was found that high-efficiency conversion of one polarization in one direction did not imply conversion of the other polarization in the other direction, as is expected from a rotating half-waveplate. In order for these EOMs to be used in the FSS eraser scheme, they must be able to up-convert one polarization and down-convert the other with high efficiency and with the same drive signal. The goal of this chapter is to first determine theoretically what drive signal is required, and then to use a similar drive signal to up-convert and down-convert light with opposite handed polarization. This will confirm that the EOM is correctly acting as a rotating half-waveplate and can be used in the FSS eraser scheme.

5.1 Electro-Optic Modulator

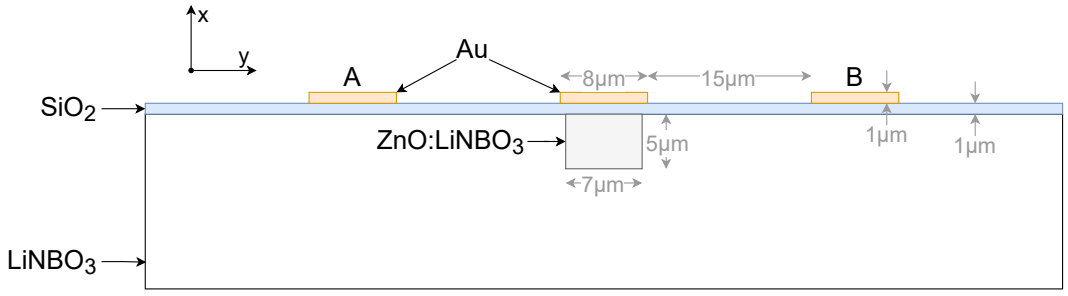

Figure 5.1: Cross-section of the $LiNbO_3$ EOM device.

For this project, we used a custom lithium niobate EOM manufactured by SRICO. The wafer consists of an x-cut, z-propagating $LiNbO_3$ crystal with a waveguide near one of the surfaces. The waveguide region is formed by zinc oxide diffusion, which forms waveguides with low polarization selectivity, low loss and a high photorefractive damage threshold [109]. Silicon dioxide is then deposited on the surface of the wafer to passivate it. On top of the SiO_2, three gold traces are deposited parallel to the waveguide, with the centre trace directly above the waveguide and the other two equidistant from the centre. The outer traces are used to apply voltages and the centre trace acts as a common ground. The $LiNbO_3$ wafer is 3 cm long, and a cross-section of the device is shown in Fig. 5.1.

As discussed in 4.2, our rotating waveplate protocol requires the ability to apply an electric field in the x and y directions. For our device, this is achieved by applying either a common or differential voltage to the two outer traces, while holding the middle trace at ground. Holding the outer traces at $+V_0$ and the centre trace at ground will create an electric field in the $+x$ direction within the waveguide. Holding trace A at $+V_0$ and trace B at $-V_0$ will create an electric field in the $+y$ direction. However, the magnitude of the electric field will not necessarily be the same in the common and differential cases, due to the geometry of the device.

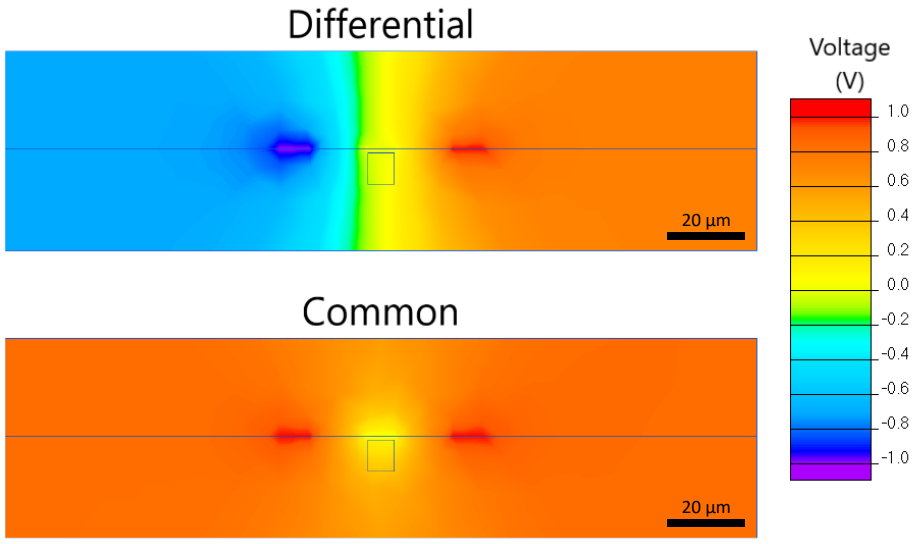

Figure 5.2: QuickField finite element method simulations of the electrostatic potential in the EOM for differential ($\pm$1V) and common (+1V) applied voltages. A differential voltage creates a horizontal electric field, whereas a common voltage creates a vertical one. The electric field in the waveguide region is 1.87 times larger in the common case compared to the differential case.

To quantify the difference in electric field magnitude for the common and differential cases, the electrostatic potential was solved using QuickField Student, a finite element analysis program. The device was modelled using the dimensions from Fig. 5.1, except for

the traces, which were modelled as infinitely thin. We then set the potentials of the two outside traces and solved for the electric field and potential using finite element analysis. Fig. 5.2 shows the simulated electrostatic potential in the air, chip and waveguide regions for differential and common voltages of equal magnitude ($\pm$1V). From this, we find E_x = 34.9 kV/m and E_y = 18.7 kV/m at the centre of the waveguide for the common and differential cases, respectively. For the same magnitude, common voltages produce an electric field 1.87 times larger in the waveguide region as compared to the differential case. We can compensate for this by choosing the phase ϕ between oscillating electric fields to be some value other than 90°. We instead select a phase such that, when the signals are applying a differential voltage, the magnitude of the voltage is 1.87 times larger than when the signals are applying a common voltage. This is satisfied for $\phi = 123.7°$, which yields an electric field of constant magnitude within the waveguide region. While the value of the phase may change depending on the exact geometry and properties of the device, it is good to know that the phase between the two signals will not be exactly 90° and can be changed when trying to find optimal experimental parameters.

5.1.1 Electronics

The electrical system for our EOM has a few requirements that guide our choice of components. First, we must be able to apply two sinusoidal signals of the same, tunable amplitude. This will allow us to set the signal amplitudes to the value determined by the half-wave voltage of the device. We must also be able to tune the phase between the two signals, as we just outlined. Additionally, we should be able to add DC voltages to both traces in order to compensate for any unwanted, built-in birefringence in the device. While the ZnO waveguide is expected to have minimal birefringence, any built-in birefringence can be tuned to zero by applying DC biases to both traces.

To generate a pair of sinusoidal waves, we use a TI DAC38RF82, a dual channel digital-to-analog converter capable of generating RF signals up to GHz frequencies. The amplitudes of the signals and the phase between them can all be controlled with custom Python code, which simplifies interfacing with the device [110]. The FSS of our dot is 760 MHz, and each EOM shifts one polarization up in frequency and the other down, so we need

to operate the EOMs at half of the frequency of the FSS. Therefore, want the ability to produce a drive signal at up to 380 MHz. At this frequency, the device is capable of generating signals with a measured amplitude of 0.76 dBm. Previous work with a similar $LiNbO_3$ EOM device required a drive signal of 30 dBm to achieve high-efficiency frequency shifting [111]. Therefore, the DAC38RF82 device itself does not generate a large enough amplitude signal to drive the device.

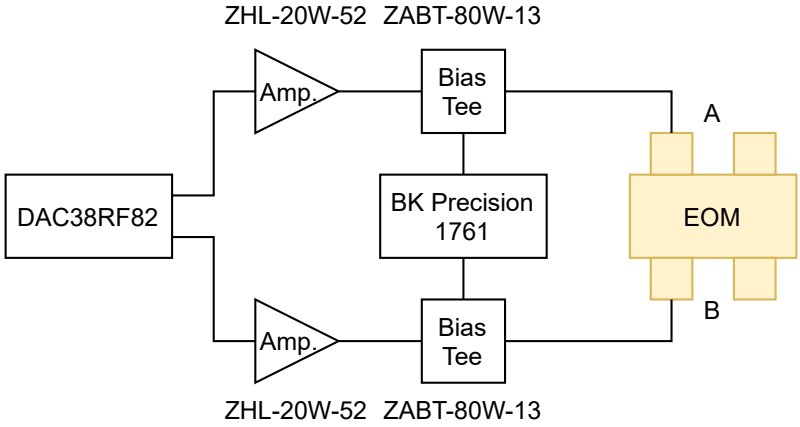

Figure 5.3: Electrical components involved in driving the EOM.

To amplify the voltage, the two RF signals are then sent through a pair of Mini-Circuits ZHL-20W-52 amplifiers. These high-power amplifiers have a gain of 50 dB, and a maximum output of 42 dBm. In order to avoid damaging the amplifiers, the output from the DAC38RF82 is first attenuated by -11 dB, restricting the maximum output to 39.76 dBm. For a 50 Ω system, 39.76 dBm corresponds to 61.5 V_{pp}. Since the phase between our signals is variable, so too will be the magnitude of the signals when they are equal, but opposite (i.e. what differential voltage they can apply). Two sinusoids with a phase difference of ϕ will have equal but opposite values at $x_i = \pi - \frac{\phi}{2}$, where the sinusoids will have a value of $\pm \sin\left(\pi - \frac{\phi}{2}\right)$. If we assume $\phi = 123.7°$ and an amplitude of $\frac{61.5}{2}$ V, this means the system is capable of applying up to 27.0 V of differential voltage.

Next, we want the ability to apply a constant DC bias to both traces A and B in order to remove any built-in birefringence from the EOM waveguide. To do so, we use a BK

Precision 1761 DC triple output power supply. The 1761 has two tunable voltage sources, which can be used to individually bias the two traces of the EOM. The DC component from the power supply is connected to the AC component through a ZABT-80W-13-S bias tee. The output of each bias tee is then connected to the EOM. A diagram of the electrical components is included in Fig. 5.3.

The final step is to send the electrical signal to the EOM. There are three different methods in which we can achieve this. They are the standing wave mode, which has two variations, and the travelling wave mode. These methods are shown in Fig. 5.4. Each method has benefits and drawbacks, which we will now discuss subsequently.

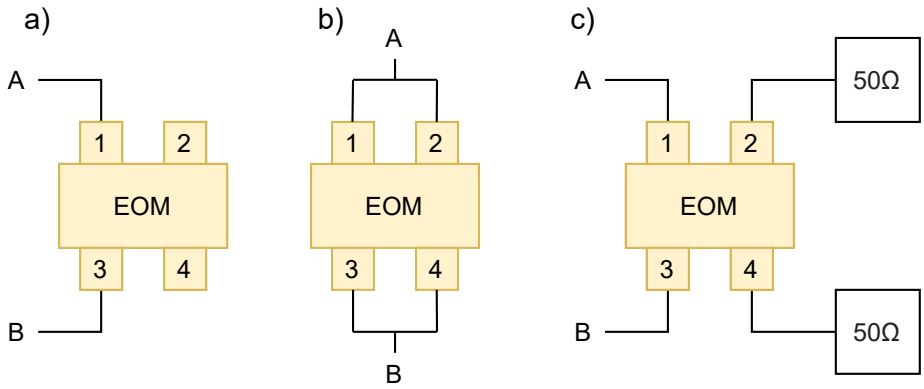

Figure 5.4: The three electrical configurations for the EOM device. a) The single-port standing wave configuration. b) The two-port standing wave configuration. c) The travelling wave configuration, in which the RF signal is terminated by a pair of 50 Ω resistors.

5.1.2 Standing Wave

The first EOM configuration is the standing wave mode. The idea of this setup is to have the EOM act as an open circuit, reflecting 100% of the signal back along the transmission line to form a standing wave. There are two ways to achieve this: first, connecting the transmission line directly to the input port of the EOM and leaving the output port disconnected (called the single-port method) or second, splitting the input transmission

line with a tee adaptor and connecting the outputs to the input and output ports of the EOM (called the two-port method).

The single-port method, shown in Fig. 5.4 a), places a voltage anti-node at the unattached port, near where the trace lies on the lithium niobate. A voltage anti-node corresponds to the maximum amplitude of voltage oscillation, and therefore minimizes the required power of the AC drive signal. Furthermore, a voltage anti-node corresponds to a current node, limiting the current flowing within the EOM device, which has destroyed a similar device through Joule heating [108]. The two-port method, shown in Fig. 5.4 b), has the ability to place a standing wave anti-node at the centre of the EOM trace, for the correct choice of transmission line lengths and driving frequency. However, this only works for drive signal frequencies with wavelengths that match the length of the transmission line after the splitter. This limits us to frequencies near a fundamental frequency determined by the transmission line lengths, and multiples thereof. Since we want the freedom to choose an arbitrary frequency, we will use the single-port method instead.

The standing wave mode is limited in the maximum frequency it can operate at. In the time that light is travelling through the EOM, it should only see the rotating half-waveplate at a single angle θ. However, in the standing wave mode, the voltage applied is approximately the same throughout the entire trace and oscillates at the frequency of the drive signal. As such, it will change throughout the transit time of the photons through the device. In order for the standing wave mode to work with high efficiency, we need the transit time of photons through the device $t_t = \frac{n_o l}{c}$ to be small relative to an oscillation period, or $1 \ll \frac{2\pi}{\omega t_t}$, where ω is the driving frequency. This condition also determines how closely the single-port method places a voltage anti-node at the centre of the EOM trace, which occurs for $l \ll \lambda$, or equivalently $1 \ll \frac{2\pi c}{\omega l n_o}$. Our lithium niobate chip is 3 cm long, so for our device at 380 MHz, we have:

$$\begin{aligned} 1 &\ll \frac{2\pi c}{\omega l n_o} \\ 1 &\ll 11.4. \end{aligned} \tag{5.1}$$

The inequality in Eq. 5.1 holds, but not entirely convincingly. We want the photon to see the waveplate at a single angle during its transit, but the angle of the waveplate will rotate

by 31.5° in the time it takes for a photon to transit the EOM in the current setup. We therefore expect to not be able to reach unity conversion efficiency in the standing wave mode. To counteract this, we can operate the EOM device at lower frequencies to increase the right-hand side of the inequality.

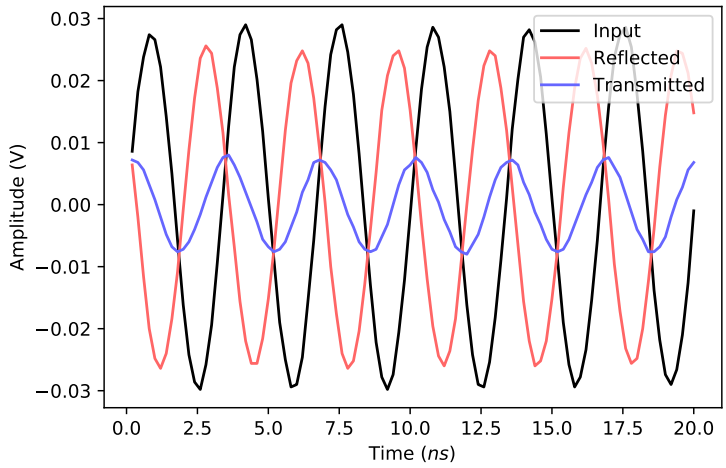

Figure 5.5: Measured reflected and transmitted signals for the EOM operating in standing wave mode, when only trace A is connected. 7.3% of the input power is transmitted through the EOM to trace B, due to capacitive coupling between the traces.

Another limiting factor in the performance of the EOM is the capacitive coupling between traces A and B. Ideally, the signals on the two traces are completely independent of each other, but capacitive coupling leads to transmission between the traces. When a single trace (either A or B) was driven, a portion of the signal was transmitted to the other trace, rather than entirely reflected back along the input transmission line. To see this, a pair of Mini-Circuits ZGBDC20-33H-S+ bi-direction couplers were placed before the EOM on both paths. Bi-directional couplers are four-port devices, which couple a small fraction of the signal on a transmission line to different ports, depending on the direction of propagation of the signal. This allows us to see the forward and backward propagating components on the transmission lines, and therefore determine how much of the signal is reflected or transmitted at the EOM. Fig. 5.5 shows the reflected and transmitted signal

when only channel A was driven at 300 MHz in the single-port standing wave configuration. The signals were recorded with a Textronix MDO4104-6 oscilloscope, which was used for all subsequent experiments as well. It was determined that 77.5% of the input power was reflected and 7.3% was transmitted through the EOM to channel B. This process was repeated with only trace B driven and similar results were obtained: 74.5% reflection and 6.1% transmission. This transmission is attributed to capacitive coupling between the two traces of the EOM. Since the parallel traces are separated by only a few micrometers, there is a non-negligible capacitance between the traces, so a portion of the signal is transmitted across the EOM.

The capacitive coupling between the traces means that the signal applied to each transmission line is not what will be seen on each EOM trace. Instead, it will be a combination of the input signal on the trace and the transmitted portion of the signal from the other trace. This can always be compensated for by individually setting the amplitude of the signal on traces A and B such that the incident, reflected and transmitted signals sum to be equal on both traces. Another solution would be putting an inductor across traces A and B, such that the signal sees an infinite impedance across the traces from the capacitance and inductor at the drive frequency. This would solve the coupling problem and make the two traces isolated as intended.

5.1.3 Travelling Wave

The second EOM electrical configuration is the travelling wave mode, shown in Fig. 5.4 c). In this setup, the input transmission line is connected to the input port of the EOM, and the electrical signal travels along the traces of the EOM before being terminated at the output port. This setup eliminates reflections by terminating the signal with a 50 Ω resistor after the EOM. The travelling wave setup addresses the issue of the emulated waveplate rotating during the transit of the photon, so we are no longer limited by Eq. 5.1. In this setup, the photons and electrical signal co-propagate, so the problem of a photon seeing a changing electric field is reduced. Note that in general, the velocity of the electrical signal and the speed of light in the material will not be the same, but it will be an improvement over the standing wave method. With this setup, frequency up and down conversion by 2

GHz has been demonstrated on a laser with efficiencies of over 90% [111].

In contrast to the standing wave method, the travelling wave mode does not place a voltage anti-node at the location of the EOM, meaning there will be current flowing in the traces of the EOM. This causes Joule heating on the EOM traces, which can raise the temperature high enough to damage the waveguide by allowing the ZnO to diffuse deeper into the $LiNbO_3$ [40]. Unfortunately, the gold traces on our current devices are very thin (1 μm) and heating is a significant problem. As a result, our current devices are not capable of operating in the travelling wave mode. However, the next generation of devices will have traces 10 μm thick and will be able to operate in the travelling wave mode.

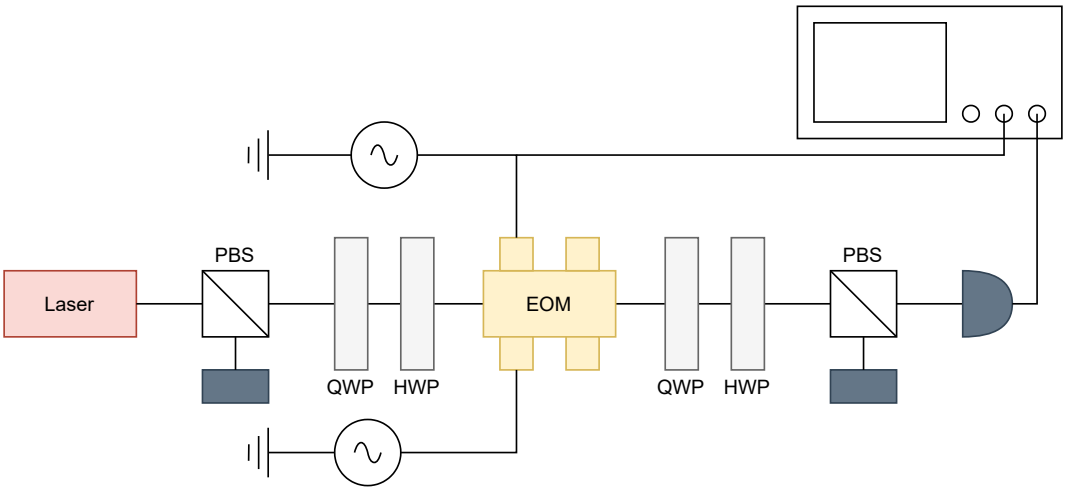

Figure 5.6: EOM setup for DC testing. In this setup, the voltage sources apply a slow-changing triangle wave voltage to the EOM traces, 180° out of phase with each other.

5.2 DC Results

Before attempting to shift the frequency of light with an AC drive signal, we must find some device parameters using DC voltages. Of particular interest are two values: the half-wave voltage and the built-in birefringence of the device. The half-wave voltage is the voltage we must apply to delay one component of the electric field by one half-wavelength. This

is the voltage required to emulate a stationary half-waveplate, and will tell us what the amplitude of the AC drive signal should be. The built-in birefringence is the birefringence of the device with no voltage applied to either of the traces. It is possible that the waveguide has different indices of refraction along different axes, leading to an intrinsic birefringence even with no signal on either trace. Both of these values can be found by applying a slow-oscillating voltage to both traces and measuring the effect on the polarization of incident photons.

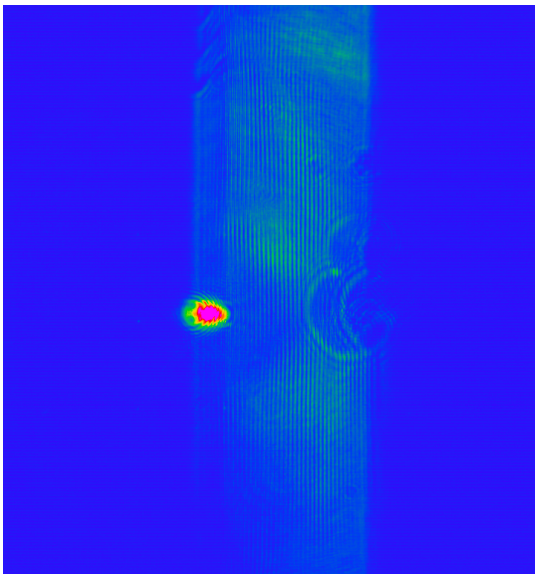

Figure 5.7: False colour image of the waveguide and $LiNbO_3$ chip, as imaged with a Thorlabs DCC1545M-GL CMOS camera. The bright spot is laser light travelling through the EOM waveguide. The faint rectangular region is the bulk $LiNbO_3$ chip.

The following experiments were all done with light from a Thorlabs DBR852P diode laser. This laser has a spectral linewidth of 10 MHz, so we can easily resolve a frequency shift on the order of hundreds of MHz. In addition, the wavelength of the laser is 852 nm, which is not far off from the 892 nm of the exciton photon from the quantum dot. According to Eq. 4.15, the electric field required to emulate a half waveplate scales linearly with wavelength. Therefore, changing the operating wavelength from 852 nm to 892 nm will require increasing the amplitude of the drive signal by only 4.7%. Light from the laser

was coupled into the waveguide with an Olympus LMPLN5XIR objective lens, chosen for its numerical aperture of 0.1 and high transmission in the near-IR. At the output of the EOM, the beam passes through a Thorlabs BP108 pellicle beamsplitter and approximately 8% of the intensity is sent to a Thorlabs DCC1545M-GL CMOS camera, to confirm that the light is propagating in the waveguide region. The optical output of the $LiNbO_3$ chip is shown in Fig. 5.7, which shows that the majority of the light is confined to the waveguide region.

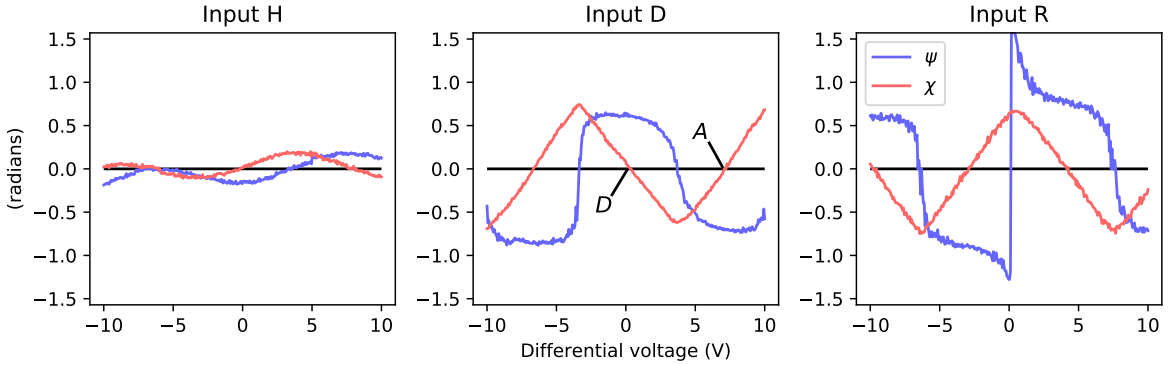

Figure 5.8: Ellipticity angle χ and orientation angle ψ of light output from the EOM as a function of the applied differential voltage for three input polarizations. For H polarized input light, the polarization barely changes, since the polarization is aligned with the principle axes of the EOM waveplate. For D polarized light, the light is not aligned with the principle axes, and we see modulation of the polarization. For an applied voltage of around ± 7 V, we see complete conversion from D to A polarized light. For R polarized input, we also see modulation of the polarization, with conversion from R to L also around $\pm$ 7 V, as expected.

To find both the built-in birefringence and the half-wave voltage, we apply a slow-oscillating differential voltage to the EOM traces and measure the output polarization. The setup for this experiment is shown in Fig. 5.6. After the EOM are a Casix WPA1215-$\lambda/4$ QWP followed by a Casix WPA1215-$\lambda/2$ HWP and a Thorlabs LPNIRE100-B polarizer, which are used to measure the output polarization in six bases $\{H, V, D, A, R, L\}$ and reconstruct the output polarization of the beam for a given input polarization. After

reconstructing the output polarization, we can calculate the two values of the polarization ellipse: the ellipticity angle χ and the orientation angle ψ. Fig. 5.8 shows the calculated values of ψ and χ when a differential voltage is applied to traces A and B. The experiment was repeated three times, once each with H, D and R polarized light as the input.

From Fig. 5.8, we can make a few observations. First, the waveguide has minimal built-in birefringence. This is seen in all three plots; the output polarization at zero applied voltage always corresponds closely to the input polarization. For example, in the Input R plot, the discontinuity in ψ at 0 V corresponds to completely circularly polarized light, for which the orientation angle ψ is undefined. Additionally, the lack of large changes in the output polarization for any voltages in the Input H plot tells us that the angle of the waveplate created in the $LiNbO_3$ aligns closely with the H polarization. This makes sense, as a differential voltage creates an electric field in the y direction, which causes the waveplate fast and slow axes to lie along the x and y axes, respectively. Since, for H polarized light, the electric field is entirely in the y direction, no relative shift between electric field components is created, so the output polarization should be unaffected. This reasoning is confirmed by the Input D plot, which shows complete conversion of D to A polarized light around 7 V. At zero volts, the ellipticity angle χ is zero since D is a form of linear polarization, and the orientation angle ψ is close to $\frac{\pi}{4}$, as expected for diagonally-polarized light. At 7 volts, the ellipticity is once again zero, and the orientation angle is now close to $-\frac{\pi}{4}$, indicating that the light is now anti-diagonally-polarized. Since D polarized light has equal electric field components in the x and y directions, a delay in one of these directions will cause a change in the output polarization. Going from D to A requires a half-wave delay, so this plot also tells us our half-wave voltage: 7 V.

5.3 AC Results

With our device characterized, we can now move on to testing its frequency shifting capabilities using the narrowband laser. The new experimental setup (shown in Fig. 5.9) was adjusted to accommodate a Thorlabs SA200-8B scanning Fabry-Perot cavity. One end of the cavity is connected to a piezoelectric transducer, which changes the cavity length

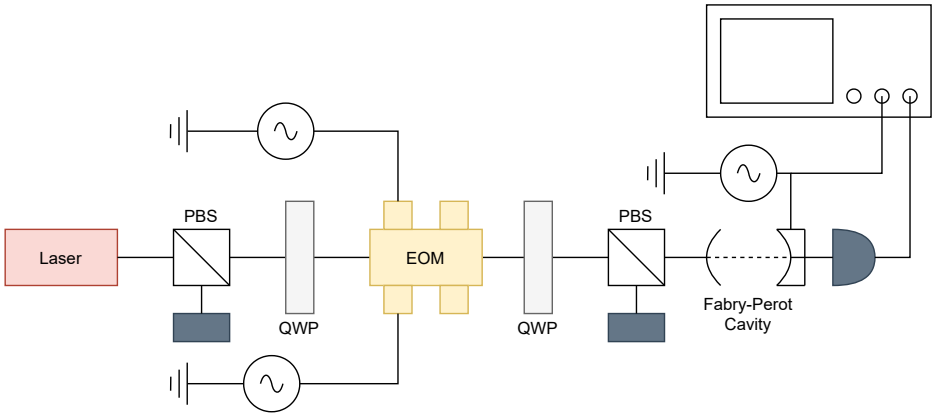

Figure 5.9: EOM setup for AC experiment. In this experiment, the voltage sources connected to the EOM are the RF signals from the amplifiers. The voltage source connected to the Fabry-Perot is a slow-oscillating voltage used to scan the transmission frequency of the cavity.

when a voltage is applied. Changing the length of the cavity changes the wavelength of transmitted modes, and the output intensity is detected using a photodiode. The cavity has a free spectral range (FSR) of 1.5 GHz and a resolution of 7.5 MHz. From the FSR, we can find the conversion between the voltage applied and transmitted wavelength, allowing us to measure the shift in frequency of the laser light.

In order to confirm that the EOM rotating waveplate emulator is working correctly, we need to demonstrate both down-shifting of RCP light and up-shifting of LCP light. We need to be able to achieve both up-shifting and down-shifting with the same drive signal in order to use the EOM devices for the FSS eraser discussed in the previous chapter. It has previously been demonstrated that electro-optic half-waveplate emulators are capable of both up-converting and down-converting light [111, 112], although it is unclear if the same drive signal was used to shift in both directions. The EOM needs to be able to achieve both of these simultaneously, and with high efficiency. In addition, the device needs to act as a half-waveplate, so that we get RCP light out for LCP light in and LCP light out for RCP light in.

In rotating half-waveplate EOMs, inefficiencies correspond to light not being shifted,

or being shifted by the wrong amount [107]. These devices are capable of shifting photons by integer multiples of the drive frequency, forming sidebands. This means that if we want to increase the frequency by ω, we may get components shifted by {..., -2ω, $-\omega$, 0, ω, 2ω, ...}. For a perfect drive signal, all the optical power will be shifted into the $+\omega$ sideband, but errors such as amplitude imbalance, phase imbalance and higher harmonics will lead to some optical power in other sidebands. The goal, therefore, is to optimize the drive signal to get as much power in the desired sideband as possible.

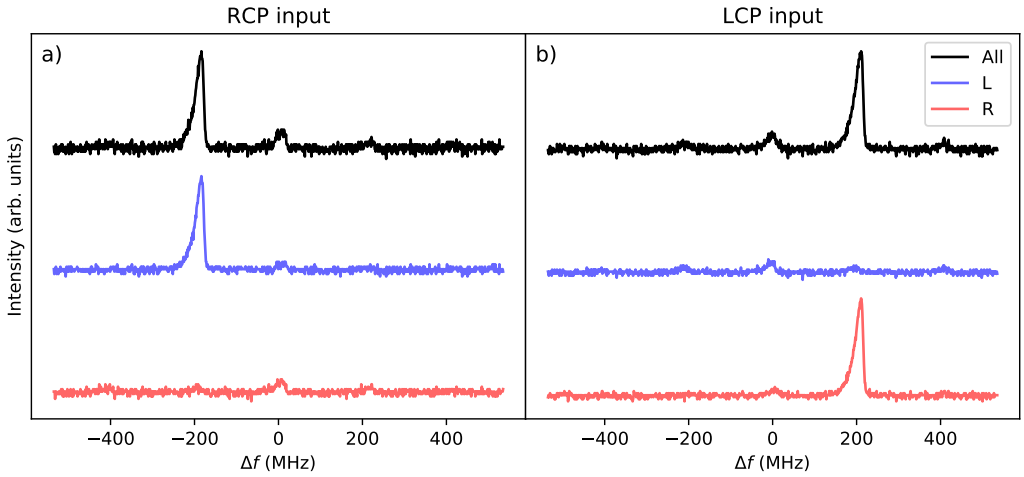

Figure 5.10: Frequency shifting of light from a narrowband diode laser. The blue line is the measured intensity of left circularly polarized light, and the red line is the intensity of right circularly polarized light. The black line is the sum of the intensities in the two polarization modes. a) Frequency down-conversion of RCP light through the rotating half-waveplate. Integrating the peaks shows that 83.7% of optical power is converted to the correct frequency and polarization band. b) Frequency up-conversion of LCP light with an efficiency of 80.7%. All data was collected with the same drive signal applied to the EOM.

We have five experimental parameters that we can adjust to find an optimal combination for frequency shifting: frequency (f), amplitude (V_{AC}), phase (ϕ) and DC bias on traces A and B (V_A and V_B). For frequency, we want the ability to go up to 380 MHz, but since our device is expected to perform worse for higher frequencies, we chose to operate at $f = 200$ MHz. The phase was set to 123° and both V_A and V_B were initially set to 0 V.

For amplitude, we need 7 V of differential voltage to emulate a half-waveplate. For two sinusoids 123° out of phase, this is achieved by a signal amplitude of 7.97 V, or 15.9 V_{pp}. Since our system is capable of generating signals up to 61.5 V_{pp} (39.7 dBm), we start by driving it at 15.9/61.5 = 25.8% power. With these values, there was a noticeable amount of light shifted into the desired sideband, but the majority of the intensity was still in the main band. This is characteristic of too small an amplitude in the drive signal [107]. Therefore, the amplitude of the drive signal was increased until an improvement in the conversion efficiency was observed.

After some optimization of the drive variables, a high degree of frequency shifting was achieved. The values were: $f = 200$ MHz, $V_{AC} = 40.6$ V_{pp} (36.1 dBm), $\phi = 120°$, $V_B = 0$ V and $V_A - 6.56$ V. With these parameters, frequency shifting both up and down were observed, depending on the handedness of the input polarization. Many trials were performed, and the best results are shown in Fig. 5.10. Integrating the peaks shows that, for right circularly polarized input, 83.7% of the light is shifted down in frequency and is left circularly polarized. For left circularly polarized input, 80.7% of photons are up-shifted and right circularly polarized after the EOM. This shows that the EOM is working as intended by emulating a fast rotating half-waveplate. The inability to reach unity conversion efficiency can be attributed to the inherent errors introduced by the standing wave setup, and possibly errors in the drive signal parameters as well.

The experimental parameters required to emulate a fast rotating half-waveplate mostly agreed with our theoretical analysis of the system. The phase between the two drive signals was only 3.7° off from the predicted value, indicating excellent agreement with our model. Additionally, the DC bias on trace B was 0 V, as predicted. The DC bias on trace A was predicted to also be 0 V, but was found to be optimal at -6.56 V. However, this voltage is relatively low compared to previous trials [40, 108], indicating better agreement with theory. The signal amplitude disagreed most strongly with the predicted amplitude, as we needed an amplitude of 40.6 V_{pp}, which is 2.55 times larger than the predicted 15.9 V_{pp}. While we did expect around 50% of the power to be reflected by the EOM [108], this does not fully explain the difference. The discrepancy may also be partially explained by loss in the system at higher powers, although further testing is needed to confirm if this is the case.

5.3.1 Stability

In order to use our EOM in more interesting experiments, like the FSS eraser described in Section 4.4, it needs to be stable over long periods of time. The frequency shifting data in Fig. 5.10 was taken in approximately 100 ms, whereas the tomography experiment discussed in Chapter 2 consists of data taken over a 6.5-hour period. Even a partial tomography experiment to measure the FSS would take nearly 45 minutes, so we are interested in determining if our EOM is stable on these time scales.

In previous trials with these EOM devices, it was observed that the conversion efficiency tends to decrease the longer the devices are run. This could be compensated for by gradually increasing the DC biases applied to the two traces as the efficiency dropped. From this observation, we hypothesized that the DC bias causes charges to drift within the $LiNbO_3$ and generate an internal electric field opposing the applied field. To test this, and understand the timescale on which this occurs, we ran the EOM device for an extended period of time and measured the conversion efficiency throughout.

Fig. 5.11 shows the amount of power in four frequency bands over a period of 40 minutes. For the first 20 minutes, both the AC and DC signals were left on, and the conversion efficiency was measured twice every minute. In minutes 20 to 30, the DC voltage was turned off, except briefly for data acquisition once every minute. In minutes 30 to 40, the AC signal was also turned off, except for data acquisition. At each time step, the intensity vs. frequency of the optical output was recorded by the oscilloscope, giving data like that in Fig. 5.10. For each data acquisition, the four frequency bands with the highest intensity were identified, and the shifting efficiency was calculated from the relative heights of the peaks.

In the 20 minutes with the full electrical signal applied, the conversion efficiency gradually decreased from around 80% to 60%. This led to an increase in the power in the unshifted energy band. However, in the following 10 minutes without DC voltage, the conversion efficiency recovered and increased to approximately 70%. In the 10 minutes following that, the DC and AC signals were turned off except for data acquisition, and the conversion efficiency recovered to approximately the initial 80%.

Turning the AC signal off appears to have no additional benefit compared to turning off

just the DC signal. This supports our hypothesis that the DC voltage is the cause of the decreasing conversion efficiency. The likely reason for this is charge accumulation within the $LiNbO_3$, which opposes the applied DC electric field. Since $LiNbO_3$ is a dielectric, it can be polarized by an external electric field, producing an internal field that opposes the applied one. A constant electric field leads to a gradual buildup of charge which opposes the applied field and thus decreases the conversion efficiency. However, the AC field is oscillating quickly and does not cause charge buildup in the dielectric, so the efficiency will not decrease if the AC signal is left on. When the DC bias was turned off, the conversion efficiency appeared to recover approximately as quickly as it had deteriorated, attributed to the charges relaxing and no longer opposing the applied field [113]. It still remains to be shown that this method of duty cycling the EOM can lead to stable operation over extended periods.

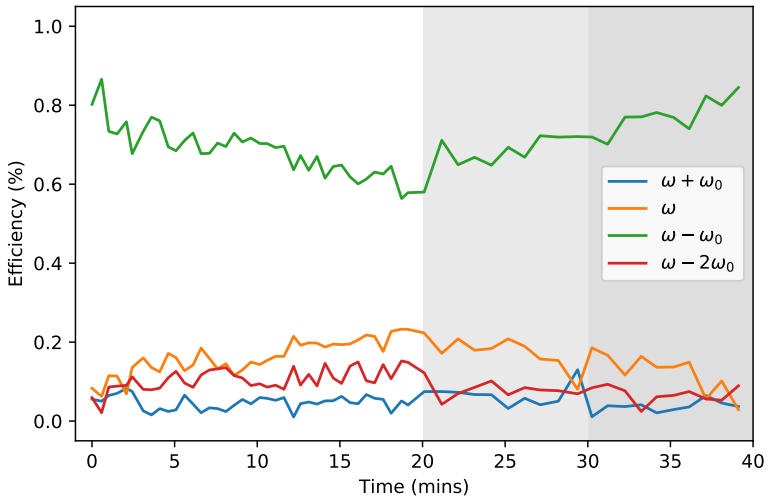

Figure 5.11: Conversion efficiency of the EOM device over time. In the light grey region, the DC voltage was turned off and only turned on to take measurements. In the dark grey region, the AC signal was turned off as well. In the first 20 minutes, the efficiency decays from around 80% to 60%. The conversion efficiency recovers over a similar time span when the DC voltage is turned off.

These results are relevant to the feasibility of using these EOM devices in experiments

that use our quantum dot source. We note that the conversion efficiency is only stable on short time scales, up to about a minute. This is not ideal for experiments such as quantum state tomography, which requires hours of data acquisition for a full experiment. However, the fact that the conversion efficiency recovers on a similar timescale that it deteriorates is reassuring. Experiments requiring long-term, stable operation of these $LiNbO_3$ EOMs will likely require cycling the devices on and off to prevent charge buildup and a loss in efficiency. In the simplest case, this may be possible by running the EOMs at a duty cycle with enough off time to allow for charge relaxation. If stable operation cannot be achieved through a simple duty cycle, the EOMs may require an active feedback system to control when the DC bias is applied. The active feedback system would sample the output from the EOM and disable the DC bias or apply a reverse bias to facilitate charge relaxation when the efficiency drops below an acceptable level. Such a system may be necessary to maintain high conversion efficiency over long periods of time.

Chapter 6

Conclusion and Outlook

6.1 Conclusion

Semiconductor quantum dots have the ability to outperform the current state-of-the-art SPDC-based photon pair sources. However, there are still a number of issues that need to be solved before this happens, including long lifetimes and the fine structure splitting. In this thesis, we have shown that resonant two-photon excitation improves the single photon purity and measured concurrence of emitted photon pairs. However, the performance of quantum dot-based sources is still limited by their fine structure splitting, which is an unwanted property caused by asymmetry in the quantum dot confining potential. It is of interest to tune the quantum dot fine structure splitting to zero, for which many schemes have already been demonstrated experimentally.

In this thesis, we discussed an all-optical approach to eliminating the FSS using an electro-optic rotating half-waveplate emulator. We showed theoretically that such a device could be used to reduce or eliminate an arbitrary fine structure splitting in photons emitted by a quantum dot. Importantly, this scheme is agnostic to the specific implementation of the source, as well as the nanostructure it is embedded in. Furthermore, multiple all-optical FSS erasers could be used to eliminate the FSS of multiple sources on the same sample, something that is impossible with many of the other FSS removal schemes.

This thesis leaves us in a good position to demonstrate the optical FSS eraser experimentally. The average frequency shifting efficiency shown here was 82.2%, with similar rates for up and down-conversion. Since the FSS eraser scheme depends on two EOMs, the overall erasing efficiency would be $\epsilon = 0.822^2 = 0.676$. At this rate, the FSS erasing capability would likely be measurable, as the signal-to-noise ratio (ignoring other sources of noise) would be $\frac{0.676}{1-0.676} = 2.09$. In Chapter 4, we discussed how a partial tomography measurement in only four polarization bases could be used to measure a reduction in the FSS. To do such an experiment, the EOM would need to be capable of stable operation for approximately 40 minutes. The results in this thesis indicate that the stability drops significantly over the span of 20 minutes, but can recover when the DC signal is turned off. In order to reach the stability required for long, automated experiments like quantum state tomography, the EOMs might require duty cycling or an active feedback system to control the signal applied to the traces.

In order to fully recover a pure, time-independent state corresponding to a quantum dot without any fine structure splitting, we would need unity frequency conversion efficiency. The efficiency of the EOMs may be improved in the future by moving to the travelling wave method and optimizing both signal amplitudes individually to account for capacitive coupling between the EOM traces. By implementing both of these, it may be possible to improve the efficiency of the rotating waveplate emulator even further, getting closer to an all-optical method of removing the quantum dot fine structure splitting with high efficiency.

6.2 Outlook

There exist natural next steps for both the resonant excitation and optical FSS eraser experiments, that will build on the research in this thesis. For resonant two photon excitation, the next step is repeating the tomography experiment performed in this thesis with low timing jitter photon detectors. With low timing jitter, detectors are unable to resolve the energy difference between the two branches of the biexciton-exciton cascade. Because of this, it is predicted that low timing jitter detectors will measure near-unity

concurrence over the entire lifetime of the excited state. Superconducting nanowire single photon detectors (SNSPDs) have demonstrated with a timing jitter of less than 3 ps [114] and sub-15 ps timing jitter SNSPDs are commercially available [115]. Future experiments can use these low jitter detectors in combination with resonant TPE to attempt to measure near-unity concurrence over the lifetime of the exciton.

For the FSS eraser experiment, the work in this thesis has demonstrated that the EOM devices are capable of emulating a fast rotating half-waveplate and converting the frequency of photons with high efficiency. The immediate next step is addressing the stability of the devices, either with a simple duty cycle or an active feedback system. Once stable operation is demonstrated, the next step will be using the EOMs in a simplified version of the tomography experiment, to determine if they are capable of reducing the FSS. While a full tomography experiment involves measurement in a set of 36 polarization bases, we are able to determine the FSS using a small subset of these measurements. The oscillations between the RL+LR and RR+LL correlation counts are used to determine the frequency of the precession caused by the FSS. Since the photons must travel through quarter waveplates in the FSS eraser scheme, the oscillations in the HH+VV and HV+VH correlation counts will contain information about the FSS at the output of the EOMs. For EOMs operating at unity efficiency at the frequency corresponding to the FSS, no oscillations will be present in the HH+VV-(HV+VH) correlation counts. This provides a simple method of determining whether the FSS eraser scheme has succeeded, without requiring a full tomography experiment.

Both of these subsequent experiments, if successful, will help overcome different obstacles currently faced by quantum dots. The resonant TPE tomography experiment has the ability to show that dephasing is not a significant issue faced by quantum dots, and that the two-photon entanglement is not degraded in the presence of a fine structure splitting. The FSS eraser experiment may demonstrate that an all-optical method of erasing the fine structure splitting is possible by acting on the photons after they have been emitted, rather than modifying the environment of the source itself. Both of these will help push quantum dot photon sources forward, with the goal of surpassing SPDC-based sources to become the state-of-the-art entangled photon sources.

References

[1] G. Wendin, "Quantum information processing with superconducting circuits: a review," *Reports on Progress in Physics*, vol. 80, no. 10, p. 106001, 2017.

[2] C. D. Bruzewicz, J. Chiaverini, R. Mcconnell, and J. M. Sage, "Trapped-ion quantum computing: Progress and challenges," *Applied Physics Reviews*, vol. 6, no. 2, p. 021314, 2019.

[3] G.-Q. Liu and X.-Y. Pan, "Quantum information processing with nitrogen–vacancy centers in diamond," *Chinese Physics B*, vol. 27, no. 2, p. 020304, 2018.

[4] C. Ramanathan, N. Boulant, Z. Chen, D. G. Cory, I. Chuang, and M. Steffen, "NMR quantum information processing," *Quantum Information Processing*, vol. 3, no. 1, p. 15–44, 2004.

[5] C. Schimpf, M. Reindl, F. B. Basset, K. D. Jöns, R. Trotta, and A. Rastelli, "Quantum dots as potential sources of strongly entangled photons: Perspectives and challenges for applications in quantum networks," *Applied Physics Letters*, vol. 118, no. 10, p. 100502, 2021.

[6] R. Winik, D. Cogan, Y. Don, I. Schwartz, L. Gantz, E. R. Schmidgall, N. Livneh, R. Rapaport, E. Buks, D. Gershoni, and et al., "On-demand source of maximally entangled photon pairs using the biexciton-exciton radiative cascade," *Physical Review B*, vol. 95, no. 23, p. 235435, 2017.

[7] L. Leandro, J. Hastrup, R. Reznik, G. Cirlin, and N. Akopian, "Resonant excitation of nanowire quantum dots," *npj Quantum Information*, vol. 6, no. 1, p. 93, 2020.

[8] C. Hopfmann, W. Nie, N. L. Sharma, C. Weigelt, F. Ding, and O. G. Schmidt, "Maximally entangled and gigahertz-clocked on-demand photon pair source," *Physical Review B*, vol. 103, no. 7, p. 075413, 2021.

[9] Y. Chen, M. Zopf, R. Keil, F. Ding, and O. G. Schmidt, "Highly-efficient extraction of entangled photons from quantum dots using a broadband optical antenna," *Nature Communications*, vol. 9, no. 1, p. 2994, 2018.

[10] E. Knill, R. Laflamme, and G. J. Milburn, "A scheme for efficient quantum computation with linear optics," *Nature*, vol. 409, no. 6816, p. 46–52, 2001.

[11] J. M. Lukens and P. Lougovski, "Frequency-encoded photonic qubits for scalable quantum information processing," *Optica*, vol. 4, no. 1, pp. 8–16, 2016.

[12] T. Huber, A. Predojević, M. Khoshnegar, D. Dalacu, P. J. Poole, H. Majedi, and G. Weihs, "Polarization entangled photons from quantum dots embedded in nanowires," *Nano Letters*, vol. 14, no. 12, p. 7107–7114, 2014.

[13] I. Marcikic, H. D. Riedmatten, W. Tittel, V. Scarani, H. Zbinden, and N. Gisin, "Time-bin entangled qubits for quantum communication created by femtosecond pulses," *Physical Review A*, vol. 66, no. 6, p. 062308, 2002.

[14] J. T. Barreiro, T.-C. Wei, and P. G. Kwiat, "Beating the channel capacity limit for linear photonic superdense coding," *Nature Physics*, vol. 4, no. 4, p. 282–286, 2008.

[15] D. Bouwmeester, J.-W. Pan, K. Mattle, M. Eibl, H. Weinfurter, and A. Zeilinger, "Experimental quantum teleportation," *Nature*, vol. 390, no. 6660, p. 575–579, 1997.

[16] D. F. V. James, P. G. Kwiat, W. J. Munro, and A. G. White, "Measurement of qubits," *Physical Review A*, vol. 64, no. 5, p. 052312, 2001.

[17] W. K. Wootters, "Entanglement of formation of an arbitrary state of two qubits," *Physical Review Letters*, vol. 80, no. 10, p. 2245–2248, 1998.

[18] W. An-Min, "A simplified and obvious expression of concurrence in Wootters' measure of entanglement of a pair of qubits," *Chinese Physics Letters*, vol. 20, no. 11, p. 1907–1909, 2003.

[19] W. K. Wootters, "Entanglement of formation and concurrence," *Quantum Information and Computation*, vol. 1, no. 1, p. 27–44, 2001.

[20] F. Verstraete and H. Verschelde, "Fidelity of mixed states of two qubits," *Physical Review A*, vol. 66, no. 2, 2002.

[21] J.-W. Pan, D. Bouwmeester, H. Weinfurter, and A. Zeilinger, "Experimental entanglement swapping: Entangling photons that never interacted," *Physical Review Letters*, vol. 80, no. 18, p. 3891–3894, 1998.

[22] F. B. Basset, M. B. Rota, C. Schimpf, D. Tedeschi, K. D. Zeuner, S. F. C. D. Silva, M. Reindl, V. Zwiller, K. D. Jöns, A. Rastelli, and R. Trotta, "Entanglement swapping with photons generated on demand by a quantum dot," *Physical Review Letters*, vol. 123, no. 16, p. 160501, 2019.

[23] W. K. Wootters and W. H. Zurek, "A single quantum cannot be cloned," *Nature*, vol. 299, no. 5886, p. 802–803, 1982.

[24] T. Inagaki, N. Matsuda, O. Tadanaga, M. Asobe, and H. Takesue, "Entanglement distribution over 300 km of fiber," *Optics Express*, vol. 21, no. 20, pp. 23241–23249, 2013.

[25] R. Ursin, F. Tiefenbacher, T. Schmitt-Manderbach, H. Weier, T. Scheidl, M. Lindenthal, B. Blauensteiner, T. Jennewein, J. Perdigues, P. Trojek, B. Ömer, M. Fürst, M. Meyenburg, J. Rarity, Z. Sodnik, C. Barbieri, H. Weinfurter, and A. Zeilinger, "Entanglement-based quantum communication over 144 km," *Nature Physics*, vol. 3, no. 7, p. 481–486, 2007.

[26] N. Sangouard, C. Simon, H. D. Riedmatten, and N. Gisin, "Quantum repeaters based on atomic ensembles and linear optics," *Reviews of Modern Physics*, vol. 83, no. 1, p. 33–80, 2011.

[27] F. Rozpedek, R. Yehia, K. Goodenough, M. Ruf, P. C. Humphreys, R. Hanson, S. Wehner, and D. Elkouss, "Near-term quantum-repeater experiments with nitrogen-vacancy centers: Overcoming the limitations of direct transmission," *Physical Review A*, vol. 99, no. 5, p. 052330, 2019.

[28] F. B. Basset, M. Valeri, E. Roccia, V. Muredda, D. Poderini, J. Neuwirth, N. Spagnolo, M. B. Rota, G. Carvacho, F. Sciarrino, and R. Trotta, "Quantum key distribution with entangled photons generated on demand by a quantum dot," *Science Advances*, vol. 7, no. 12, 2021.

[29] P. Grünwald, "Effective second-order correlation function and single-photon detection," *New Journal of Physics*, vol. 21, no. 9, p. 093003, 2019.

[30] R. Hanbury-Brown and R. Q. Twiss, "Correlation between photons in two coherent beams of light," *Concepts of Quantum Optics*, vol. 177, no. 4497, p. 27–29, 1956.

[31] R. J. Warburton, "A self-assembled quantum dot as single photon source and spin qubit: Charge noise and spin noise," *Quantum Dots for Quantum Information Technologies Nano-Optics and Nanophotonics*, p. 287–323, 2017.

[32] W. M. Witzel, M. S. Carroll, A. Morello, L. Cywinski, and S. D. Sarma, "Electron spin decoherence in isotope-enriched silicon," *Physical Review Letters*, vol. 105, no. 18, 2010.

[33] A. Fognini, A. Ahmadi, M. Zeeshan, J. T. Fokkens, S. J. Gibson, N. Sherlekar, S. J. Daley, D. Dalacu, P. J. Poole, K. D. Jöns, V. Zwiller, and M. E. Reimer, "Dephasing free photon entanglement with a quantum dot," *ACS Photonics*, vol. 6, no. 7, pp. 1656–1663, 2019.

[34] Z.-B. Chen, B. Zhao, Y.-A. Chen, J. Schmiedmayer, and J.-W. Pan, "Fault-tolerant quantum repeater with atomic ensembles and linear optics," *Physical Review A*, vol. 76, no. 2, p. 022329, 2007.

[35] C. A. Kocher and E. D. Commins, "Polarization correlation of photons emitted in an atomic cascade," *Physical Review Letters*, vol. 18, no. 15, p. 575–577, 1967.

[36] S. J. Freedman and J. F. Clauser, "Experimental test of local hidden-variable theories," *Physical Review Letters*, vol. 28, no. 14, p. 938–941, 1972.

[37] W. H. Louisell, A. Yariv, and A. E. Siegman, "Quantum fluctuations and noise in parametric processes. I.," *Physical Review*, vol. 124, no. 6, p. 1646–1654, 1961.

[38] D. C. Burnham and D. L. Weinberg, "Observation of simultaneity in parametric production of optical photon pairs," *Physical Review Letters*, vol. 25, no. 2, p. 84–87, 1970.

[39] Y. H. Shih, A. V. Sergienko, M. H. Rubin, T. E. Kiess, and C. O. Alley, "Two-photon entanglement in type-II parametric down-conversion," *Physical Review A*, vol. 50, no. 1, p. 23–28, 1994.

[40] S. Daley, "Electro-optic rotating half-waveplate for a quantum dot fine-structure eraser," *MASc Thesis, University of Waterloo*, 2019.

[41] X.-L. Wang, L.-K. Chen, W. Li, H.-L. Huang, C. Liu, C. Chen, Y.-H. Luo, Z.-E. Su, D. Wu, Z.-D. Li, H. Lu, Y. Hu, X. Jiang, C.-Z. Peng, L. Li, N.-L. Liu, Y.-A. Chen, C.-Y. Lu, and J.-W. Pan, "Experimental ten-photon entanglement," *Phys. Rev. Lett.*, vol. 117, no. 21, p. 210502, 2016.

[42] F. Wolfgramm, X. Xing, A. Cerè, A. Predojević, A. M. Steinberg, and M. W. Mitchell, "Bright filter-free source of indistinguishable photon pairs," *Optics Express*, vol. 16, no. 22, p. 18145, 2008.

[43] P. Petroff and S. Denbaars, "MBE and MOCVD growth and properties of self-assembling quantum dot arrays in III-V semiconductor structures," *Superlattices and Microstructures*, vol. 15, no. 1, pp. 15–21, 1994.

[44] E. Moreau, I. Robert, L. Manin, V. Thierry-Mieg, J. M. Gérard, and I. Abram, "Quantum cascade of photons in semiconductor quantum dots," *Physical Review Letters*, vol. 87, no. 18, p. 183601, 2001.

[45] O. Benson, C. Santori, M. Pelton, and Y. Yamamoto, "Regulated and entangled photons from a single quantum dot," *Physical Review Letters*, vol. 84, no. 11, p. 2513–2516, 2000.

[46] C. Santori, D. Fattal, M. Pelton, G. S. Solomon, and Y. Yamamoto, "Polarization-correlated photon pairs from a single quantum dot," *Physical Review B*, vol. 66, no. 4, p. 045308, 2002.

[47] M. E. Reimer, G. Bulgarini, N. Akopian, M. Hocevar, M. B. Bavinck, M. A. Verheijen, E. P. Bakkers, L. P. Kouwenhoven, and V. Zwiller, "Bright single-photon sources in bottom-up tailored nanowires," *Nature Communications*, vol. 3, no. 1, p. 737, 2012.

[48] M. Müller, S. Bounouar, K. D. Jöns, M. Glässl, and P. Michler, "On-demand generation of indistinguishable polarization-entangled photon pairs," *Nature Photonics*, vol. 8, no. 3, p. 224–228, 2014.

[49] H. Wang, Y.-M. He, T.-H. Chung, H. Hu, Y. Yu, S. Chen, X. Ding, M.-C. Chen, J. Qin, X. Yang, X. Yang, R.-Z. Liu, Z.-C. Duan, J.-P. Li, S. Gerhardt, K. Winkler, J. Jurkat, L.-J. Wang, N. Gregersen, Y.-H. Huo, Q. Dai, S. Yu, S. Höfling, C.-Y. Lu, and J.-W. Pan, "Towards optimal single-photon sources from polarized microcavities," *Nature Photonics*, vol. 13, no. 11, p. 770–775, 2019.

[50] A. Dousse, J. Suffczyński, A. Beveratos, O. Krebs, A. Lemaître, I. Sagnes, J. Bloch, P. Voisin, and P. Senellart, "Ultrabright source of entangled photon pairs," *Nature*, vol. 466, no. 7303, p. 217–220, 2010.

[51] H. Wang, H. Hu, T.-H. Chung, J. Qin, X. Yang, J.-P. Li, R.-Z. Liu, H.-S. Zhong, Y.-M. He, X. Ding, Y.-H. Deng, Q. Dai, Y.-H. Huo, S. Höfling, C.-Y. Lu, and J.-W. Pan, "On-demand semiconductor source of entangled photons which simultaneously has high fidelity, efficiency, and indistinguishability," *Physical Review Letters*, vol. 122, no. 11, p. 113602, 2019.

[52] X. Ding, Y. He, Z.-C. Duan, N. Gregersen, M.-C. Chen, S. Unsleber, S. Maier, C. Schneider, M. Kamp, S. Höfling, C.-Y. Lu, and J.-W. Pan, "On-demand single photons with high extraction efficiency and near-unity indistinguishability from a resonantly driven quantum dot in a micropillar," *Physical Review Letters*, vol. 116, no. 2, p. 020401, 2016.

[53] Y.-M. He, Y. He, Y.-J. Wei, D. Wu, M. Atature, C. Schneider, S. Hofling, M. Kamp, C.-Y. Lu, and J.-W. Pan, "On-demand semiconductor single-photon source with near-unity indistinguishability," *International Photonics and Optoelectronics Meetings*, vol. 8, no. 3, pp. 213–217, 2012.

[54] N. Somaschi, V. Giesz, L. D. Santis, J. C. Loredo, M. P. Almeida, G. Hornecker, S. L. Portalupi, T. Grange, C. Antón, J. Demory, C. Gómez, I. Sagnes, N. D. Lanzillotti-Kimura, A. Lemaítre, A. Auffeves, A. G. White, L. Lanco, and P. Senellart, "Near-optimal single-photon sources in the solid state," *Nature Photonics*, vol. 10, no. 5, p. 340–345, 2016.

[55] M. Zopf, R. Keil, Y. Chen, J. Yang, D. Chen, F. Ding, and O. G. Schmidt, "Entanglement swapping with semiconductor-generated photons violates Bell's inequality," *Physical Review Letters*, vol. 123, no. 16, p. 160502, 2019.

[56] C. Schimpf, M. Reindl, D. Huber, B. Lehner, S. F. C. D. Silva, S. Manna, M. Vyvlecka, P. Walther, and A. Rastelli, "Quantum cryptography with highly entangled photons from semiconductor quantum dots," *Science Advances*, vol. 7, no. 16, 2021.

[57] D. Huber, M. Reindl, Y. Huo, H. Huang, J. S. Wildmann, O. G. Schmidt, A. Rastelli, and R. Trotta, "Highly indistinguishable and strongly entangled photons from symmetric GaAs quantum dots," *Nature Communications*, vol. 8, no. 1, p. 15506, 2017.

[58] L. Schweickert, K. D. Jöns, K. D. Zeuner, S. F. C. D. Silva, H. Huang, T. Lettner, M. Reindl, J. Zichi, R. Trotta, A. Rastelli, and V. Zwiller, "On-demand generation of background-free single photons from a solid-state source," *Applied Physics Letters*, vol. 112, no. 9, p. 093106, 2018.

[59] M. E. Reimer, G. Bulgarini, A. Fognini, R. W. Heeres, B. J. Witek, M. A. M. Versteegh, A. Rubino, T. Braun, M. Kamp, S. Höfling, D. Dalacu, J. Lapointe, P. J. Poole, and V. Zwiller, "Overcoming power broadening of the quantum dot emission in a pure wurtzite nanowire," *Physical Review B*, vol. 93, no. 19, p. 195316, 2016.

[60] M. A. M. Versteegh, M. E. Reimer, K. D. Jöns, D. Dalacu, P. J. Poole, A. Gulinatti, A. Giudice, and V. Zwiller, "Observation of strongly entangled photon pairs from a nanowire quantum dot," *Nature Communications*, vol. 5, no. 1, p. 5298, 2014.

[61] D. Dalacu, P. J. Poole, and R. L. Williams, "Tailoring the geometry of bottom-up nanowires: Application to high efficiency single photon sources," *Nanomaterials*, vol. 11, no. 5, p. 1201, 2021.

[62] G. Bulgarini, M. E. Reimer, M. B. Bavinck, K. D. Jöns, D. Dalacu, P. J. Poole, E. P. A. M. Bakkers, and V. Zwiller, "Nanowire waveguides launching single photons in a Gaussian mode for ideal fiber coupling," *Nano Letters*, vol. 14, no. 7, p. 4102–4106, 2014.

[63] P. E. Faria Junior, T. Campos, C. M. O. Bastos, M. Gmitra, J. Fabian, and G. M. Sipahi, "Realistic multiband $k \cdot p$ approach from ab initio and spin-orbit coupling effects of InAs and InP in wurtzite phase," *Phys. Rev. B*, vol. 93, no. 23, p. 235204, 2016.

[64] M. E. Reimer, M. P. V. Kouwen, A. W. Hidma, M. H. M. V. Weert, E. P. A. M. Bakkers, L. P. Kouwenhoven, and V. Zwiller, "Electric field induced removal of the biexciton binding energy in a single quantum dot," *Nano Letters*, vol. 11, no. 2, p. 645–650, 2011.

[65] S. L. Chuang, *Physics of optoelectronic devices*. Wiley, 1995.

[66] H. Y. Ramirez, C. H. Lin, C. C. Chao, Y. Hsu, W. T. You, S. Y. Huang, Y. T. Chen, H. C. Tseng, W. H. Chang, S. D. Lin, and S. J. Cheng, "Optical fine structures of highly quantized InGaAs/GaAs self-assembled quantum dots," *Physical Review B*, vol. 81, no. 24, p. 245324, 2010.

[67] R. Seguin, A. Schliwa, S. Rodt, K. Pötschke, U. W. Pohl, and D. Bimberg, "Size-dependent fine-structure splitting in self-organized InAs/GaAs quantum dots," *Physical Review Letters*, vol. 95, no. 25, p. 257402, 2005.

[68] M. Bayer, G. Ortner, O. Stern, A. Kuther, A. A. Gorbunov, A. Forchel, P. Hawrylak, S. Fafard, K. Hinzer, T. L. Reinecke, S. N. Walck, J. P. Reithmaier, F. Klopf, and F. Schäfer, "Fine structure of neutral and charged excitons in self-assembled In(Ga)As/(Al)GaAs quantum dots," *Physical Review B*, vol. 65, no. 19, p. 195315, 2002.

[69] R. M. Stevenson, A. J. Hudson, A. J. Bennett, R. J. Young, C. A. Nicoll, D. A. Ritchie, and A. J. Shields, "Evolution of entanglement between distinguishable light states," *Physical Review Letters*, vol. 101, no. 17, p. 170501, 2008.

[70] S. A. Blokhin, M. A. Bobrov, N. A. Maleev, J. N. Donges, L. Bremer, A. A. Blokhin, A. P. Vasil'ev, A. G. Kuzmenkov, E. S. Kolodeznyi, V. A. Shchukin, N. N. Ledentsov, S. Reitzenstein, and V. M. Ustinov, "Design optimization for bright electrically-driven quantum dot single-photon sources emitting in telecom o-band," *Optics Express*, vol. 29, no. 5, p. 6582, 2021.

[71] C. Matthiesen, A. N. Vamivakas, and M. Atatüre, "Subnatural linewidth single photons from a quantum dot," *Physical Review Letters*, vol. 108, no. 9, p. 093602, 2012.

[72] K. Brunner, G. Abstreiter, G. Böhm, G. Tränkle, and G. Weimann, "Sharp-line photoluminescence and two-photon absorption of zero-dimensional biexcitons in a GaAs/AlGaAs structure," *Physical Review Letters*, vol. 73, no. 8, p. 1138–1141, 1994.

[73] A. Ahmadi, "Toward on-demand generation of entangled photon pairs with a quantum dot," *PhD Thesis, University of Waterloo*, 2020.

[74] A. J. Ramsay, A. V. Gopal, E. M. Gauger, A. Nazir, B. W. Lovett, A. M. Fox, and M. S. Skolnick, "Damping of exciton rabi rotations by acoustic phonons in optically excited InGaAs/GaAs quantum dots," *Physical Review Letters*, vol. 104, no. 1, p. 017402, 2010.

[75] M. Glässl, A. M. Barth, and V. M. Axt, "Proposed robust and high-fidelity preparation of excitons and biexcitons in semiconductor quantum dots making active use of phonons," *Physical Review Letters*, vol. 110, no. 14, p. 147401, 2013.

[76] J. H. Quilter, A. J. Brash, F. Liu, M. Glässl, A. M. Barth, V. M. Axt, A. J. Ramsay, M. S. Skolnick, and A. M. Fox, "Phonon-assisted population inversion of a single InGaAs/GaAs quantum dot by pulsed laser excitation," *Phys. Rev. Lett.*, vol. 114, p. 137401, Mar 2015.

[77] M. Reindl, K. D. Jöns, D. Huber, C. Schimpf, Y. Huo, V. Zwiller, A. Rastelli, and R. Trotta, "Phonon-assisted two-photon interference from remote quantum emitters," *Nano Letters*, vol. 17, no. 7, p. 4090–4095, 2017.

[78] S. Lüker, K. Gawarecki, D. E. Reiter, A. Grodecka-Grad, V. M. Axt, P. Machnikowski, and T. Kuhn, "Influence of acoustic phonons on the optical control of quantum dots driven by adiabatic rapid passage," *Physical Review B*, vol. 85, no. 12, p. 121302, 2012.

[79] M. D. D. Burgh, N. K. Langford, A. C. Doherty, and A. Gilchrist, "Choice of measurement sets in qubit tomography," *Physical Review A*, vol. 78, no. 5, p. 052122, 2008.

[80] T. Fokkens, A. Fognini, and V. Zwiller, "Optical quantum tomography code," 2017. Available: `https://github.com/afognini/Tomography`.

[81] S. Stufler, P. Machnikowski, P. Ester, M. Bichler, V. M. Axt, T. Kuhn, and A. Zrenner, "Two-photon rabi oscillations in a single $In_xGa_{1-x}As$/GaAs quantum dot," *Physical Review B*, vol. 73, no. 12, p. 125304, 2006.

[82] J. Schleibner, S. Bounouar, M. Strauß, S. Reitzenstein, A. Knorr, and A. Carmele, "Suppressed antibunching via spectral filtering: An analytical study in the two-photon mollow regime," *Physical review. A*, vol. 99, no. 2, p. 023813, 2019.

[83] H. Jayakumar, A. Predojević, T. Huber, T. Kauten, G. S. Solomon, and G. Weihs, "Deterministic photon pairs and coherent optical control of a single quantum dot," *Physical Review Letters*, vol. 110, no. 13, p. 135505, 2013.

[84] K. A. Fischer, L. Hanschke, M. Kremser, J. J. Finley, K. Müller, and J. Vučković, "Pulsed rabi oscillations in quantum two-level systems: beyond the area theorem," *Quantum Science and Technology*, vol. 3, no. 1, p. 014006, 2017.

[85] A. J. Ramsay, T. M. Godden, S. J. Boyle, E. M. Gauger, A. Nazir, B. W. Lovett, A. M. Fox, and M. S. Skolnick, "Phonon-induced rabi-frequency renormalization of optically driven single InGaAs/GaAs quantum dots," *Physical Review Letters*, vol. 105, no. 17, p. 177402, 2010.

[86] A. J. Hudson, R. M. Stevenson, A. J. Bennett, R. J. Young, C. A. Nicoll, P. Atkinson, K. Cooper, D. A. Ritchie, and A. J. Shields, "Coherence of an entangled exciton-photon state," *Physical Review Letters*, vol. 99, no. 26, p. 266802, 2007.

[87] J. Zhang, E. Zallo, B. Höfer, Y. Chen, R. Keil, M. Zopf, S. Böttner, F. Ding, and O. G. Schmidt, "Electric-field-induced energy tuning of on-demand entangled-photon emission from self-assembled quantum dots," *Nano Letters*, vol. 17, no. 1, p. 501–507, 2016.

[88] A. J. Bennett, M. A. Pooley, R. M. Stevenson, M. B. Ward, R. B. Patel, A. B. D. L. Giroday, N. Sköld, I. Farrer, C. A. Nicoll, D. A. Ritchie, and A. J. Shields, "Electric-field-induced coherent coupling of the exciton states in a single quantum dot," *Nature Physics*, vol. 6, no. 12, p. 947–950, 2010.

[89] B. D. Gerardot, S. Seidl, P. A. Dalgarno, R. J. Warburton, D. Granados, J. M. Garcia, K. Kowalik, O. Krebs, K. Karrai, A. Badolato, and P. M. Petroff, "Manipulating exciton fine structure in quantum dots with a lateral electric field," *Applied Physics Letters*, vol. 90, no. 4, p. 041101, 2007.

[90] K. Kowalik, O. Krebs, A. Lemaître, S. Laurent, P. Senellart, P. Voisin, and J. A. Gaj, "Influence of an in-plane electric field on exciton fine structure in InAs-GaAs self-assembled quantum dots," *Applied Physics Letters*, vol. 86, no. 4, p. 041907, 2005.

[91] R. M. Stevenson, R. J. Young, P. Atkinson, K. Cooper, D. A. Ritchie, and A. J. Shields, "A semiconductor source of triggered entangled photon pairs," *Nature*, vol. 439, no. 7073, p. 179–182, 2006.

[92] P. E. Kremer, A. C. Dada, P. Kumar, Y. Ma, S. Kumar, E. Clarke, and B. D. Gerardot, "Strain-tunable quantum dot embedded in a nanowire antenna," *Physical Review B*, vol. 90, no. 20, p. 201408, 2014.

[93] I. Yeo, D. Kim, I. K. Han, and J. D. Song, "Strain-induced control of a pillar cavity-GaAs single quantum dot photon source," *Scientific Reports*, vol. 9, no. 1, p. 18564, 2019.

[94] D. Huber, M. Reindl, S. F. Covre da Silva, C. Schimpf, J. Martín-Sánchez, H. Huang, G. Piredda, J. Edlinger, A. Rastelli, and R. Trotta, "Strain-tunable GaAs quantum dot: A nearly dephasing-free source of entangled photon pairs on demand," *Physical Review Letters*, vol. 121, no. 3, p. 033902, 2018.

[95] D. Su, X. Dou, X. Wu, Y. Liao, P. Zhou, K. Ding, H. Ni, Z. Niu, H. Zhu, D. Jiang, and B. Sun, "Tuning exciton energy and fine-structure splitting in single InAs quantum dots by applying uniaxial stress," *AIP Advances*, vol. 6, no. 4, p. 045204, 2016.

[96] J. Wang, M. Gong, G.-C. Guo, and L. He, "Eliminating the fine structure splitting of excitons in self-assembled InAs/GaAs quantum dots via combined stresses," *Applied Physics Letters*, vol. 101, no. 6, p. 063114, 2012.

[97] W. Langbein, P. Borri, U. Woggon, V. Stavarache, D. Reuter, and A. D. Wieck, "Control of fine-structure splitting and biexciton binding in $In_xGa_{1-x}As$ quantum dots by annealing," *Physical Review B*, vol. 69, no. 16, p. 161301, 2004.

[98] R. Trotta, E. Zallo, C. Ortix, P. Atkinson, J. D. Plumhof, J. V. D. Brink, A. Rastelli, and O. G. Schmidt, "Universal recovery of the energy-level degeneracy of bright excitons in InGaAs quantum dots without a structure symmetry," *Physical Review Letters*, vol. 109, no. 14, p. 147401, 2012.

[99] R. Singh, "Tuning fine structure splitting and exciton emission energy in semiconductor quantum dots," *Journal of Luminescence*, vol. 202, p. 118–131, 2018.

[100] G. Juska, V. Dimastrodonato, L. O. Mereni, A. Gocalinska, and E. Pelucchi, "Towards quantum-dot arrays of entangled photon emitters," *Nature Photonics*, vol. 7, no. 7, p. 527–531, 2013.

[101] A. Fognini, A. Ahmadi, S. J. Daley, M. E. Reimer, and V. Zwiller, "Universal fine-structure eraser for quantum dots," *Optics Express*, vol. 26, no. 19, p. 24487, 2018.

[102] R. A. Beth, "Mechanical detection and measurement of the angular momentum of light," *Physical Review*, vol. 50, no. 2, p. 115–125, 1936.

[103] G. Li, T. Zentgraf, and S. Zhang, "Rotational doppler effect in nonlinear optics," *Nature Physics*, vol. 12, no. 8, p. 736–740, 2016.

[104] B. A. Garetz and S. Arnold, "Variable frequency shifting of circularly polarized laser radiation via a rotating half-wave retardation plate," *Optics Communications*, vol. 31, no. 1, p. 1–3, 1979.

[105] C. M. Natarajan, M. G. Tanner, and R. H. Hadfield, "Superconducting nanowire single-photon detectors: physics and applications," *Superconductor Science and Technology*, vol. 25, no. 6, p. 063001, 2012.

[106] C. F. Buhrer, D. Baird, and E. M. Conwell, "Optical frequency shifting by electro-optic effect," *Applied Physics Letters*, vol. 1, no. 2, p. 46–49, 1962.

[107] J. Campbell and W. Steier, "Rotating-waveplate optical-frequency shifting in lithium niobate," *IEEE Journal of Quantum Electronics*, vol. 7, no. 9, p. 450–457, 1971.

[108] M. Kobierski, "Frequency shifting a single photon by electro-optic modulation," *MASc Thesis, University of Waterloo*, 2020.

[109] R. E. D. Paolo, E. Cantelar, R. Nevado, J. A. S. García, M. Domenech, P. L. Pernas, G. Lifante, and F. Cussó, "Photorefractive damage resistant Zn-diffused optical waveguides in LiNbO 3 : Nd 3+ and laser operation," *Ferroelectrics*, vol. 273, no. 1, p. 229–234, 2002.

[110] A. Fognini, "Pydualdds," 2018. Available: `https://github.com/afognini/PyDualDDS`.

[111] C. Qin, H. Lu, B. Ercan, S. Li, and S. J. B. Yoo, "Single-tone optical frequency shifting and nonmagnetic optical isolation by electro-optical emulation of a rotating half-wave plate in a traveling-wave lithium niobate waveguide," *IEEE Photonics Journal*, vol. 9, no. 3, p. 1–13, 2017.

[112] C. Qin, H. Lu, A. Pollick, S. Sriram, and S. J. B. Yoo, "Power-efficient electro-optical single-tone optical-frequency shifter using x-cut y-propagating lithium tanta-

late waveguide emulating a rotating half-wave-plate," *Optical Fiber Communication Conference*, 2017.

[113] R. S. Weis and T. K. Gaylord, "Lithium niobate: Summary of physical properties and crystal structure," *Applied Physics A Solids and Surfaces*, vol. 37, no. 4, p. 191–203, 1985.

[114] B. A. Korzh, Q.-Y. Zhao, S. Frasca, J. P. Allmaras, T. M. Autry, E. A. Bersin, M. Colangelo, G. M. Crouch, A. E. Dane, T. Gerrits, F. Marsili, G. Moody, E. Ramirez, J. D. Rezac, M. J. Stevens, E. E. Wollman, D. Zhu, P. D. Hale, K. L. Silverman, R. P. Mirin, S. W. Nam, M. D. Shaw, and K. K. Berggren, "Demonstration of sub-3 ps temporal resolution with a superconducting nanowire single-photon detector," *Nature Photonics*, vol. 14, no. 4, pp. 250–255, 2020.

[115] Single Quantum, "Single quantum eos snspd closed-cycle system," 2019. Available: `singlequantum.com/wp-content/uploads/2019/05/Single-Quantum-Eos.pdf`.

APPENDICES

Appendix A

Tomography Results

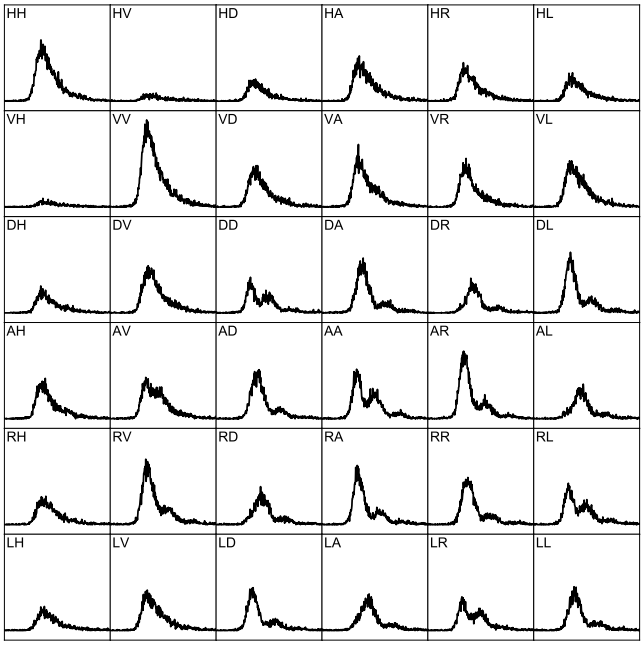

Figure A.1: Full tomography results when the quantum dot was excited quasi-resonantly.

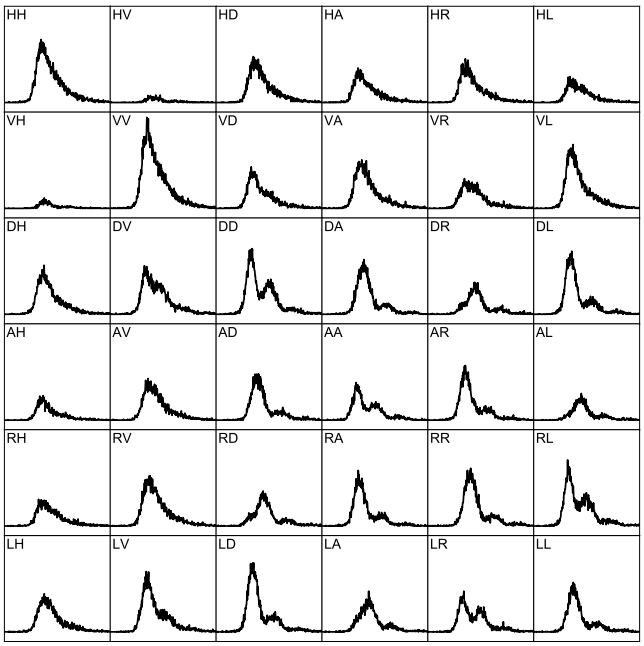

Figure A.2: Full tomography results of the quantum dot under resonant two-photon excitation